Proposal to the
National Aeronautics and Space Administration
for the

Solar High-Energy Astrophysical Plasmas Explorer

SHAPE

Volume I
Proposed Concept, Statement of Work, and Cost Plan

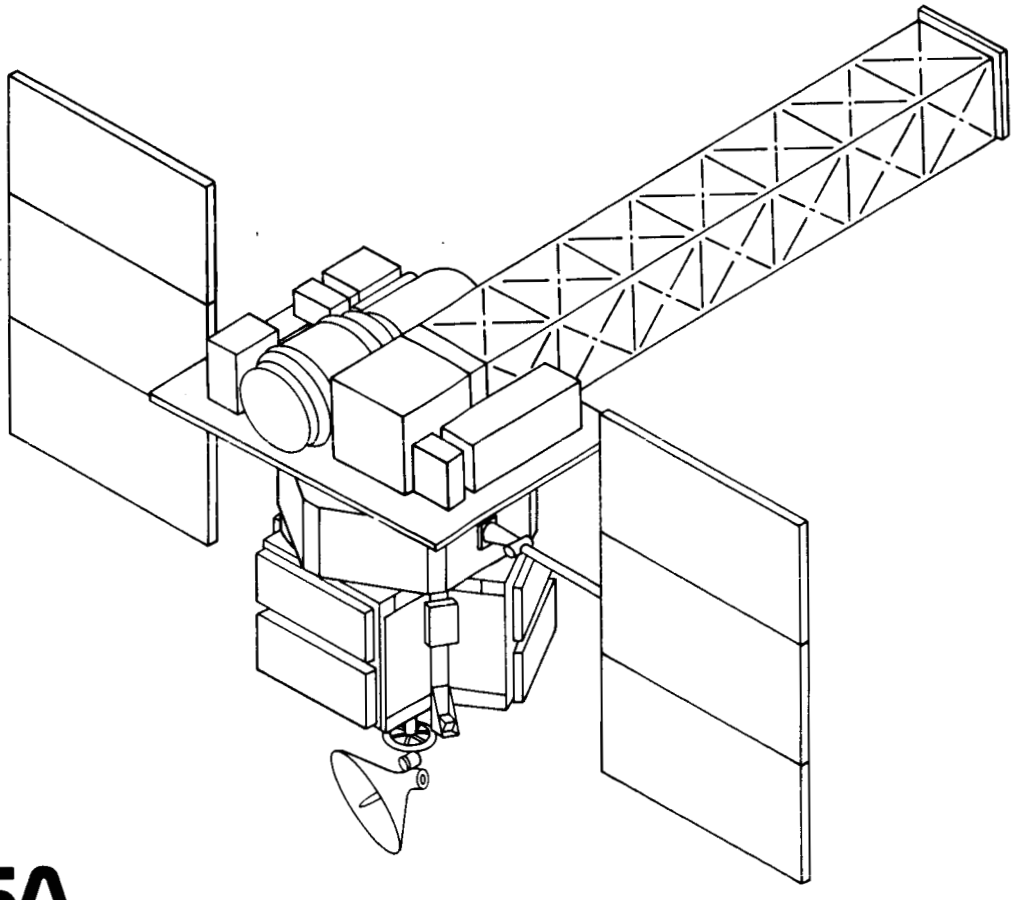

NASA

Dr. Brian R. Dennis
Principal Investigator
Laboratory for Astronomy and Solar Physics
Goddard Space Flight Center
Greenbelt, MD 20771
(301)286-7983 FTS 888-7983

Dr. Franklin D. Martin
Director
Space and Earth Sciences Directorate
Goddard Space Flight Center
Greenbelt, MD 20771

SOLAR HIGH-ENERGY ASTROPHYSICAL PLASMAS EXPLORER
(– SHAPE –)

PROPOSING ORGANIZATIONS:

University of Alabama in Huntsville
University of California at Berkeley
University of California at San Diego
California Institute of Technology
NASA Goddard Space Flight Center
Lockheed Palo Alto Research Laboratory
Naval Research Laboratory
University of New Hampshire
University of Birmingham, UK
University of Southampton, UK
University of Delft, The Netherlands
Centre d'Etude Spatiale des Rayonnements, Toulouse, France
Max Planck Inst. for Extraterrestrial Phys., FRG
Mullard Space Science Laboratory, UK
Rutherford Appleton Laboratory

PRINCIPAL INVESTIGATOR:

B. Dennis: Code 682, Laboratory for Astronomy and Solar Physics, Goddard Space Flight Center, Greenbelt, MD 20771. Telephone: (301) 286-7983.

CO-INVESTIGATORS:

T. Prince: Lead Scientist for the Gamma-Ray Imaging Device (GRID). California Institute of Technology, 220-47, Pasedena, CA 91125. Telephone: (818) 356-6605.

R. Lin: Lead Scientist for the High-Resolution Gamma-Ray and Neutron Spectrometer (HIGRANS). Space Science Laboratory, University of California, Berkeley, CA 94720. Telephone: (415) 642-1149.

M. Bruner: Lead Scientist for the Low-Energy Imaging Spectrometer (LEIS). Lockheed Palo Alto Research Laboratory, 3251 Hanover St., Palo Alto, CA 94304. Telephone: (415) 424-3273.

L. Culhane: Lead Scientist for the Soft X-Ray Impulsive Phase Spectrometer (SIPS). Mullard Space Science Laboratory, Holmbury St. Mary, Dorking, Surrey RH5 6NT, UK. Telephone: 44-30670-292.

R. Ramaty: Lead Theoretician. Code 665, Goddard Space Flight Center, Greenbelt, MD 20771. Telephone: (301) 286-8715; FTS 888-8715.

G. Doschek: Code 4170, Naval Research Laboratory, Washington, DC 20375. Telephone: (202) 767-3527.

G. Emslie: Physics Department, University of Alabama in Huntsville, Huntsville, AL 35899. Telephone: (205) 895-6167.

R. Lingenfelter: Center for Astrophysics and Space Science, University of California, La Jolla, CA 92093. Telephone: (619) 534-2464.

K. Hurley: Centre d'Etude Spatiale des Rayonnements, BP4346, 31029 Toulouse Cedex, France. Telephone: 61-55-66-37.

C. Reppin: Max Planck Institute for Extraterrestrial Physics, 8046 Garching, FRG. Telephone: 89-3299584.

F. van Beek: Laboratory for Micro-Engineering, Delft University of Technology, Landbergstraat 3, 2628 CE Delft, The Netherlands. Telephone: 31-15-785-396.

G. Simnett: Department of Space Research, University of Birmingham, P.O. Box 363, Birmingham B15 2TT, UK. Telephone: 44-21-472-1301.

DATE OF SUBMISSION: July 1986

ABSTRACT

We propose to study the concept of a Solar High-Energy Astrophysical Plasmas Explorer (**SHAPE**). The primary scientific goal is to understand the impulsive release of energy, efficient acceleration of particles to high energies, and rapid transport of energy – fundamental processes that occur in solar flares, γ-ray bursters, supernova remnants, the galactic center region, and active galaxies. Solar flare studies are the centerpiece of our investigation, because in flares these high energy processes not only occur routinely but also can be observed in unmatched detail at most wavelength regions of the electromagnetic spectrum as well as in energetic charged particles and neutrons. With the powerful new instruments of **SHAPE**, we expect to locate the regions of particle acceleration and energy release, determine the structure and conditions in those regions, characterize in great detail the accelerated particle distributions, follow the subsequent transport of energy through the plasma, and thereby identify the operative physical mechanisms.

The **SHAPE** payload consists of four instruments: **GRID** (Gamma-Ray Imaging Device), a Fourier-transform X-ray and γ-ray imager having arcsecond spatial resolution and covering the energy range from a few keV to 1 MeV; **HIGRANS** (High-resolution Gamma-Ray and Neutron Spectrometer), a cooled germanium spectrometer with a bismuth-germanate shield, covering the energy range from 10 keV to 20 MeV with keV resolution and capable of observing γ-rays and neutrons up to 1 GeV; **LEIS** (Low-Energy Imaging Spectrometer), an imaging spectrometer with arcsecond spatial resolution operating at UV and EUV wavelengths; and **SIPS** (Soft X-ray Impulsive Phase Spectrometer), a Bragg crystal spectrometer with high spectral resolution and great sensitivity at wavelengths between 1 and 9 Å.

Based on the pioneering achievements of the Solar Maximum Mission (**SMM**) in high-energy solar physics (hard X-ray imaging and γ-ray spectroscopy) and non-solar astrophysics (the discovery of γ-ray emission up to tens of MeV from bursters, the steady 0.511 MeV galactic line emission, observation of galactic radioactive aluminum, and repeating soft γ-ray bursters from the galactic bulge region), we expect that **SHAPE**, with its orders-of-magnitude improvements over **SMM** in sensitivity and spatial, spectral, and temporal resolution, will resolve many questions of fundamental interest and discover new phenomena. Specifically, **GRID** will be capable of carrying out the first arcsecond hard X-ray and γ-ray imaging of solar flares to clearly resolve flaring magnetic loops on sub-second time scales. Detailed high-resolution γ-ray spectroscopy will be possible with **HIGRANS** to resolve many nuclear lines and determine the structure of the continuum. **LEIS** will provide arcsecond UV and EUV images of the spatial structures present before, during, and after the flare, and also provide a way to detect low-energy (10 keV-1 MeV) protons. High-sensitivity, soft X-ray spectroscopy with **SIPS** will allow plasma conditions – temperature, density, flows, and turbulence – to be determined from the flare onset. In addition, elemental abundances in the solar atmosphere will be determined from complementary observations of γ-ray and soft X-ray spectral lines. Observations of other astrophysical phenomena include measurements with high energy resolution of the continuum and line features in the spectra of γ-ray bursters, hard X-ray images with arcsecond resolution of supernova remnants and jets in active galaxies, and maps of hard X-ray and γ-ray sources in congested areas of the sky such as the galactic center region.

An already existing Multimission Modular Spacecraft (**MMS**) could be used for **SHAPE**. Ideally, the payload would be placed in orbit in time for the next maximum in solar activity, expected to occur sometime between 1990 and 1992. High quality flare observations will be possible through 1995. Solar and non-solar observations would be carried out simultaneously and the non-solar observations could be continued after 1995 with possible refurbishment of the instruments.

SOLAR HIGH-ENERGY ASTROPHYSICAL PLASMAS EXPLORER

TABLE OF CONTENTS

1. INTRODUCTION

The ability to release energy impulsively and accelerate particles to high energies is a common characteristic of cosmic plasmas at many sites throughout the universe, ranging from magnetospheres to active galaxies. These high-energy processes play a central role in the overall physics of the system at each site where they are observed. The detailed understanding of these processes is one of the major goals of astrophysics, but in essentially all cases, we are only just beginning to perceive the relevant basic physics.

Nowhere can one pursue the study of this basic physics better than in the active Sun, where solar flares are the direct result of impulsive energy release and particle acceleration. Here, the acceleration of electrons is revealed by hard X-ray and γ-ray bremsstrahlung; the acceleration of protons and nuclei is revealed by nuclear γ-rays and neutrons. The accelerated particles, notably the electrons with energies of tens of keV, probably contain a major fraction of all the released flare energy, thus indicating the fundamental role of the high-energy plasma processes. Many closely correlated lower-energy phenomena, some of which are the direct consequence of interactions of the accelerated particles, also reveal the nature of the high-energy plasma processes. It is the opportunity provided by solar flares to observe in detail this multitude of interwoven characteristics of high-energy plasmas that makes this study so exciting and fruitful.

That this endeavor can indeed be profitably pursued in solar flares has been demonstrated by the pioneering observations carried out with instruments flown during the active phase of the last solar cycle (1978–1984) on the NASA **Solar Maximum Mission (SMM)** and the International Sun-Earth Explorer 3 **(ISEE-3)**, the Japanese **Hinotori** satellite, and the DoD **P78-1** spacecraft. Of the many results obtained, the imaging of solar flares in hard X-rays (e.g., Hoyng *et al.* 1981, Ohki *et al.* 1983, Tsuneta *et al.* 1984) and the detection of γ-ray lines from many flares (Chupp 1984) are particularly significant. Improved sensitivity and finer spatial, spectral, and temporal resolution are clearly needed, however, to fully exploit these new and powerful diagnostic tools. Hard X-ray images with fine spatial and temporal resolution can be used to determine the location of the electrons and trace the transport of the energy released impulsively in the flare; γ-ray line measurements made with sufficient energy resolution to determine intensities and spectral shapes of individual emission lines can provide the complete distribution of the accelerated particles in momentum space, that is, both their energy spectra and their angular distributions. These opportunities, and the promise of new discoveries anticipated from future observations, are the main drivers of the proposed **SHAPE** (Solar High-Energy Astrophysical Plasmas Explorer) concept.

The major areas that will be addressed by observations with **SHAPE** are energy release, particle acceleration, and energy transport in cosmic plasmas. We would like to know what processes liberate the energy stored in unstable magnetic configurations, how this energy is converted into kinetic energy of fast particles and thermal energy of hot plasma, what mechanisms transport particles and energy away from the energy release site, and what observational consequences result from the operative radiation mechanisms. The physics of these processes is highly involved, drawing on plasma physics, magnetohydrodynamics, kinetic theory, particle and radiation transport, and atomic and nuclear physics. Improved hard X-ray and γ-ray observations are essential for unravelling these difficult but fundamentally important astrophysical problems. In the case of solar flares, such high-energy observations must be combined with ultraviolet (UV), extreme ultraviolet (EUV), soft X-ray, and direct neutron observations for maximum scientific reward.

An additional objective of **SHAPE** is the study of elemental abundances. The complementary

nature of γ-ray and soft X-ray spectroscopy will permit simultaneous abundance determinations at different heights, allowing studies of elemental fractionation in the solar atmosphere.

This proposal describes the scientific objectives and instrumentation of **SHAPE**, an Explorer optimized for the study of solar high-energy phenomena in the next phase of solar activity (expected to extend at least to 1995). The two high-energy instruments are **GRID** (Gamma-Ray Imaging Device) and **HIGRANS** (High-Resolution Gamma-Ray and Neutron Spectrometer).

GRID will have arcsecond spatial resolution and sub-second temporal resolution and will be capable of producing images at photon energies between a few keV and 1 MeV. These images, the first at photon energies above 40 keV, will be comparable in morphological detail to the solar flare images obtained at microwave frequencies with the Very Large Array. With angular resolution matching the expected sizes of flare structures and temporal resolution matching the characteristic timescales of the acceleration and transport mechanisms, we will be able to locate the regions of acceleration and follow the subsequent redistribution of the released energy.

HIGRANS will observe from keV to GeV energies, with keV resolution up to 10 MeV. This resolution is sufficient to separate the many nuclear lines observed with **SMM** and to measure their shapes. High-energy resolution is also essential for observing structure in the continuum, such as that expected if more than one source or mechanism contributes to the observed radiation. At energies above 10 MeV, **HIGRANS** will be capable of observing neutrons and separating pion-decay γ-rays from relativistic electron bremsstrahlung. This will allow the investigation of the highest-energy processes occurring in flares.

The two low-energy instruments, **LEIS** (Low-Energy Imaging Spectrometer) and **SIPS** (Soft X-Ray Impulsive Phase Spectrometer), are essential for defining the structures in which the the explosive high-energy phenomena take place, and for revealing other direct manifestations of the impulsive energy release. **LEIS** will provide monochromatic images with arcsecond spatial resolution at UV wavelengths from 1200 to 1452 Å and at EUV wavelengths from 240 to 285 Å. These wavelength ranges cover emission lines from plasma at temperatures between about 10^4 and 2×10^7 K. **LEIS** will also be able to detect 10-keV-to-1-MeV protons in flares for the first time, by searching for red-shifted Lyman-α emission from de-excitation of fast hydrogen atoms formed by the protons via charge exchange. **SIPS** will provide high-resolution spectra at wavelengths between 1 and 9 Å with both high sensitivity and high time resolution. Simultaneous interplanetary energetic-particle observations and vigorous ground-based and theoretical support programs are also required to achieve the scientific objectives.

Both **GRID** and **HIGRANS** have unique capabilities for observing other astrophysical sources. Of particular interest are objects in which violent energy release processes and particle acceleration can be detected in hard X-rays and γ-rays. These sources include γ-ray bursters, supernova remnants, the galactic center, and active galaxies. The bulk of the observed luminosity from many of these sites is in high-energy photons, indicating again the dominant role of energetic particles.

No planned future mission, including the Gamma-Ray Observatory (**GRO**) and the Japanese **SOLAR-A** satellite (formerly the High Energy Solar Physics mission, **HESP**), has instrumentation which can match the high sensitivity and fine spatial and energy resolutions of the **SHAPE** instruments. The **SHAPE** observations will complement (and be complemented by) data obtained from these two other satellites and from the **International Solar-Terrestrial Physics (ISTP)** Program.

2. THE SOLAR OBJECTIVES OF SHAPE

A large solar flare releases as much as 10^{32} ergs in times as short as 100 to 1000 s. Much of that energy appears in the form of high-energy particles and hot plasma. It is believed that the energy comes from the dissipation of the non-potential components of strong magnetic fields in the solar atmosphere, possibly through magnetic reconnection. The high-energy flare phenomena produce a wide variety of observable emissions as shown schematically on the fold-out sheet. A thorough understanding of the physical processes which lead to these observational signatures is essential to understanding solar flares. Of the many available signatures, hard X-rays, γ-rays, and neutrons, along with radio and microwave emissions, form a distinct class in that they are produced before the accelerated particles are thermalized in the ambient atmosphere. Consequently, they provide the most direct information available on the energy release and particle acceleration processes. Observations of UV, EUV, and soft X-ray emissions provide complementary information on the conditions (e.g., temperature, density, and magnetic configuration) of the plasma at and near the energy release site before, during, and after the flare.

2.1 FLARE GEOMETRY AND ENERGY TRANSPORT

(a) Sub-relativistic Electrons.

Magnetic loops in the solar atmosphere almost certainly play a role in the flare process. A popular flare model, consistent with a wide variety of observational data, is the thick-target model (Brown 1971). It involves the impulsive acceleration of electrons and protons, probably in the coronal part of a loop or arcade of loops. These particles propagate along the magnetic field lines and interact through collisional, collective, and other non-collisional processes with the ambient gas in the legs of the loops to produce a variety of observable signatures. Historically, the most outstanding of these signatures is the impulsive hard X-ray emission, believed to be bremsstrahlung produced in collisions between high-energy electrons and ambient protons. The **SHAPE** concept places considerable emphasis on the interpretation of hard X-ray bursts but other signatures of the high-energy flare phenomena will also be investigated at different wavelengths.

Hard X-Ray Bremsstrahlung. In the thick-target model, the electron beams which produce the hard X-ray bremsstrahlung must contain a large fraction of the total flare energy due to the inefficiency of the bremsstrahlung process relative to collisional energy losses (Lin and Hudson 1976, Hoyng *et al.* 1976). An assessment of the validity of this model is, therefore, fundamental to our understanding of flares, particularly since alternative models for hard X-ray production have been proposed, some of which require less energy in sub-relativistic electrons. For example, in the thermal model proposed by Brown *et al.* (1979) and subsequently developed in some detail by Smith and Harmony (1982 and references therein), the bremsstrahlung is produced in a quasi-thermal plasma with a temperature in excess of 10^8 K located in the coronal part of the loop at or close to the initial energy release site. Since in this model there are no energy losses from bremsstrahlung-producing electrons interacting with cooler electrons, its energetic efficiency can be much larger than that of the thick-target model. Although a hybrid model involving both particle acceleration and direct heating may be the most appropriate, it is important to define the signatures of each canonical model at as many wavelengths as possible and to test these signatures through coordinated observations. This was the aim of **SMM** and qualitative advances in our understanding of flares were made. More quantitative observational tests of models will be well within the capabilities of the proposed **SHAPE** payload and examples of such tests are discussed below.

Arcsecond imaging of the hard X-ray emission with the high sensitivity and broad energy coverage of **GRID** will provide a definitive, if not the definitive, test of hard X-ray production models. Theoretical predictions of the hard X-ray spatial structure that could be tested with **GRID** have been made by a number of authors (Emslie 1981, Leach and Petrosian 1983, Holman 1986). The imaging observations carried out with **SMM** and **Hinotori** have provided data for some flares which are consistent with the double structure expected from the impact of nonthermal electrons at the footpoints (Hoyng *et al.* 1981, Ohki *et al.* 1983). However, these images were obtained with relatively low angular resolution (~8 arcseconds, corresponding to 5800 km at the Sun) and were limited to photon energies of less than 40 keV, where the X-ray flux usually includes a significant contribution from a superhot thermal plasma with a temperature that can be as high as or higher than 3.5×10^7 K (Lin *et al.* 1981). No imaging observations have been made at higher energies but stereoscopic views of behind-the-limb events with widely separated spacecraft show that, at least in some cases, the dominant component of high-energy (>100 keV) X-ray emission comes from low altitudes, presumably from footpoints (Kane *et al.* 1982).

The capabilities required of a hard X-ray imager such as **GRID** are set by the spatial and temporal scales of the magnetic structures involved in a flare and by the processes that modify the electron spectrum. A typical flaring magnetic loop is about 10 arcseconds in diameter with a cross-sectional diameter of about 1 arcsecond. Hard X-ray sources as large as 2 arcminutes have been observed (Hudson *et al.* 1985) and compact flares much less than 10 arcseconds in total extent are known to exist. Fluctuations in hard X-ray intensity have been observed on time scales shorter than 100 ms (Kiplinger *et al.* 1983).

A fundamental length scale for the hard X-ray observations can be obtained from considerations of the collisional energy-loss processes of the bremsstrahlung-producing electrons. A 40 keV electron will produce the bulk of its hard X-ray emission over a distance of about 2000 km in a medium of density 3×10^{11} cm^{-3}, such as is typical of a dense flare plasma (Dere *et al.* 1979). This corresponds to ~3 arcseconds on the solar disk. Thus, appreciable modification to the energy spectrum of the hard X-ray producing electrons will take place in distances of ~1 arcsecond. One of the objectives of **GRID** is to detect changes in the electron spectrum on these distance and time scales. This will provide a stringent test of the thick-target model and indicate if other processes such as beam-plasma instabilities are degrading the electron energy in addition to Coulomb collisions.

Other Observational Signatures of Sub-relativistic Electrons. One possible signature of sub-relativistic electrons is the broadening and wavelength shifts of soft X-ray, EUV, and UV lines, presumably due to the hydrodynamic response of the solar atmosphere to the collisional energy deposited by nonthermal electrons (e.g., Nagai and Emslie 1984). During the impulsive phase of flares, soft X-ray spectra show line broadening and blue-shifted components that reveal the existence of mass motions in heated chromospheric plasma, but the interpretation of the observations is still controversial (Doschek *et al.* 1986). By observing the soft X-ray line profiles with the higher sensitivity of **SIPS** and by correlating these data with EUV and UV images obtained with **LEIS**, we will be able to test quantitatively the predictions of flare heating models (e.g., Cheng *et al.* 1984). Coupled with the hard X-ray data from **GRID** and **HIGRANS**, this will in turn afford us a means of identifying the physical processes affecting the transport of energy in the flaring atmosphere, for example, return-current ohmic heating, and collective plasma effects.

Other important signatures of nonthermal electron impact are bursts of emission in certain UV and EUV lines formed at temperatures of a few times 10^5 K, typical of the transition region (Orwig and Woodgate 1986). Enhancements are also seen in the UV continuum. These bursts are

observed simultaneously with hard X-ray bursts and they provide valuable clues to the existence of sub-relativistic electrons and to the mode of energy transport in the flare atmosphere. Their full exploitation must, however, await the higher sensitivity UV, EUV, and soft X-ray data from **LEIS** and **SIPS**. In addition, nonthermal electrons produce bursts in the X-ray Fe Kα radiation (Tanaka *et al.* 1984, Emslie *et al.* 1986), which have, so far, been observed in only a few flares with low statistical significance. A Kα burst in coincidence with a hard X-ray burst would be a powerful diagnostic of the acceleration of electrons to sub-relativistic energies. The improved sensitivity of **SIPS** will allow this diagnostic tool to be used to establish the existence of non-thermal electrons interacting in the lower corona, thus providing a test of the thick-target model that is complementary to that provided by **GRID**.

Characteristics of the Energy Release and Particle Acceleration Region. The plasma conditions and the magnetic structure of the energy release and particle acceleration regions can be obtained from the **LEIS** and **SIPS** observations. The broad temperature coverage provided by **LEIS** ensures that plasma at any temperature between chromospheric and flare values (10^4 to 2×10^7 K) can be imaged. Thus, images will be obtained with arcsecond resolution of the plasma that traces out the magnetic configuration before, during, and after the flare. Information on the plasma conditions (temperature, density flows, turbulence, etc.) will be obtained from the **SIPS** observations of soft X-ray line profiles. The spectral resolution is high enough to detect flows with velocities of >60 km s^{-1}. Motions of such magnitude are indeed indicated in the few **SMM** observations of the very early phases of flares. In addition, the slow preflare heating that is seen as a gradual rise in the broadband X-ray flux can be studied in detail with **SIPS** and **LEIS**. These results, when combined with simultaneous ground-based microwave observations, will allow accurate estimates to be made of the magnetic field strength and configuration within the flaring region (Holman and Kundu 1985, Hurford 1986).

(b) Protons and Relativistic Electrons

γ-Ray and neutron emissions are the most direct signatures of proton and relativistic electron interactions in the solar atmosphere (e.g., Ramaty and Lingenfelter 1982). The recent observations also can be interpreted in the context of a thick-target model (e.g., Murphy and Ramaty 1985), but in this case the information comes from timing arguments and total charged particle yields. In fact, unique new information on the flare geometry and on the interaction model will be obtained with the high temporal and energy resolutions of **HIGRANS**. At energies near 0.5 MeV, where proton and α-particle interactions produce significant emission, imaging observations with **GRID** will provide valuable spatial information.

Density and Temperature Determinations. Observations with **HIGRANS** of the time dependence and spectrum of positron annihilation radiation provide information on the density and temperature at the site where these particles annihilate. This site is probably also the interaction site of the accelerated protons. The time profile of the 0.511 MeV line observed with poor time resolution on **SMM** (Share *et al.* 1983) suggests that the positrons slow down and annihilate in less than several seconds, implying an ambient density of $>10^{12}$ cm^{-3}. Measurements made with **HIGRANS** of the 0.511-MeV line width will allow the temperature of the annihilation site to be determined. The energy resolution of this instrument (~1 keV at 0.511 MeV) is sufficient to measure temperatures down to 10^4 K. Furthermore, the 0.511 MeV line should be accompanied by a characteristic continuum resulting from positronium annihilation if the density of the ambient medium is less than about 10^{15} cm^{-3} (Crannell *et al.* 1976). This continuum will also be detectable with **HIGRANS**.

Beaming. The observation reported by Rieger *et al.* (1983) that γ-ray flares at energies >10 MeV occur preferentially at sites near the solar limb is strong evidence for an anisotropic distribution of relativistic electrons. Dermer and Ramaty (1986) have shown that both downward-beamed distributions of relativistic electrons and distributions peaking at directions parallel to the photosphere are consistent with these observations.

Information on the angular distribution of the protons can be obtained by comparing the number of neutrons moving downward toward the photosphere with the number moving upward (Murphy and Ramaty 1985). The former is derived from observations of the 2.223 MeV line resulting from neutron capture in the photosphere, while the latter can be found from observations of the neutron flux at the Earth. For the 1982 June 3 flare observed with the **Gamma-Ray Spectrometer (GRS)** on **SMM**, the protons cannot have a strongly downward-beamed distribution (Murphy and Ramaty 1985). Thus, at least for that flare, the protons produced nuclear reactions while they were either mirroring in the converging magnetic field or being scattered by MHD turbulence at the footpoints. By observing many flares at various locations on the Sun with **HIGRANS**, it will be possible to map out the entire angular distribution of the neutrons, and hence also of the protons which produce them.

Further information on the proton angular distribution will come from the **HIGRANS** measurements of the shapes of the nuclear deexcitation lines (Kozlovsky and Ramaty 1977). Since these lines are produced by excited nuclei whose recoil motion reflects the motion of the bombarding protons, anisotropic proton distributions lead to Doppler shifted lines whose shapes depend on the anisotropy, on the direction of the magnetic field, and on the location of the flare site. Particularly promising are the lines of ^{7}Li and ^{7}Be at 431 and 478 keV, respectively, produced in interactions of α-particles with helium atoms (see Appendix 2). We estimate that for a flare comparable to the 27 April 1981 flare, from which these lines were seen with the relatively low resolution **GRS** on **SMM**, **HIGRANS** will detect about 3000 photons from ^{7}Li and ^{7}Be de-excitations. Such a large number of counts will allow for a detailed mapping of the shapes of these lines and hence of the α-particle angular distribution (presumed to be similar to the proton distribution).

Trapping and Escape. The combination of γ-ray and neutron observations with interplanetary particle observations provides information on the trapping of the particles at the Sun. The number of protons required to produce the γ-rays and neutrons in flares is generally much higher than the number of protons which escape from these flares into interplanetary space (von Rosenvinge *et al.* 1981). On the other hand, there are many flares which release energetic particles to interplanetary space but whose γ-ray emission has so far not been seen. A possible interpretation of this result is that the protons which produce the γ-rays and neutrons are accelerated in closed magnetic loops, whereas the interplanetary protons are accelerated on open field lines. This model could be tested by detecting the γ-rays produced by the particles which are accelerated on open field lines in the corona but which precipitate back into the denser chromosphere. **HIGRANS**, with a sensitivity of $\sim 10^{-4}$ photons cm^{-2} s^{-1} in the 2.223 MeV line in a 1000-s observation, will be able to detect γ-rays from about 5×10^{29} particles with energies greater than 30 MeV interacting at the Sun. This amounts to about 0.5% of the particles released from the Sun for a moderate interplanetary event.

2.2 ENERGY RELEASE AND PARTICLE ACCELERATION

As we have emphasized above, observations of hard X-rays strongly suggest that sub-relativistic electrons contain a substantial, if not dominant fraction of all the released flare energy. This result,

coupled with the fact that hard X-ray emission is a very common property of flares, implies a strong link between the energization of these electrons and the impulsive energy release processes. Consequently, a primary objective of **SHAPE** is to pinpoint the electron acceleration sites and to trace the energy transport paths. Another objective is to determine whether these electrons are part of a thermal distribution, in which case the energization is due to bulk heating, or whether they form a genuine nonthermal population which requires acceleration mechanisms such as expected in reconnecting magnetic fields, at shocks, and in MHD turbulence. The **GRID** instrument, with arcsecond resolution and the ability to produce hard X-ray images at energies well above those where background thermal contamination is a problem, will provide crucial observations for achieving these objectives. Not only will the site(s) of the original energization be evident, but the manner in which the source of hard X-ray emission spreads throughout the flaring region during the event will provide valuable clues to the nature of the energization, such as its division into thermal and nonthermal components. When combined with information from the **LEIS** observations, many of the physical parameters of the acceleration region can be determined, including the level of turbulence and the electric field strength (Holman 1985).

Prior to the **SMM** observations it was believed that proton acceleration is a secondary phenomenon that follows the acceleration of the hard X-ray emitting electrons. This second-phase concept probably is valid for the acceleration of the bulk of the protons observed in interplanetary space (Cane *et al.* 1986). But the **SMM** observations that show γ-rays emitted simultaneously with the hard X-rays to within the 1-s timing accuracy of the data, imply that a broad spectrum of particles ranging from sub-relativistic electrons to GeV ions is often accelerated impulsively (Forrest 1983). However, it is not known whether this acceleration can be achieved by a single mechanism or whether injection (Forman *et al.* 1986) and second-step acceleration (Bai 1986) are needed.

A very important question is whether protons are accelerated in all flares or only in the more energetic ones. A definitive indicator of the presence of high energy protons is the 2.223 Mev line, which is the strongest γ-ray line (except for flares near the limb) and intrinsically very narrow. Because of its high energy resolution and low background, **HIGRANS** is a factor of at least 20 more sensitive in this line than **GRS**. Consequently, if protons are accelerated in all flares, and the γ-ray emission scales as the microwave emission, **HIGRANS** will observe $\sim$10 flares per month in the 2.223 MeV line near solar maximum.

An in-depth study of the proton spectrum above 10 MeV will be carried out from measurements made with **HIGRANS**. Information on the proton spectrum from 10 to 100 MeV will be provided by γ-ray line observations, information above several hundred MeV will be provided by observations of pion-decay γ-rays, and complementary information from $\sim$10 MeV to several GeV will be provided by neutron observations. Observations of very high energy neutrons will also be made with ground-based neutron monitors. γ-Rays from pion decay have already been observed from one flare (Forrest *et al.* 1985), and high-energy neutrons have been seen from several flares (Chupp *et al.* 1982, Debrunner *et al.* 1983).

Currently, we have no direct information on the proton spectrum at energies much below 10 MeV. It may well be that a significant fraction of the flare energy is hidden in such relatively low energy protons. By measuring the detailed profile of the Lyman-α line during the impulsive phase of flares with **LEIS**, we will be able to make the first measurements sensitive to protons at energies of 10 keV-1 MeV. De-excitation of hydrogen atoms formed by charge exchange between neutral hydrogen atoms and downward-moving protons produces excess emission in the red wing of this line. The detection of this excess emission would allow an estimate to be made of the fraction of

the flare energy residing in protons below ~1MeV during the impulsive phase (Orrall and Zirker 1976, Canfield and Chang 1985).

2.3 SOLAR ABUNDANCES

Complementary information on the composition of the solar atmosphere can be obtained from γ-ray and soft X-ray spectroscopy (Murphy *et al.* 1985, Doschek *et al.* 1985). Nuclear reactions of accelerated protons and α-particles with heavier nuclei in the ambient gas produce narrow nuclear de-excitation γ-ray lines whose relative intensities depend on the composition of the gas in the proton interaction site, probably in the chromosphere. In the soft X-ray region, most lines are due to hydrogen-like and helium-like ions characteristic of coronal and higher temperatures, so that these lines provide information on abundances in the flare plasma confined in coronal flux tubes. The combination of simultaneous abundance determinations in the chromosphere from γ-rays and in the corona from X-rays will allow a detailed study of the fractionation effects in the solar atmosphere.

The abundances deduced from γ-ray spectroscopy of one flare have been compared by Murphy *et al.* (1985) with local galactic abundances (Meyer 1985), which are believed to represent photospheric abundances. The principal difference was found to be an underabundance of C and O in the γ-ray set. A similar suppression of C and O in the coronal abundances relative to local galactic abundances has been pointed out by Meyer (1985), who noted that the suppression may be correlated with the first ionization potential of the elements. Such a correlation could be caused by charge-dependent mass transport from the photosphere to the corona. The differences between the coronal and photospheric K/Ar and Ca/Ar ratios inferred from X-ray observations (Doschek *et al.* 1985) are consistent with this correlation.

In a flare similar to the 1981 April 27 flare observed with **GRS**, **HIGRANS** will detect several hundred to a few thousand photons in each of the dozen or so major γ-ray lines with typical line-to-continuum ratios (L/C) of between 1 and 10 (see Table B1, Appendix B). These include lines of the elements C, N, O, Ne, Mg, Si, Li, Be, and four lines of Fe. These major lines will be detected with a statistical significance of 10 to 50σ allowing line shapes and asymmetries to be accurately determined. Even for flares with line fluences >30 times smaller, most of these lines will be detected at, or above, the 3σ level if L/C remains the same. **GRS** did not have fine enough energy resolution to resolve any of these lines.

X-ray abundances of all elements from Mg through Ni will be measured with **SIPS**, including such low-abundance elements as K, Ti, Mn, and Cr. **SMM** observations indicate that the calcium abundance varies during a flare and from flare to flare (Sylwester *et al.* 1984). **SIPS** will be used to confirm this result and to study abundance variations for other elements.

γ-Ray observations made with **HIGRANS** can also provide information on the photospheric abundance of ^{3}He from the time profile of the 2.223 MeV line (Wang and Ramaty 1974, Prince *et al.* 1983). The ^{3}He abundance is of importance to cosmology as well as to our understanding of the burning and mixing processes in the solar interior.

2.4 NONFLARING STUDIES

In addition to the study of solar flares, the higher sensitivity of the proposed complement of instruments will allow us to investigate the flare process on smaller scales than previously possible; this study of "microflares" will provide information on the flare-associated processes of energy release, particle acceleration, and energy transport in its most basic form (Lin et al. 1984). Di-

agnostics of regions of reduced activity could be routinely obtained with **SIPS** and **LEIS**. The thermal emission from magnetic structures both within and outside active regions will provide important information on nonflaring solar activity and coronal heating.

Studies of small-scale emerging magnetic flux, particularly in the form of X-ray bright points and ephemeral active regions, can also be made with **SIPS** and **LEIS**. Large active regions represent only a small fraction of the total magnetic flux which emerges at the solar surface; the overall balance between large and small emerging regions is such that the total rate of magnetic flux emergence is nearly constant throughout the cycle. At present, we do not know the smallest scale size of flux emergence regions. The size spectrum must turn over at some point, and the improvement in spatial resolution obtainable with **LEIS** could be used to determine this value. A number of relatively low temperature (a few million degrees) strong coronal lines that fall in the XUV region such as Fe XV at 284Å would be ideal for investigating bright points. Temperatures and dynamics information could also be obtained from the **SIPS** observations. In addition to investigating bright points, bright active region loops provide an ideal testing ground for solar loop modelling, a subject that has received considerable attention in the last several years in both the solar and stellar community. **LEIS** could provide the temperature and density distribution along the length of a loop, i.e., the parameters crucial for comparison with models.

3. THE NONSOLAR OBJECTIVES OF SHAPE

GRID and **HIGRANS** will have important roles in nonsolar astrophysics. **GRID**, with 1 arcsecond imaging over a 1 square degree field of view, will be the most powerful hard X-ray imaging instrument yet flown. With the solar offset pointing capabilities of the MMS, it will be possible to point **GRID** at all X-ray sources within 20° (and perhaps further) of the ecliptic plane. **HIGRANS**, with keV energy resolution and a 3-steradian field of view, will likewise be the most powerful high-energy-resolution instrument flown with unique capabilities for the study of γ-ray bursters over a broad energy range. Together, these instruments will bring to high energy astrophysics an exceptionally potent combination of angular, spectral, and temporal resolution.

γ-Ray Bursters. γ-Ray bursters are observed as intense flashes of X-ray and γ-ray emission lasting from a few milliseconds to over 100 s. They are thought to occur on or near the surface of magnetic neutron stars as a result of either impulsive accretion of matter onto the star, thermonuclear runaway of more slowly accreted matter, or quakes in the interior caused by sudden phase transitions (e.g., Ramaty and Lingenfelter 1982).

HIGRANS will detect many γ-ray bursts in its wide field of view but it will be difficult to use **GRID** with its narrow field of view since most standard γ-ray bursts occur at random times from unpredictable directions. Only two repeating bursters are known: the event on March 5, 1979 (GRB790305) has been followed by later but infrequent events from the same region of the sky; likewise GRB790324. The recent discovery of a third, more prolific, repeating source in the galactic bulge presents the exciting possibility that **GRID** could be pointed at such a source when it is producing up to 18 bursts per day, as it was between November 1983 and January 1984. The detection of just one burst with **GRID** would allow the source to be located to within $\sim$1.5 arcseconds, sufficiently precise to allow a detailed search to be made for a counterpart at other frequencies. **HIGRANS** will also be able to detect such bursts during much of the year and provide high-resolution measures of the spectra, reported to be unusually soft for a γ-ray burst.

Although the origin of individual bursts has not yet been identified, spectral features provide

strong evidence that neutron stars are the source. Absorption features at energies between 30 and 70 keV are attributed to cyclotron absorption in intense (3 to 5×10^{12} gauss) magnetic fields associated with neutron stars (Mazets *et al.* 1981, Dennis *et al.* 1982, Hueter 1984); emission features around 400 keV are attributed to gravitationally redshifted 511 keV positron annihilation radiation corresponding to surface redshifts of $z \simeq 0.2$ (Mazets *et al.* 1981, Teegarden and Cline 1980). These features are only poorly understood at the present, since, with one exception, they have all been observed only with low-resolution NaI(T*l*) detectors. High-resolution spectroscopy possible with **HIGRANS** will allow the widths and shapes of the lines to be measured with the goal of identifying the different mechanisms and emission sites which contribute to the observed flux.

It will also be possible with **HIGRANS** to study the continuum spectrum of γ-ray bursts. **SMM** observations revealed that the continuum emission extends up to at least 20 MeV and that a large part of the burst energy is emitted at high energies (Matz *et al.* 1985). **HIGRANS** observations will bring increased sensitivity and fast timing to the determination of these spectra and their temporal evolution, which itself can provide additional clues to the origin of the bursts (Norris *et al.* 1986).

Supernova Remnants. It is now known that the central pulsar is the energy source of the Crab Nebula, but the process by which energy is transported from the pulsar to the nebula is not well understood. The angular structure determined as a function of energy from **GRID** images can be used to discriminate between diffusion and bulk transport models for the energy flow, with diffusion predicting a specific shrinkage of the nebular size with increasing energy. Similar results may be obtained for other supernova remnants such as Cas A and Tycho.

The Galactic Center Region. The Galactic Center region contains the source of the observed 0.511 MeV positron annihilation line (Johnson *et al.* 1972, Leventhal *et al.* 1978, Riegler *et al.* 1981) as well as several X-ray sources (Watson *et al.* 1981). Imaging with **GRID** will provide a precise position for the annihilation line source. **HIGRANS** will be used to detect the annihilation line by using observations during Earth occultations for background estimations. In a similar manner, **HIGRANS** will also be used to observe emission in the 1.809 MeV line from the decay of ^{26}Al. This line is believed to be localized in a region with an angular size of $<10^{\circ}$ around the Galactic Center (Ballmoos *et al.* 1986). In regions such as the galactic bulge which are crowded with many sources, it will be possible with **GRID** to clearly separate individual sources and monitor variability over a wide range of timescales. **GRID** will be used in parallel with **HIGRANS** to study transients such as X-ray bursters.

Active Galaxies and Clusters. Imaging of the brighter jets of active galaxies (e.g., Cen A) could be carried out with **GRID**. The jets are evidence for the transfer of energy from the nucleus of the active galaxy to the outer radio lobes. Imaging at high energies is crucial for developing physical models of these sources.

Many clusters of galaxies are known to contain gas with characteristic temperatures of about 8 keV, resulting in hard X-ray emission. From the soft X-ray maps obtained with the **Einstein Observatory**, it appears that there are localized regions of enhanced surface brightness. The hard X-ray measurements indicate the presence of excess flux above a thermal spectrum at high photon energies (Lea *et al.* 1981). These hotter regions are not well localized with respect to emission at lower energies. **GRID** would have access to many suitable clusters and could pinpoint regions of hard X-ray emission.

4. THE SHAPE PAYLOAD

It is clear from the discussion of scientific objectives presented in Sections 2 and 3 of this proposal that new high-resolution imaging and spectroscopy observations are needed at hard X-ray and γ-ray energies. Improved low-energy imaging and spectroscopy are also required to define the structure and plasma conditions in which the high-energy phenomena occur. **SHAPE** has been developed to satisfy this need for improved observations. The **MAX '91** science committee, convened by NASA to study ways to obtain these observations, developed the idea of reusing an existing Multimission Modular Spacecraft (MMS). This concept, first proposed after the highly successful SMM repair mission, has now been incorporated as a fundamental aspect of the Explorer program, with the attendant cost savings and programmatic advantages. A copy of the **MAX '91** report is included for reference with this proposal.

The proposed instruments are shown in the fold-out sheet as they would appear mounted on an MMS. A summary of their basic characteristics is given in Table 4.0 and a brief description of each instrument is given in the following four sections with more details in the appendixes. The instruments have been designed from the beginning to be compatible with the SMM/MMS. The pointing direction of the instruments is set perpendicular to the symmetry axis of the MMS, so that the gravity-gradient torques that result from the 7-m-long **GRID** boom can be handled by the MMS reaction wheels.

Table 4.0 SHAPE Payload

Instrument	Range	Angular Resolution	Technique
Gamma-Ray Imaging Device (**GRID**)	5 keV to 1 MeV	1·5 arcsec	Fourier-transform collimators, position-sensitive proportional counters and NaI(Tl) detectors
High-Resolution Gamma-Ray and Neutron Spectrometer (**HIGRANS**)	10 keV to >100 MeV	Full Sun	Cooled HPGe detectors BGO-scintillators
Low-Energy Imaging Spectrometer (**LEIS**)	240–285 Å 1200–1425 Å	~1 arcsec	Normal-incidence UV and EUV telescope, toroidal gratings, imaging detector
Soft X-ray Impulsive Phase Spectrometer (**SIPS**)	1 to 9Å	Full Sun	Flat and bent crystals, position-sensitive proportional counters

All the instruments have a considerable heritage of study, development, and flight experience. Balloon versions of **GRID** and **HIGRANS** are currently being developed and are expected to be flown in the near future. The Fourier-transform imaging technique used in **GRID** has been extensively studied for the **Pinhole/Occulter Facility**. **LEIS** is based on the design of the Solar

EUV Telescope and Spectrometer (SEUTS) developed at NASA-GSFC. SIPS is a considerably more sensitive version of the SMM-Bent Crystal Spectrometer (BCS) and the P78-1 SOLFLEX instrument.

The two high-energy instruments, although optimized for solar flare bursts, are also able to make important new cosmic observations, particularly of transient phenomena. They could also be modified to provide very high sensitivity cosmic observations, comparable in quality to observations from the best instruments designed exclusively for that purpose. An attractive and cost-effective possibility is to design SHAPE so that GRID and HIGRANS could be easily refurbished for cosmic observations after 1995, when solar flare activity should greatly decrease. LEIS and SIPS are both powerful instruments for observations of the nonflaring Sun and so could provide valuable observations even during the minimum in solar activity.

Other aspects of the SHAPE program would follow the highly successful approach adopted for SMM. The four SHAPE instruments would be designed and built by separate principal investigator teams with clean interfaces to the spacecraft. Each instrument team would have its own computer for prelaunch testing and postlaunch instrument control and data analysis. Communication among the scientific teams and with ground-based observers and the rest of the interested scientific community would be assured by the free exchange of data between computers and extensive collaborative data analysis, in a manner pioneered in the SMM Experimenters' Operations Facility. The convenient exchange of data, images, and text made possible by modern computer networking will add new dimensions to the involvement of guest investigators.

In many respects, SHAPE will be simpler and less expensive than SMM. Since all the instruments view the whole Sun (LEIS has an internal gimballed mirror to allow it to scan the whole Sun), the spacecraft can be kept pointed at Sun-center for all the solar observations. Consequently, the operations should be greatly simplified compared to SMM, where the pointed instruments observed only small fractions of the solar disc, and the spacecraft pointing had to be constantly adjusted to keep the most promising active region in the fields of view. The pointing tolerance of the SHAPE instruments is much less severe, about 2 arcminutes compared with $\leq$2 arcseconds for SMM. The aspect must be determined with greater accuracy than for SMM – 0.2 arcseconds compared with 1 arcsecond – but, for the solar observations, it will be provided by the aspect sensor built into the GRID instrument. For the nonsolar observations, the aspect will be determined from the spacecraft star tracker with an accuracy to be determined in a Phase A study.

If the SHAPE instruments are exchanged in orbit with a payload already on the MMS, then it may be possible to carry the individual instruments to orbit in load-isolation canisters, thus significantly reducing the environmental design requirements and, hence, the cost of the instruments.

The total data rate from the SHAPE instruments will be higher than the SMM rate with a peak of about 2 Mbps, but inclusion of the two standard 10^9-bit tape recorders will allow the data for a flare to be stored for later high-speed playback. Data handling and compression methods will be investigated during the Phase A study.

It is clear that the SHAPE payload poses no great new technological challenges, and instrument development is already well under way. Consequently, we believe that the SHAPE payload can be built, with the help of extensive European participation, at a cost within the constraints of the Explorer program. Preliminary cost estimates made by the instrument teams and by the GSFC Resource Analysis Office indicate that this is indeed the case.

4.1 Gamma-Ray Imaging Device – GRID

The **GRID** instrument, shown schematically in Figure 4.1, has significant new capabilities for solar and cosmic high-energy astronomy.

Solar Flare Studies. The primary objectives of **GRID** for solar flare observations are:

- Identification of sites of particle acceleration and interaction.
- Study of temporal and spatial development of both the thermal and nonthermal electron components of solar flares.
- Imaging of the accelerated nucleon component of strong solar flares.

To date, solar hard X-ray images have been limited to a resolution of 8 arcseconds and to energies below 40 keV. **GRID** will have 5 times better angular resolution, the capability of imaging solar flares to energies as high as 1 MeV, and a factor of 1000 improvement in sensitivity over **HXIS** on **SMM**. The high sensitivity will, for the first time, allow studies of flares to be made on arcsecond size scales and subsecond time scales comparable to those associated with the magnetic structures and with the processes that modify the electron spectrum (see Section 2.1). The high sensitivity and full Sun coverage of **GRID** will allow the spatial study of many flares per month, thus providing a large sample of high-energy flares for statistical analysis (see Appendix A).

Galactic and Extragalactic Source Studies. The observational objectives of **GRID** for high-resolution hard X-ray and γ-ray imaging include:

- Determination of the energetic particle distribution in supernova remnants.
- Study of the spatial structure of active galactic nuclei at energies above 10 keV, including determination of the ratio of core to jet emission.
- Localization of hard X-ray and γ-ray sources in the galactic center region, including the positron-annihilation source and repeating soft γ-ray bursters.
- Study of the spatial structure of hard X-ray emission in clusters of galaxies.

In addition to its high angular resolution, **GRID** also has excellent broad-band coverage (5 keV - 1 MeV), high sensitivity, and good time resolution. It will be able to image numerous bright sources of hard X-ray emission, achieving a 3σ sensitivity for each subcollimator of $\sim 4 \times 10^{-6}$ photons cm^{-2} s^{-1} keV^{-1} at 100 keV for an observation lasting for 10^5 s. Interesting sources for observation up to at least 100 keV include the galactic center, the Crab, 3C273, the Virgo and Perseus Clusters, NGC 1275, NGC 4151, and Cen A.

Instrument Characteristics. **GRID** is based on a Fourier-transform imaging technique described in Appendix A. Two widely spaced, fine-scale grids create a large-scale modulation pattern of high-energy photons which can be measured with a detector having only moderate spatial resolution. This modulation pattern contains the phase and amplitude information for a single Fourier component of the source distribution. Multiple grid pairs with a variety of slit spacings and angular orientations are used to sample numerous Fourier components. An image is constructed from these Fourier components in exact analogy to multi-baseline radio interferometry.

Table 4.1 summarizes the **GRID** instrument parameters. The basic design uses 34 grid pairs to measure 34 separate Fourier components corresponding to angular size scales of 1.5 arcseconds to 3 arcminutes. Each grid pair sub-collimater has two position-sensitive detectors with overlapping energy coverage: a xenon multiwire proportional counter for X-ray energies up to 50 keV, and a NaI(Tl) detector for higher energies up to 1 MeV (see Appendix A for more details).

Table 4.1 GRID instrument parameters

Technique ..... Fourier-transform imaging	X-ray detectors ..... Position-sensitive multiwire
	(5 to 50 keV) proportional chambers
Angular resolution .. 1.5 arcsec	(3 cm × 10 cm × 10 cm)
Field of view ..... Full Sun (0.6 degrees)	γ-ray detectors ..... NaI(T*l*) scintillation cameras
	(30 keV to 1 MeV) (2 cm × 10 cm × 10 cm)
Boom length ..... 7 m	
	Total detector area .. 3400 cm^2
Parameters of grids	
Number of pairs ... 34	Sensitivity
Slit spacings ..... 50 μm to 6 mm	(5 to 40 keV) ..... 1000 × HXIS
(1.5 arcsec to 3 arcmin)	(>40 keV) ..... Totally new capability
Upper dimensions .. 17 cm × 17 cm	~2 flares per day
Lower dimensions .. 10 cm × 10 cm	
Thickness ..... 1 cm	Aspect sensors ..... Solar Disk Sextants
Material ..... Tungsten	(see Appendix A)

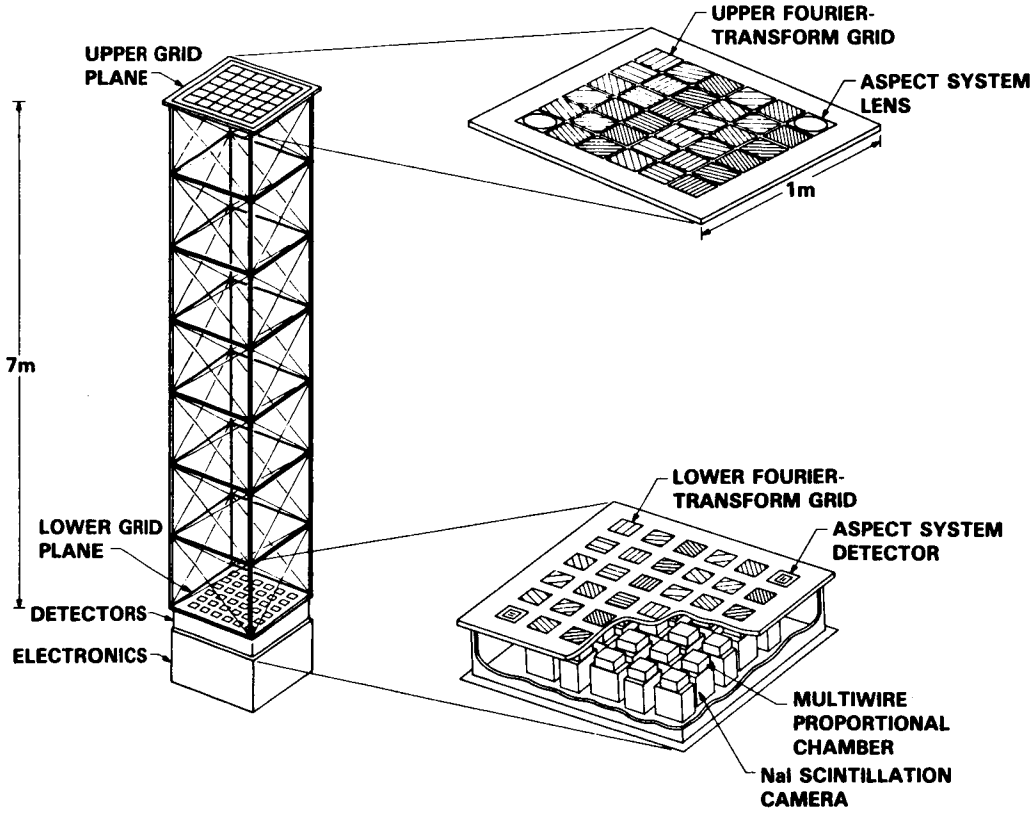

Figure 4.1. Schematic of GRID.

4.2 High-Resolution Gamma-Ray and Neutron Spectrometer – HIGRANS

The primary objectives of **HIGRANS** are as follows:

- High-resolution spectroscopy of solar flare γ-ray lines from 300 keV to 20 MeV.
- High-resolution flare X-ray and γ-ray continuum measurements from 10 keV to >20 MeV, and moderate-resolution γ-ray continuum measurements to >100 MeV.
- Flare neutron measurements from 20 MeV to 1 GeV.

Nonsolar objectives include high spectral and high temporal resolution observations of cosmic γ-ray bursts and other transient sources, including accurate measures of cyclotron lines, gravitationally red-shifted positron annihilation lines, and other spectral features. It will also monitor longer timescale transient line features from other sources such as SS433, the Crab pulsar, and the galactic center, as well as steady line sources such as the ^{26}Al line from explosive nucleosynthesis.

HIGRANS, shown schematically in Figure 4.2, is designed to provide spectral resolution of a factor of about 50 higher than previous NaI(Tl) γ-ray spectrometers, sufficient for accurate measurement of all parameters of the expected γ-ray lines with the exception of the neutron capture deuterium line, which has an expected FWHM of about 0.1 keV. The instrument is optimized for spectroscopy of solar γ-ray and hard X-ray bursts, which typically have durations of 10 to 1000 s. Thus, high count-rate capability and wide dynamic range are required, while background rejection must be good, but not outstanding. In particular, a wide field of view (120° FWHM), appropriate for the non-solar burst objectives, is acceptable from background considerations. The sensitivity of **HIGRANS** for measurements of narrow γ-ray lines, hard X-ray and γ-ray continua, and flare neutrons is a factor of 5 to >10 higher than that of **SMM** instrumentation.

The instrument consists of an array of high-purity, n-type coaxial germanium detectors (HPGe) cooled to 90 K and surrounded by bismuth germanate (BGO) and plastic scintillator anticoincidence shields. Electrical segmentation of the HPGe detector into a thin front segment and a thick rear segment, together with pulse-shape discrimination, provides optimal dynamic range and signal to background characteristics for flare measurements over the energy range from 10 keV to 20 MeV. Neutrons and >20 MeV γ-rays are detected and identified with the combination of the HPGe detectors and rear BGO shields. Table 4.2 gives the parameters of **HIGRANS**; further details on the instrument and its current state of development are given in Appendix B.

Table 4.2. HIGRANS instrument parameters

Energy range	
γ-rays and hard X-rays	10 keV to 20 MeV (high-resolution HPGe) 20 MeV to >100 MeV (medium resolution BGO)
Neutrons	20 MeV to 1 GeV
Energy resolution	0.6 to 5 keV FWHM (high-resolution HPGe)
Total detector area	340 cm^2 HPGe, 1400 cm^2 BGO
Field of view	120° FWHM
Shields	5-cm-thick BGO on sides, three 5-cm thick BGO at rear, 1-cm-thick plastic scintillator over 4π steradians
Germanium detector cooling	90 K for 3 years with solid-cryogen cooler

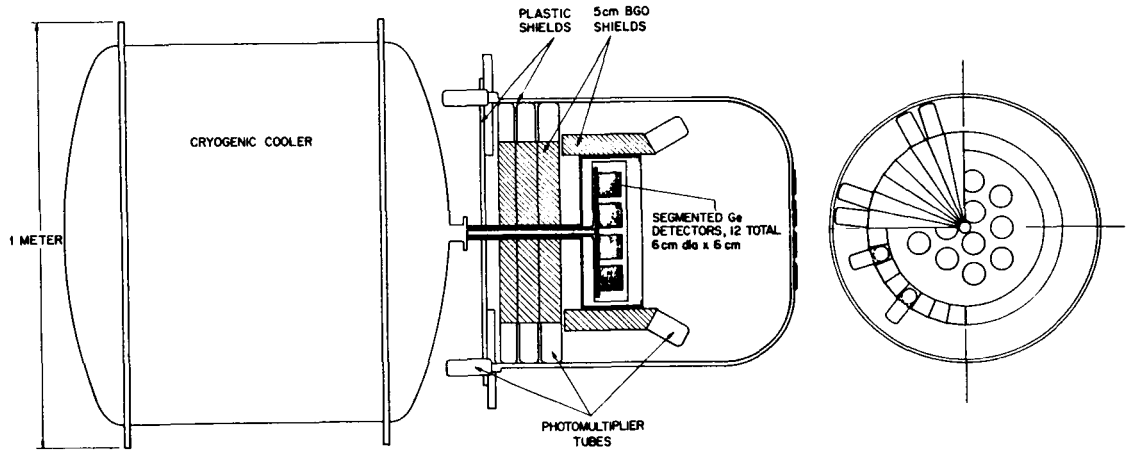

Figure 4.2. Schematic of **HIGRANS**.

4.3 The Low-Energy Imaging Spectrometer – LEIS

LEIS is designed to provide comprehensive measurements of the geometry and plasma properties of solar material throughout the temperature range from 8×10^3 K to 2×10^7 K. It is the first solar physics instrument with the capability of obtaining high spatial and spectral resolution data with high time resolution in both the UV and EUV wavelength ranges simultaneously. The wide temperature coverage will be achieved by observing in the UV and EUV wavelength bands from 240 to 285 Å and 1200 to 1425 Å, respectively. **LEIS** will be used to make unique observations, important to many areas of solar physics discussed in Section 2 including flares, preflare activity, active regions, coronal bright points, and the quiet Sun. Major science objectives for **LEIS** include the following:

- Determine the preflare magnetic field configuration.
- Determine the relationship of the high-energy accelerated particles to the thermal flare.
- Evaluate flare energetics and plasma diagnostics.
- Test for the presence of beams of protons with energies between ~10 keV and 1 MeV.

The ability to make monochromatic images over this broad temperature range will allow the first detailed observations of preflare loop structures to be made with **LEIS**. During the impulsive phase, images taken with **LEIS** in UV transition zone lines such as Si IV will reveal the sites of chromospheric heating due to energy deposited by high-energy electrons. These sites should be the footpoints and sources of evaporation for the thermal coronal flare plasma that produces the soft X-ray flare. These observations can be combined with the **GRID** images to give a complete picture of the geometry of the high-energy flare. The UV images, combined with the EUV images in spectral lines such as Fe XXIV (2×10^7 K), which indicate the locations, sizes, and orientations of the soft X-ray flare loops, will directly test the chromospheric evaporation hypothesis.

As discussed in Section 2, there is considerable interest in whether or not proton beams exist at energies below ~1 MeV and, if they exist, with what intensity. The only way that we have for detecting such protons is by studying the shape of the Lyman-α line. The Lyman-α emission from the de-excitation of the hydrogen atoms formed by charge exchange between ambient atoms and downward-moving protons will be red-shifted for flares observed near Sun center. Thus, the Lyman-α line will exhibit a characteristic asymmetry, which can be accurately measured with **LEIS**, and which gives an indication of the presence and intensity of protons with energies down to ~10 keV.

The two **LEIS** wavelength ranges have been chosen to cover spectral lines important from the diagnostics standpoint. For example, observations of the UV intersystem lines, O V, S IV, and O IV, together with allowed lines of Si IV and N V, enable the electron density of the regions heated by electron beams to be determined. Similarly, the EUV lines of Fe IX are excellent indicators of electron density for plasma near 10^6 K. In addition, the intensities of the measured lines covering a broad temperature range can be used to determine the differential emission measure distribution, which can be related to energy transport processes and dynamics in the flare plasma. Finally, **LEIS** can be used to measure line broadening and Doppler shifts due to plasma turbulence and bulk motions, respectively.

LEIS, shown schematically in Figure 4.3, consists of an off-axis parabola operating as a prime-focus telescope, a slit assembly, a toroidal-grating assembly, and an imaging detector. Functionally, **LEIS** operates as a high-speed stigmatic spectroheliograph. The primary mirror has a 2-m focal length, and is articulated, permitting the optic axis of the telescope to be pointed to any position

on the solar disk without moving either the instrument or the spacecraft. The grating assembly contains two toroidal gratings, one operating in the UV, the other in the EUV. The detector is a phosphor-sensitized intensified television camera based on a Plumbicon tube. Tapered fiber-optic lenses are used to match the 1×1 arcsecond pixel size required at the focal plane to the pixel size required by the intensifier and Plumbicon sections. The Plumbicon readout electronics are designed to permit selective addressing of areas of the focal plane, so that only the desired spectral lines are read out to the data system. The instrument is controlled by a microprocessor which sequences the operation of the primary mirror, the entrance slit mechanism, the detector control electronics, and the data handling system.

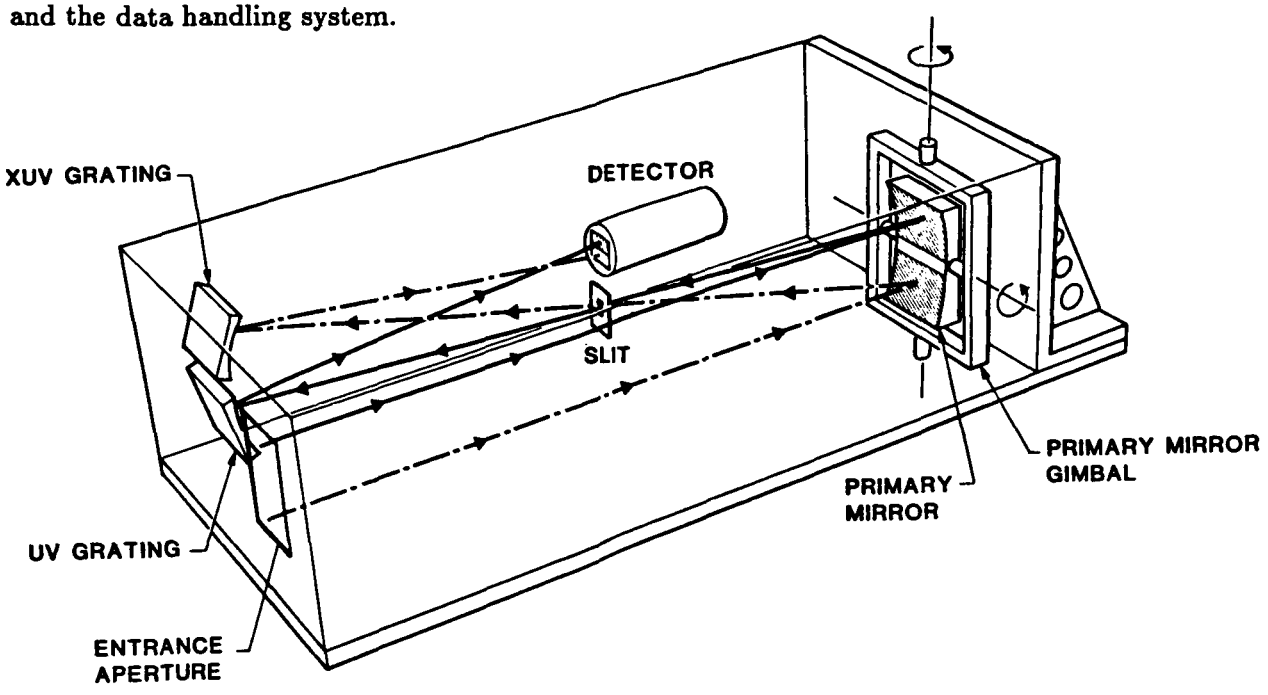

Figure 4.3. Schematic of **LEIS**.

The primary mirror is a rectangular section cut from a paraboloid of revolution and defines two collecting areas. The lower collecting area is coated to optimize for EUV reflectivity, while the upper area is optimized for UV reflectivity. Since they are part of the same parabolic surface, the UV and EUV images are rigorously co-aligned on the entrance slit of the spectrograph. The chief rays, defined by lines from the center of each section to the center of the entrance slit, converge toward the entrance slit and then separate again inside the spectrograph, as shown in Figure 4.3. This feature of the telescope allows the two sections of the spectrograph to operate simultaneously and independently.

To create a spectroheliogram, one observes a sequence of spectrograms, moving the primary mirror between each so that the slit sweeps across the desired area of the solar disk. A spectroheliogram can have any desired width and can be centered about any position on the disk. The basic sampling rate of the detector is 2×10^4 spectral elements per second. (One spectral element corresponds to an intensity measurement at one wavelength for each of the 480 UV or EUV spatial elements.) These rates would allow us to sample about 40 spectral elements distributed between the UV and EUV image planes while completing a full 8×8 arcminute spectroheliogram in 1 s. The system can also operate in a slitless spectrograph mode for higher sensitivity.

4.4 Soft X-Ray Impulsive Phase Spectrometer (SIPS)

The **SIPS** instrument (shown in Figure 4.4) consists of eight high-sensitivity bent-crystal spectrometers (**HSBCS**) and two high-sensitivity flat-crystal spectrometers (**HSFCS**). The wavelength coverage is given in Table 4.3.

Table 4.3 Principal characteristics of **SIPS**

Instrument	Channel	Wavelength Coverage (Å)	Number of Detectors	Spectral Resolution ($\lambda/\delta\lambda$)
HSBCS	Ca XVIII–XIX	3·160 – 3·235	3	5000
	Fe XXII–XXV	1·840 – 1·985	3	12500
	Fe XXVI	1·769 – 1·796	2	5000
HSFCS	Low Temp.	1·0 – 9·0	1	15000
	High Temp.	1·0 – 4·0	1	15000

SIPS will provide, for the first time, soft X-ray spectra on a timescale characteristic of the impulsive phase ($\leq$1 s). This is accomplished with a factor of 10 greater sensitivity than was available from the corresponding channels of the **SMM–BCS**, thus allowing the following new measurements to be made, all with exceptionally high time resolution throughout the flare:

- Measurements of turbulent and bulk plasma motions before, during, and after the impulsive phase.
- Measurements of the dynamics, temporal evolution, and the differential emission measure of the thermal plasma, including the superhot component.
- Measurements of the transient ionization to provide density estimates of the high-temperature ($>10^7$ K) plasma.
- Highly accurate measurements of the abundance of about a dozen elements in the soft-X-ray-emitting plasma.

The mechanical structure for the **HSBCS** will be largely identical to that of the **SMM–BCS**. It will consist of the eight curved crystal assemblies and eight corresponding one-dimensional position-sensitive proportional counters. An attractive feature of the bent-crystal design is that it requires no moving parts and is, thus, highly reliable. The multiplicity of similar channels also adds redundancy as well as sensitivity. The instrument will view the entire Sun.

The **HSFCS** will be a scanning Bragg crystal spectrometer. The design will be a greatly improved version of the **P78–1** spectrometer (**SOLFLEX**). The two **HSFCS** crystals are independently driven and will have effective areas about 6 times greater than those of the **SOLFLEX** spectrometers. The **HSFCS** spectrometers will scan any selected wavelength range between 1 and 9 Å. The complete range can be scanned in about 5 minutes.

The **HSBCS** will use germanium crystals with the same two cuts as used for the **SMM–BCS**. These crystals can be easily bent and provide high spectral resolution and reflectivity. Other crystals with higher reflectivity and spectral resolution will also be considered. One of the **HSFCS** spectrometers will include a germanium crystal to provide in-orbit cross-calibration of wavelength dispersion with **HSBCS**. The 1–9 Å **HSFCS** channel will use an ADP crystal. The **HSBCS** detectors will be sealed, one-dimensional position-sensitive proportional counters. The position

resolution of the detectors will be increased fourfold over the **SMM–BCS** by making use of a modified wedge and strip design for the readout. The double wedge readout provides low thermal noise, low distortion, and good linearity. The **HSFCS** will use two standard sealed proportional counters.

The digital electronics design, which will be similar to that of the **SMM–BCS**, will include a microprocessor-based system and will control data acquisition and transmission for both **HSBCS** and **HSFCS**. The microprocessor adds flexibility to the instrument, making it possible to vary the temporal and spectral resolution of the different channels, coordinate flare observations between the two spectrometers and the rest of the payload, and optimize the overall performance. Alternatively, the data can be processed at a higher rate and put in a queued memory store for later transmission; this can improve the time resolution in all channels during the impulsive phase. This microprocessor makes possible in-orbit software modifications, real-time processing of the data, and flare alerts to other instruments on board. Much of the analysis software developed for the **SMM–XRP** can be directly adapted for use with **SIPS** data, thus achieving equivalent savings to that obtained by using existing mechanical and electronic designs.

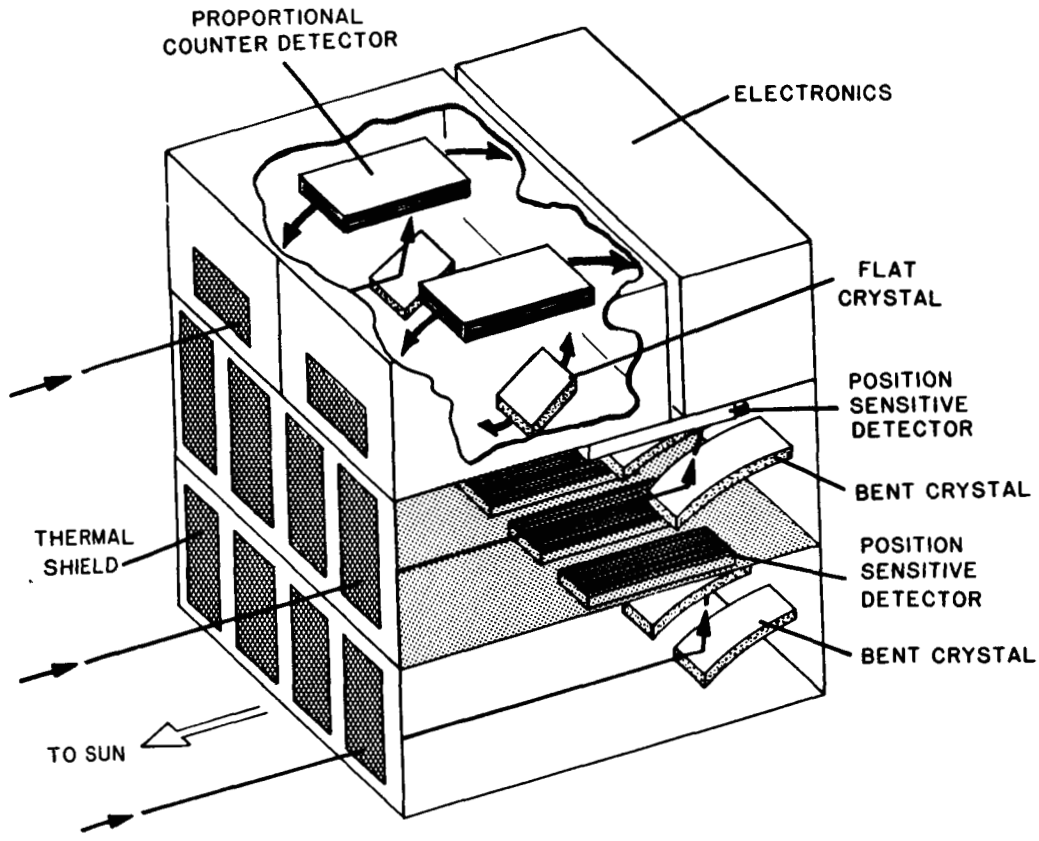

Figure 4.4. Schematic of **SIPS**

FOLDOUT FRAME 1

MAGNETIC DISSIPATION

ELECTRON ACCELERATION

PROTON ACCELERATION

PLASMA HEATING

PLASMA MOTIONS

RADIO AND OPTICAL EMISSION

UV/XUV LINES

X-RAY LINES

X-RAY CONTINUUM

γ-RAY CONTINUUM

NUCLEAR γ-RAY LINES

NEUTRON EJECTION

INTERPLANETARY PROTONS AND ELECTRONS

GROUND-BASED TELESCOPES

GRID

ISTP AND NEUTRON MONITORS

FOLDOUT FRAME 2

LEIS

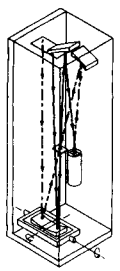

LOW-ENERGY IMAGING SPECTROMETER

SIPS

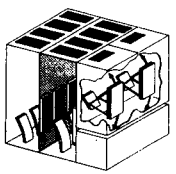

SOFT X-RAY IMPULSIVE PHASE SPECTROMETER

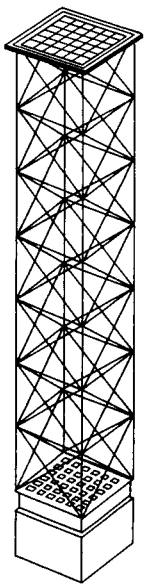

GAMMA-RAY IMAGING DEVICE

HIGRANS

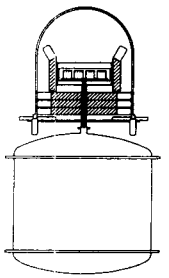

HIGH-RESOLUTION GAMMA-RAY AND NEUTRON SPECTROMETER

SHAPE

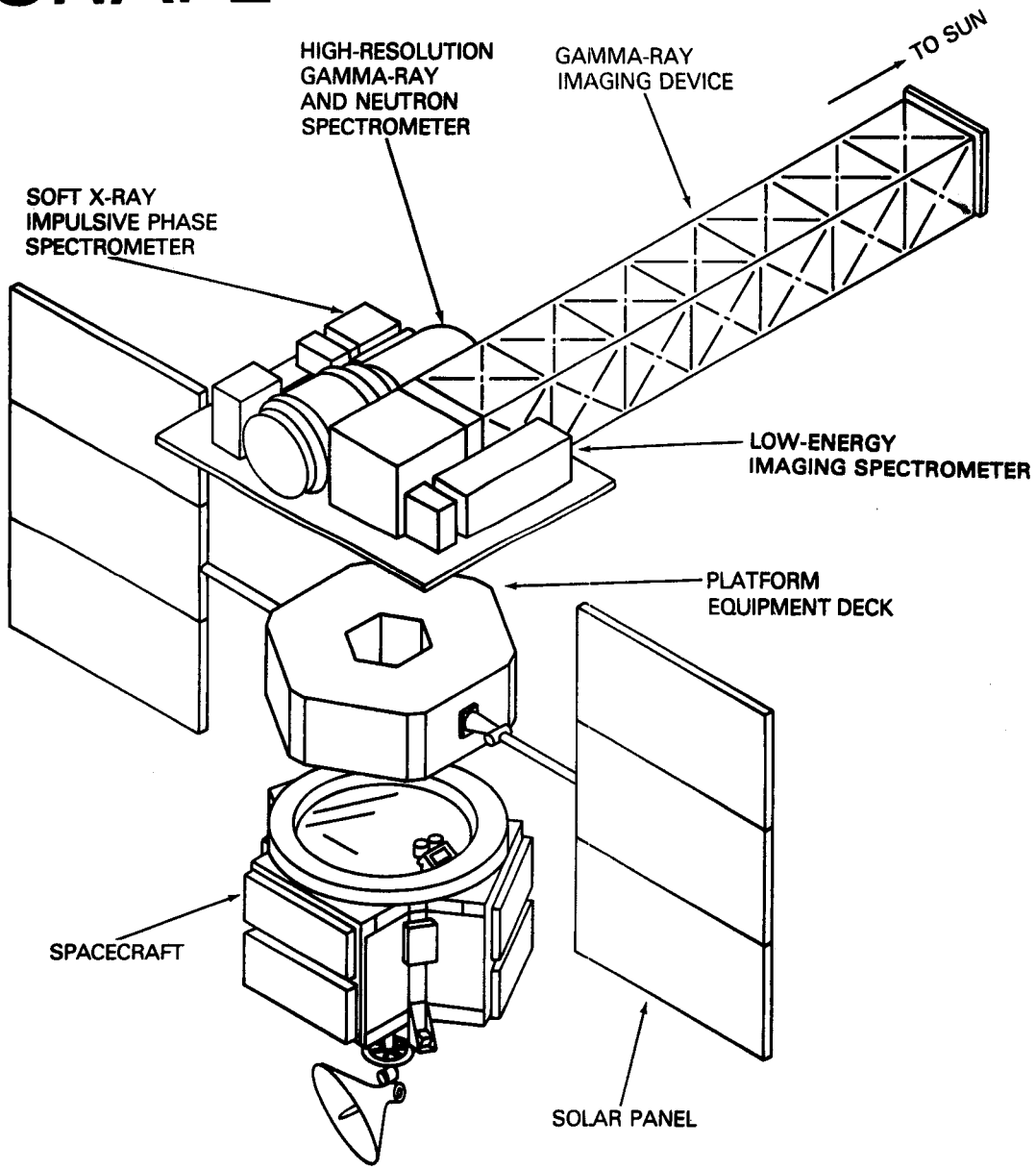

3 FOLDOUT FRAME

SOLAR HIGH-ENERGY ASTROPHYSICAL PLASMAS EXPLORER

5. STATEMENT OF WORK

The goal of the Phase A study is to produce a detailed conceptual design of the four instruments that make up the **SHAPE** payload and to define the solar and cosmic scientific objectives of such a mission. The study will include the identification of mission, spacecraft, and operations requirements. A management approach will be recommended and a cost estimate will be developed for each instrument and for the complete mission.

The proposed Phase A study will be conducted under the overall direction of the Principal Investigator at Goddard Space Flight Center with the Lead Scientists coordinating studies of the four different instruments and the theoretical support. A study of **SHAPE** as a coordinated mission will be conducted at GSFC in order to plan the integration of the instruments onto an **MMS** spacecraft and to determine what test and evaluation procedures will be required. A plan will be developed for in-orbit operations including commanding the instruments, handling the data on the spacecraft, and analyzing it on the ground.

To coordinate these Phase A activities, two general meetings will be held at GSFC, in September 1987 and in June 1988. Instrument team meetings will be held in conjunction with these general meetings and also at other times during the year-long study as required by the team leaders. The schedule of the Phase A activities is as follows:

1st Quarter: Organizational meeting, definition of detailed technical issues.

2nd Quarter: Baseline design definition, development of management approach.

3rd Quarter: Detailed costing of instruments, independent review of conceptual designs.

4th Quarter: Preparation of final report.

Quarterly reports will be written by each team leader and these will be assembled by the PI for presentation to the Study Office. Technical information and study feedback from the Study Office will also be channelled through the PI to the team leaders.

The final report will contain the following sections:

(1) a comprehensive conceptual design for the instruments.

(2) an approach for instrument development, fabrication, and test.

(3) identification of the mission, spacecraft, and operation requirements.

(4) detailed definition of the solar and cosmic scientific objectives. and

(5) a management approach and cost estimate.

In addition to the Co-Investigators listed on the title page of this proposal, a number of other people have agreed to act as Associated Scientists for the Phase A study; they are listed in the statements of work for each instrument. Such a large scientific team is appropriate for this planning stage, when it is important to consider a wide variety of ideas for future observations. One of the major tasks of the Phase A study will be to identify a smaller management team to be responsible for the hardware in Phase B and Phase C/D. A management plan will be developed for each instrument and for the overall payload. It will be decided where the major components of each instrument will be built, and where each instrument and the overall payload will be integrated and tested. The decisions will be based on scientific quality, cost minimization, efficiency, and the availability of the required expertise and capabilities.

5.1 Statement of Work for the Overall Mission

We assume, for the purposes of this proposal that the spacecraft will be an **MMS**, although any similar three-axis stabilized spacecraft could be used. A list of mission-wide concerns to be studied during Phase A follows with names of the responsible scientists. Appropriate technical support will be available at GSFC to assist in these studies.

- Develop verification requirements for instrument and payload environmental tests. (L. Orwig)
- Study thermal control of individual instruments and of the overall payload. (M. Bruner)
- Determine co-alignment requirements between the different instruments, particularly **GRID** and **LEIS**, and establish how these can be achieved. (T. Prince, M. Bruner, E. Maier)
- Establish a plan to obtain coordinated ground-based radio and optical observations with absolute time determined to better than 1 ms throughout the observations. (B. Dennis, H. Hudson)
- Study the arrangement of the instruments on the platform equipment deck to ensure minimum interference between instruments and gravity-gradient torques that can be handled by the spacecraft reaction wheels. (L. Orwig)
- Develop a plan for solar observations that will have the minimum number of different instrument operating modes consistent with achieving the scientific objectives. (H. Hudson, C. Crannell, M. Bruner, K. Strong)
- Develop a plan for nonsolar observations taking into account the limitations on the offset pointing capabilities of the spacecraft. (K. Wood, R. Lingenfelter)
- Study the commands, data rates, and on-board data storage requirements. (L. Orwig, R. Shine)
- Establish a plan for postlaunch operations and data analysis to ensure free and prompt access to the data and analysis software by all interested scientists. This will include studies of the required computing facilities, software support, and manpower requirements. (B. Dennis, R. Shine, K. Strong)
- Make estimates of instrument and overall mission costs. (C. Crannell)

5.2 Statement of Work for GRID

T. Prince (lead scientist)	California Institute of Technology (CIT)
C. Crannell, B. Dennis, L. Orwig	NASA – Goddard Space Flight Center (GSFC)
A. Dean	Southampton University (SU), UK
J. L. Culhane	Mullard Space Science Laboratory (MSSL), UK
E. Fenimore	Los Alamos Scientific Laboratory (LASL)
H. Hudson	University of California at San Diego (UCSD)
G. Hurford	California Institute of Technology (CIT)
E. Maier	NASA – Goddard Space Flight Center (GSFC)
G. Simnett	University of Birmingham (UB), UK
S. Sofia	Yale University Observatory (YUO)
E. Tandberg-Hanssen, J. Dabbs	NASA – Marshall Space Flight Center (MSFC)
F. van Beek	Delft University of Technology (DUT), The Netherlands
K. Wood	Naval Research Laboratory (NRL)

The following specific technical issues concerning **GRID** will be studied by the indicated institutions with technical support provided by GSFC and MSFC:

NaI(Tl) detectors/analog electronics	CIT, SU
Proportional chambers	UB, MSSL
Digital electronics/data handling	CIT, GSFC, UB
Grid fabrication	DUT, GSFC, LASL, NRL
Structure/thermal control/integration and test	MSFC
Alignment/aspect	YUO, DUT, GSFC
Imaging simulations	CIT, GSFC, LASL
Data reduction/distribution	CIT, GSFC, UCSD

International collaboration is anticipated in the following three areas: F. van Beek of the Netherlands will be responsible for studies of grid fabrication, G. Simnett and L. Culhane of the UK will be responsible for design of the proportional chamber system, and A. Dean of the UK will participate in studies of scintillation detectors.

5.3 Statement of Work for HIGRANS

R. Lin (lead scientist)	University of California, Berkeley (UCB)
E. Chupp, P. Dunphy, D. Forrest	University of New Hampshire (UNH)
C. Crannell, L. Orwig	NASA - Goddard Space Flight Center (GSFC)
K. Hurley	CESR, Toulouse, France
S. Kane, R. Pehl,	University of California, Berkeley (UCB)
J. Matteson, R. M. Pelling	University of California, San Diego (UCSD)
C. Reppin, G. Kanbach, E. Rieger	Max Planck Institute, Garching (MPI), FRG
G. Share, K. Wood	Naval Research Laboratory (NRL)

The specific technical areas identified for study, and the institutions involved are (lead institution listed first):

Segmented HPGe detectors/analog electronics	UCB
Cryostat and mechanical structure for HPGe	UCB, UCSD
Cryogenic cooler	UCB, GSFC
BGO shield design	UNH, CESR, MPI
BGO elements and electronics	CESR
Instrument calibration	UNH, UCB
Instrument mechanical structure	MPI
Digital electronics/data handling	GSFC, UCB
Data reduction/distribution	GSFC
Integration and test	GSFC
Instrument background studies	NRL, UCB

Strong international collaboration is anticipated during the study phase, and roughly half of the instrument (both the BGO and plastic shields, all associated electronics, and instrument mechanical structure) is expected to be obtained from Europe.

5.4 Statement of Work for LEIS

M. E. Bruner (lead scientist)	Lockheed Palo Alto Research Laboratory (LPARL)
J. Bartoe, G. A. Doschek	Naval Research Laboratory (NRL)
L. Golub	Smithsonian Astrophysical Observatory (SAO)
G. Holman, R. Thomas	NASA – Goddard Space Flight Center (GSFC)
R. Moore	NASA – Marshall Space Flight Center (MSFC)
R. Shine, K. T. Strong	Lockheed Palo Alto Research Laboratory (LPARL)

The following specific identified for study and the institutions involved are:

Optical design	
• Spectral ranges and resolution	NRL, LPARL
• Spatial resolution	NRL, LPARL
• Ray tracing and design optimization	GSFC
• Mirror coatings	GSFC, LPARL
Cost analysis	LPARL, NRL, SAO
Detector tradeoff study	SAO, LPARL, GSFC
UV section optical design	LPARL, NRL
Instrument system approach	LPARL, GSFC, NRL, SAO
Observing modes	LPARL
Identification of auxiliary studies & observations	GSFC, NRL, LPARL
Stray light control	NRL, LPARL, GSFC

5.5 Statement of Work for SIPS

J. L. Culhane (lead scientist)	Mullard Space Science Laboratory (MSSL), UK
R. C. Catura, K. T. Strong	Lockheed Palo Alto Research Laboratory (LPARL)
A. M. Cruise, K. J. H. Phillips	Rutherford Appleton Laboratory (RAL), UK
G. A. Doschek, U. Feldman	Naval Research Laboratory (NRL)
J. R. Lemen, J. H. Parkinson	Mullard Space Science Laboratory (MSSL), UK

The SIPS instrument will be studied by an international consortium consisting of four groups. The division of responsibilities during the study closely matches the modular sub-components of the instrument. The study will define scientific objectives and provide a comprehensive design for the instrument, plans for testing and integration, and operational plans for the mission and data reduction. The specific technical areas identified for study, and the institutions involved are:

HSBCS mechanical structure	MSSL
HSBCS crystal assemblies	RAL
HSFCS mechanical structure, crystal assemblies	NRL
Detectors and analog electronics	MSSL
Digital electronics and distribution	LPARL
Integration and test	MSSL, NRL, LPARL
Instrument calibration	MSSL, NRL, RAL
Data reduction and distribution	MSSL, NRL, LPARL, RAL

5.6 Statement of Work for the Theoretical Support Team

R. Ramaty (lead scientist)	NASA – Goddard Space Flight Center (GSFC)
G. A. Doschek	Naval Research Laboratory (NRL)
G. Emslie	University of Alabama in Huntsville (UAH)
R. Lingenfelter	University of California at San Diego (UCSD)

The Theoretical Support Team will conduct a Phase A Study of the scientific objectives of **SHAPE** in order to refine the observational goals of the instrument teams.

6. SHAPE COST PLAN

In the following section the **SHAPE** costing plans are described. Table 6.1 is a summary of the overall costs of the Phase A study to **NASA** in 1986 dollars. These costs and manpower requirements are broken down in detail for each instrument team and the theoretical support group in Table 6.2. Estimates of the European costs have been made, based on current exchange rates. Table 6.3 shows the **GSFC** manpower and resources requirements for Phase A. The **SHAPE** travel budget breakdown for payload meetings at **GSFC** is listed in Table 6.4. The travel requirements for experiment team meetings, if any, are contained in the relevant institution's budget, which are summarized at the end of this section and based on their statement of work (see Section 5).

Table 6.1: Summary of Phase A Costs to NASA for SHAPE

INSTITUTION	COST ($K)	MANPOWER (MM)
GSFC	38	75.6
IMS	47	
Travel (non-civil service)	25	
Cal Tech (**GRID**)	72	6.5
Berkeley (**HIGRANS**)	40	5.5
UNH (**HIGRANS**)	20	0.6
NRL (**HIGRANS**)	5	0.8
LPARL (**LEIS**)	78	5.4
LPARL (**SIPS**)	35	2.4
NRL (**SIPS**)	35	2.0
UCSD (Theory)	5	0.8
TOTAL	400	99.6

MM ≡ Man months of effort

European costs (not including salaries):		
Max Planck Institute (**HIGRANS**):	DM 100K	(~$ 40K)
CESR, Toulouse (**HIGRANS**):	FF 200K	(~$ 30K)
MSSL, UCL, UK (**SIPS**):	£ 20K	(~$ 30K)
TOTAL European Costs		(~$100K)

Table 6.2 Cost Breakdown by Instrument

INSTRUMENT	INSTITUTION	COST ($K)	MANPOWER (MM)
GRID			
	Cal Tech	72	6.5
	GSFC	11	18
TOTAL for GRID		83	24.5
HIGRANS			
	UCB	40	5.5
	UNH	20	
	NRL	5	
	GSFC	20	32.4
TOTAL for HIGRANS		85	37.9
LEIS			
	LPARL	78	
	GSFC	12	11
TOTAL for LEIS		90	11
SIPS			
	LPARL	35	2.4
	NRL	35	2
TOTAL for SIPS		70	4.4
Theory Group			
	UCSD	5	0.6
	GSFC	8	3.0
TOTAL for Theory		13	3.6

Table 6.3: GSFC Cost and Manpower Estimates in Man Years (MY)

GSFC Code		Mission-wide	GRID	HIGRANS	LEIS
Code 600:					
	D. Burritt	0.05			
	C. Crannell		0.2	0.25	
	B. Dennis	0.3			
	G. Holman	0.1			
	L. Orwig		0.1	0.25	
	R. Ramaty			0.2	
	R. Schmadabeck	0.05			
	R. Thomas				0.2
Code 200:					
		0.1			
Code 700:					
	Electronics and data handling	0.2	1.0	1.0	
	Thermal analysis	0.2		0.6	
	Instrument I & T		0.2	0.4	
	T & E	0.2			
	Optics				0.7
TOTALS		1.2	1.5	2.7	0.9
Total GSFC Civil Service Manpower			6.3 MY		
TOTAL IMS costs @ $7.5K per MY			$47.25K		

ADDITIONAL COSTS:

Mission design analysis	$15K
Thermal analysis	$ 4K
T & E verification requirements	$ 8K
LEIS optical design	$ 5K
Scientific theory postdoctoral support	$ 4K
Computer time (IBM3081)	$ 2K
TOTAL ADDITIONAL COSTS	$38K

Table 6.4: SHAPE Travel Expenses

West Coast	Number of trips East	Estimated Cost
Bruner, Shine	4	$750
Catura	1	$750
Hudson	2	$750
Hurford	2	$750
Kane	2	$750
Lin, Pehl	4	$750
Lingenfelter	1	$750
Matteson, Pelling	1	$750
Prince	4	$750
SUBTOTAL	21 trips	$ 15.8K

East Coast	Number of trips to GSFC	
Chupp, Dunphy, Forrest	4	
Emslie	2	$350
Golub	2	$350
Sofia	1	$350
SUBTOTAL	9 trips	$ 3.2K
	SUBTOTAL	$ 19K
	OVERHEAD @ 34%	$ 6K
TOTAL		$ 25K

BUDGETS FOR INDIVIDUAL SHAPE INSRUMENT TEAMS

a) Lockheed Palo Alto Research Laboratory for LEIS

Total Labor Hours	
Reasearch Scientist	344
Staff Engineer	260
Staff Scientist	280
Total Labor Hours	864
Direct Labor Cost	$ 24,515
Total Overhead Cost	$ 36,895
G & A Cost	$ 9,953
Cost of Money	$ 2,985
SUBTOTAL	$ 74,348
Fixed Fee (5%)	$ 3,568
TOTAL	$77,916

b) Lockheed Palo Alto Research Laboratory for SIPS

Total Labor Hours	
Reasearch Scientist	200
Staff Engineer	177
Total Labor Hours	377
Direct Labor Cost	$ 9,681
Total Overhead Cost	$ 14,547
G & A Cost	$ 3,883
Travel Costs	$ 3,121
Other Direct Costs	$ 600
Cost of Money	$ 1,229
SUBTOTAL	$ 33,061
Fixed Fee (5%)	$ 1,910
TOTAL	$34,971

c) Naval Research Laboratory for SIPS

Total Labor Hours		
	Reasearch Scientist	140
	Consultant (crystals)	80
	Mechanical Engineer	240
	Total Labor Hours	420
Direct Labor Cost		$ 15,100
Total Overhead Cost		$ 15,500
Travel Costs		$ 2,000
Computer Costs		$ 2,000
	TOTAL	$34,600

d) Theoretical Support Group

Total Labor Hours			
	R. Ramaty	400	($2,000)
	R. E. Lingenfelter	100	($5,000)
	R. Murphy	200	($4,000)
	Total Labor Hours	700	
Direct Labor Cost		$ 11,000	
Computer Costs		$ 2,000	
	TOTAL	$13,000	

e) California Institute of Technology for GRID

1) Salaries			
Professorial Faculty	N/C		
Research Scientist	$17,250	1/2	mn-yr
Electronics Engineer	1,600	1/2	mn-mo
Total Salaries	$18,850		
Staff Benefits (@ 29.5%)	5,561		
Total Salaries and Staff Benefits	$24,411		
2) Services and Materials			
Graphics	600		
Materials	700		
Telephone and postage	200		
Total Services and Materials	$ 1,500		
3) Travel			
Three GRID study meetings - MSFC	$ 2,400		
4) Instrument Development Studies (Subcontracts)			
Grid Fabrication demonstration	$10,000		
Imaging simulations	7,500		
Total subcontracts	$17,500		
TOTAL DIRECT COSTS	$45,811		
5) Overhead (58% of TDC)	26,570		
TOTAL	$72,381		

f) University of California, Berkeley for HIGRANS

(October 1, 1987 - September 30, 1988)

A. Salaries and Wages	Man-Months	Monthly Rate†	Amount Requested	
Research Physicist IV(off-scale)/V	0.75	$6016	$4,512	*
	0.50	6629	3,315	*
Research Physicist II	0.25	4788	1,197	*
Senior Development Engineer	0.75	4527	3,395	**
	0.25	4799	1,200	**
Research Assistant	1.25	1839	2,299	Δ
	0.50	1839	920	ΔΔ
	0.75	1949	1,462	ΔΔ
	0.25	1949	487	Δ
Secretary III	0.25	2315	579	**
			$19,366	

B. Employee Benefits	
25.75% of salaries marked *	$2,324
30.75% of salaries marked **	1,591
1.21% of salaries marked Δ	34
1.72% of salaries marked ΔΔ	41
	$3,990

C. Supplies and Expenses	
SSL business services group - 27 hrs. @ $21.15/hr.	$571
- 9 hrs. @ $22.40/hr.	202
SSL drafting services - 16 hrs. @ $26.20/hr.	419
Lawrence Berkeley Laboratory subcontract to support participation of LBL HIGRANS team member (cost-reimbursement):	
LBL Instrument Science Engineering group - 40 hrs. @ $74.60/hr.	2,984
Communications and copying	577
	$4,753

Total Direct Costs	$28,109
Indirect Costs - 42.2% through 6/30/88	$8,897
- 42.6%, 7/1/88 and after	$2,994
TOTAL AMOUNT REQUESTED	$40,000

†Includes anticipated ~5% cost of living increase effective 7/1/86, and 6% increases effective 7/1/87 and 7/1/88.

g) University of New Hampshire for HIGRANS

(September 1987 - September 1988)

Direct Labor:		
Scientific Staff		6,794
Lab Technician		2,352
Consultant Engineer		1,000
	Total Direct Labor:	10,146
Fringe Benefits:		
27% of Salaries		2,469
7.5% of Hourly Labor		75
	Total Fringe Benefits:	2,544
Supplies (see Supplies Estimate):		400
Total Direct Costs		13,090
Indirect Costs (53% of Direct Costs)		6,938
	Total:	20,028

BREAKDOWN OF BUDGET REQUEST

1. Direct Labor Estimate

Research Scientist (20% time)	6,794
Laboratory Technician (10% time)	2,352
Consultant Engineer (50 hrs.)	1,000
	10,146

2. Supplies Estimate

Computer Supplies	250
Electronic Components (Miscellaneous)	150
	255

Note: Travel funds are covered in the overall SHAPE study budget and will be distributed through Goddard Space Flight Center.

7. REFERENCES

Bai, T. 1986, submitted to *Astrophys. J.*

Ballmoos, P. V., Diehl, R., and Schonfelder, V., 1986, submitted to *Astrophys. J.*

Brown, J. C. 1971, *Solar Physics*, **18**, 485.

Brown, J. C., Melrose, D. B., and Spicer, D. S. 1979, *Astrophys. J.*, **228**, 592.

Cane, H. V., McGuire, R. E., and von Rosenvinge, T. T. 1986, *Astrophys. J.*, **301**, 448.

Canfield, R. C., and Chang, C. C., 1985, *Astrophys. J.*, **295**, 275.

Cheng, C. C., Karpen, J. T. and Doschek, G. A. 1984, *Astrophys. J.*, **235**, 1055.

Chupp., E. L. 1984, *Ann. Rev. Astron. Astrophys.*, **22**, 359.

Chupp *et al.* 1982, *Astrophys. J. Letters*, **263**, L95.

Crannell, C. J., Joyce, G., Ramaty, R., and Werntz, C. 1976, *Astrophys. J.*, **210**, 582.

Debrunner, H., Fluckinger, E., Chupp, E. L., and Forrest, D. J. 1983, *Proc. 18th Intern. Cosmic Ray Conf., Bangalore*, **4**, 75.

Dennis, B. R. et al., 1982, *Gamma-Ray Transients and Related Astrophysical Phenomena*, (AIP, New York), R. E. Lingenfelter, H. S. Hudson, and D. M. Worrall (eds), p. 153.

Dere, K. P., Mason, H. E., Widing, K. G., and Bhatia, A. K. 1979, *Astrophys. J. Suppl.*, **40**, 341.

Dermer, C. D., and Ramaty, R. 1986, *Astrophys. J.*, **301**, 962.

Doschek, G. A., Feldman, U., and J.F. Seely, 1985, *M.N.R.A.S.*, **217**, 317.

Doschek, G. A. *et al.* 1986, *Energetic Phenomena on the Sun*, Proc. SMM Workshops, M. Kundu and B. E. Woodgate (eds), NASA CP, in press.

Emslie, A. G. 1981, *Astrophys. J.*, **245**, 711.

Emslie, A. G., Phillips, K. J. H., and Dennis, B. R. 1986, *Solar Phys.*, **103**, 89.

Forman, M. A., Ramaty, R., and E. G. Zweibel, 1986, *Physics of the Sun*, P. A. Sturrock (ed.), vol. II, p. 249.

Forrest, D. J. 1983, *Positron-Electron Pairs in Astrophysics*, M. L. Burns, A. K. Harding, and R. Ramaty (eds), AIP, New York, p. 3.

Forrest, D. J. *et al.* 1985, *Proc. 19th Intern. Cosmic Ray Conf.*, La Jolla, 4, 146.

Holman, G. D. 1985, *Astrophys. J.*, **293**, 584.

Holman, G. D. 1986, *Solar Flares and Coronal Physics Using P/OF as a Research Tool*, E. Tandberg-Hanssen, R. M. Wilson, and H. S. Hudson (eds), NASA CP2421, p. 150.

Holman, G. D. and Kundu, M. R. 1985, *Astrophys. J.*, **292**, 291.

Hoyng, P. *et al.* 1981, *Astrophys. J. Lett.*, **246**, L155.

Hoyng, P., Brown, J. C. and van Beek, H. F. 1976, *Solar Physics*, **48**, 197.

Hudson, H. S., Ohki, K. J., and Tsuneta, S. 1985, *Proc. 19th Intern. Cosmic Ray Conf.*, La Jolla, 4, 50.

Hueter, G. J., 1984, *Energy Transients in Astrophysics*, S. E. Woosley (ed.), AIP, New York, p. 373.

Hurford, G. J. 1986, *Solar Flares and Coronal Physics Using P/OF as a Research Tool*, E. Tandberg-Hanssen, R. M. Wilson, and H. S. Hudson (eds), NASA CP2421, p. 191.

Johnson, W. N., Harnden, F. R., and Haymes, R. C., 1972, *Astrophys. J. Lett.*, **172**, L1.

Kane, S. R., Fenimore, E. E., Klebesadel, R. W., and Laros, J. 1982, *Astrophys. J.*, **254**, L53.

Kiplinger, A. L., Dennis, B. R., Emslie, A. G., Frost, K. J., and Orwig, L. E. 1983, *Astrophys. J.*, **265**, L99.

Kozlovsky, B. and Ramaty, R. 1977, *Astrophys. Lett.*, **19**, 19.

Lea, S. et al. 1981, *Astrophys. J.*, **246**, 369.

Leach, J. and Petrosian, V. 1983, *Astrophys. J.*, **269**, 715.

Leventhal, M., MacCallum, C., and Stang, P. D. 1978, *Astrophys. J.*, **225**, L11.
Lin, R. P., and Hudson, H. S. 1976, *Solar Phys.*, **50**, 153.
Lin, R. P., Schwartz, R. A., Pelling, R. M. and Hurley, K. C. 1981, *Astrophys. J.*, **251**, L109.
Lin, R. P., Schwartz, R. A., Kane, S. R., Pelling, R. M., and Hurley, K. C. 1984, *Astrophys. J.*, **283**, 421.
Mazets, E. P., *et al.* 1981, *Nature*, **290**, 378.
Matz, S. M., *et al.* 1985, *Astrophys. J.*, **288**, L37.
Meyer, J. P. 1985, *Astrophys. J. Suppl.*, **57**, 173.
Murphy, R. J., Ramaty, R., Forrest, D. J., and Kozlovsky, B. 1985, *Proc. 19th Intern. Cosmic Ray Conf.*, La Jolla, 4, 249 and 253.
Murphy, R. J. and Ramaty, R. 1985, *Adv. in Space Research*, **4**, 127.
Nagai, F. and Emslie, A. G. 1984, *Astrophys. J.*, **279**, 896.
Norris, J. *et al.* 1986, *Astrophys. J.*, **301**, 213.
Ohki, K. Takakura, T., Tsuneta, S., and Nitta, N. 1983, *Solar Phys.*, **86**, 301.
Orrall, F. Q. and Zirker, J. B. 1976, *Astrophys. J.*, **208**, 618.
Orwig, L. E. and Woodgate, B. E. 1986, *The Lower Atmosphere of Solar Flares*, Proc. NSO/SMM Symposium at Sacromento Peak), D. F. Neidig (ed.), p. 306.
Prince, T. A., Forrest, D. J., Chupp, E. L., Kanbach, G., and Share, G. H. 1983, *Proc. 18th Intern. Cosmic Ray Conf.*, Bangalore, 4, 79.
Ramaty, R. and Lingenfelter, R. E. 1982, *Ann. Rev. Nucl. Sci.*, **32**, 235.
Rieger, E. *et al.* 1983, *Proc. 18th Intern. Cosmic Ray Conf.*, Bangalore, 10, 338.
Riegler, G. R. *et al.* 1981, *Astrophys. J. Letters*, **246**, L13.
Share, G. H., Chupp, E. L., Forrest, D. J., and Rieger, E. 1983, *Positron-Electron Pairs in Astrophysics*, M. L. Burns, A. K. Harding, and R. Ramaty (eds), AIP, New York, p. 15.
Spicer, D. S. 1983, *Adv. Space Res.*, **2**, 135.
Sylwester, J., Lemen, J. R., and Mewe, R. 1984, *Nature*, **310**, 665.
Smith, D. F. and Harmony, D.W. 1982, *Astrophys. J.*, **252**, 800.
Tanaka, K., Watanabe, T., and Nitta, N. 1984, *Astrophys. J.*, **282**, 793.
Teegarden, B. J. and Cline, T. L. 1980, *Astrophys. J.*, **236**, L67.
Tsuneta, S. *et al.* 1984, *Astrophys. J.*, **280**, 887.
von Rosenvinge, T. T., Ramaty, R. and Reames, D. V. 1981, *Proc. 17th Intern. Cosmic Ray Conf.*, Paris, 3, 28.
Wang, H. T. and Ramaty, R. 1974, *Solar Physics*, **36**, 129.
Watson, M.G., Willingate, R., Grindlay, J. E., and Hertz, P. 1981, *Astrophys. J.*, **250**, 142.

Appendix - GRID Instrument

In this appendix we discuss several technical aspects of the GRID instrument. Considerable effort has gone into conceptual design studies for a hard x-ray and γ-ray Fourier-transform imager, principally under the auspices of the Pinhole/Occulter Facility Science Working Group and the Max '91 Science Study Group. (For further discussions see, e.g., Tandberg-Hanssen et al., 1983 and 1986, Crannell et al., 1986, and the Report of the MAX'91 Science Study Committee, 1986). The baseline design presented in the main body of this proposal (section III) is essentially that developed by the Max '91 Science Study Group. We will not attempt a complete description of the GRID design, rather in this appendix we will focus on relevant new developments from recent design and hardware studies.

Section A.1 gives an overview of the current GRID baseline design and describes various design options. Section A.2 describes recent progress on fabricating very fine subcollimator grids suitable for γ-ray imaging. Section A.3 describes a recently completed laboratory demonstration of Fourier-transform techniques at γ-ray energies. Finally, section A.4 describes studies undertaken on the GRID instrument structure and aspect/alignment sensors.

A.1 GRID Configuration and Design Options

Because the GRID instrument is inherently modular, there is considerable flexibility in its design parameters. The baseline design described in the main body of the proposal has been used as a reference for stimulating and focusing the various technical studies that are underway. The completion of these technical studies is one aspect of the proposed Explorer Concept Study.

The baseline GRID design has been driven by the desire to optimize the performance of the instrument for solar flare observations. In spite of this, the GRID instrument will be very well suited for many studies of interest to cosmic high-energy astronomy because GRID brings entirely new observational capabilities to this field.

Imaging Design Considerations. The operating principle of GRID is based on the concept of Fourier-transform imaging. A Fourier transform x-ray telescope is composed of a number of subcollimators, each consisting of a pair of widely spaced collimator grids. Each collimator grid consists of parallel slits with a certain orientation and slit spacing. The characteristic large scale modulation (Moire) pattern at the detector plane arises from a small difference in slit spacing and orientation between the top and bottom grids. Each subcollimator is equivalent to a single baseline in radio interferometry in that each measures a single Fourier component of the source distribution (Makishima et al., 1977; Hurford and Hudson, 1979). This equivalence provides the key to evaluating the properties of a Fourier transform x-ray telescope for it implies that many of the analysis tools and considerations, highly developed for applications to such facilities as the Very Large Array, can be carried over directly into the x-ray domain.

In considering the design of a hard x-ray imager, scientific and operational factors strongly suggest that a whole-Sun field of view is desirable. The resolution of each subcollimator (defined as the FWHM angular response of the finest subcollimator or equivalently as one-half of the equivalent interferometer fringe spacing) is set by the ratio of the aperture size to grid separation. For example, a grid aperture of 50 μm and a 6.7 m boom length corresponds to 1.5 arc second resolution. The choice of the number of subcollimators (34 in the MAX'91 baseline design) necessarily involves a tradeoff. Clearly more subcollimators are desirable to provide better spatial information. However within a given instrument envelope, the advantages of a larger number of subcollimators must be weighed against the loss of sensitivity associated with smaller subcollimators, and against increased complexity in detectors, electronics, and data handling.

The selection of spatial frequencies ("u-v plane coverage") is also an important issue. Existing data from Hinotori and SMM indicate that from flare to flare sources can range from below ~5 arc seconds to several arc minutes in size. Imaging over such a wide range of size scales can be achieved by logarithmic spacing of spatial frequencies. Simulation studies have further indicated that with this choice, and with pseudo-random orientations of the spatial frequencies, significant reduction in image sidelobes can be achieved. (It might be noted that for x-ray Fourier transform telescopes the choice of spatial frequencies is independent for each subcollimator, a degree of freedom not available in the practical design of radio interferometers.)

With a few dozen subcollimators it is clear that complete full-Sun images with 1.5 arc second resolution will not be achieved in the sense of an optical image. Instead, a better analog might be the "snapshot" flare images obtained at radio frequencies with a 9 or 10 antenna VLA configuration (e.g., Marsh and Hurford, 1980). Simulation studies have confirmed that a GRID instrument with 34 subcollimators selected according to the foregoing arguments, and whose data is reduced using existing VLA mapping and cleaning software can readily meet the basic scientific requirements as outlined in the proposal. An example of one of these simulations is shown in Figure A.1-1. It should be noted that GRID will provide spatial information over a decade of energy of the solar spectrum that has never been imaged at all. Thus, the imaging capabilities of GRID represent a substantial initial step, particularly when it is appreciated that relatively simple source geometries are expected in the hard x-ray and γ-ray energy regimes.

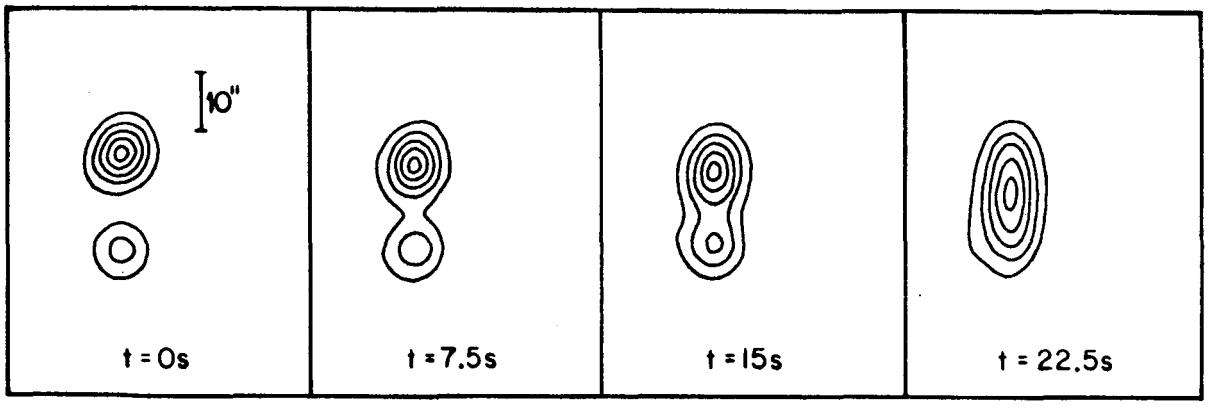

Figure A.1-1: Simulation of GRID imaging of a flaring magnetic loop viewed from above in x-rays greater than 25 keV. The x-ray source, initially isolated at footpoints of 3 and 5 arc second size, gradually fills the 16 arc second loop. Each image represents a 200 millisecond integration interval, shorter than the electron travel time, and therefore adequate to resolve the dynamic evolution of the source. The strength of the flare corresponds to that expected approximately once per month during a solar maximum period.

The range of capabilities of GRID is shown in Figure A.1-2. The three diagonal lines indicate the maximum energy for which spatial information can be obtained in each of three cases: (1) relatively weak fluences, for which there is a clear detection of the flare in every subcollimator at the maximum energy, but for which statistical fluctuations are still important; in this case, size scales and locations of a moderate number of the principal emission regions can be determined, (2) moderate strength fluences, for which the statistics are good enough that the phase and amplitude are well-determined in every subcollimator; in this case high-contrast can be obtained between relatively weak and relatively strong spatial features, (3) large fluences, for which there are adequate statistics to divide the data set into numerous time intervals, each with good phase and amplitude

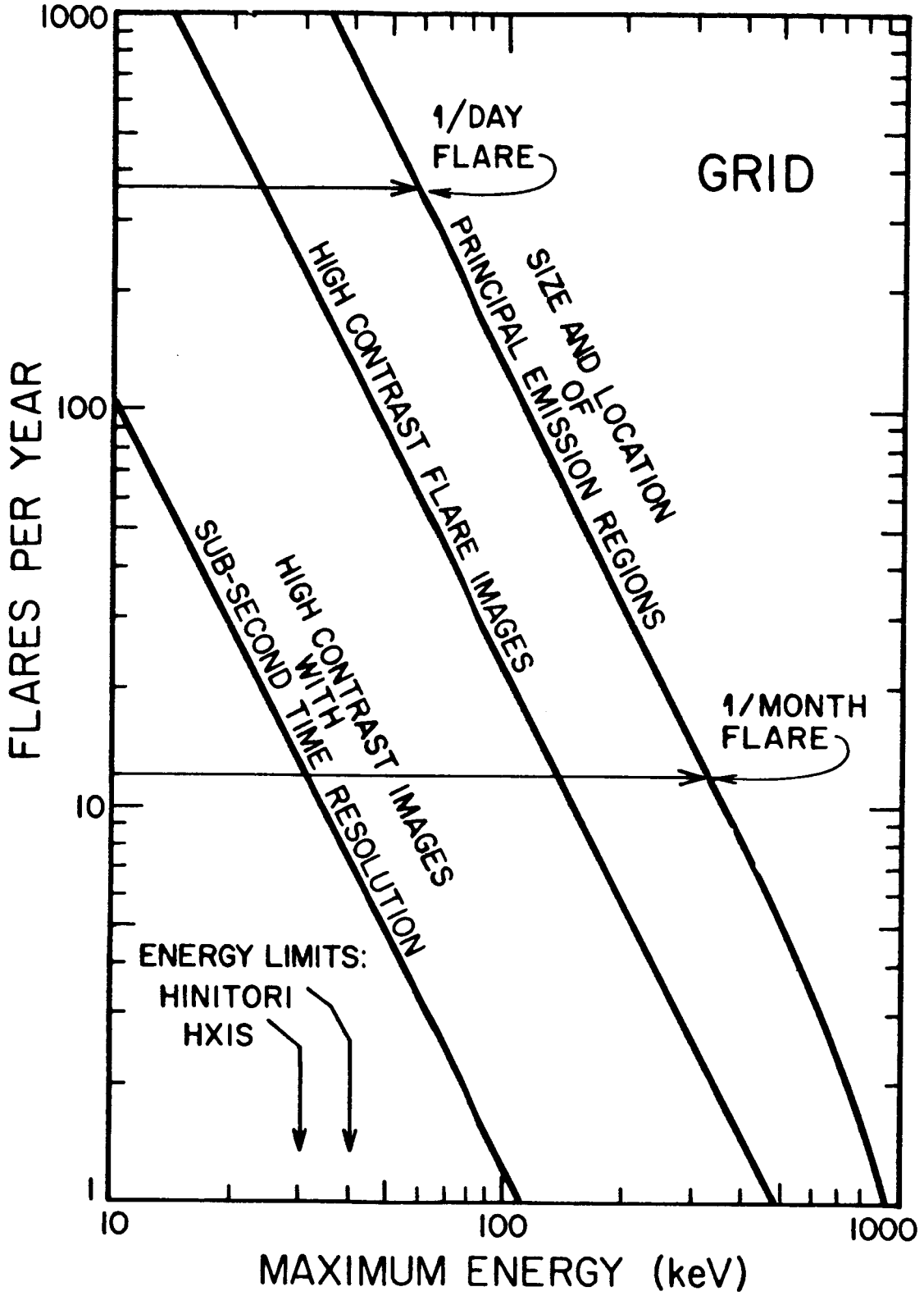
1000
100
10
1
FLARES PER YEAR
1/DAY
FLARE
GRID
SIZE AND LOCATION
OF
PRINCIPAL EMISSION REGIONS
HIGH CONTRAST FLARE IMAGES
1/MONTH
FLARE
HIGH CONTRAST
WITH
SUB-SECOND TIME RESOLUTION
IMAGES
ENERGY LIMITS:
HINITORI
HXIS
10
100
1000
MAXIMUM ENERGY (keV)

Figure A.1-2

information in every subcollimator; in this case, high-contrast spatial information can be obtained with sub-second time resolution allowing detailed studies of flare dynamics. The estimates in Figure A.1-2 have been obtained using actual SMM-HXRBS data from a typical period during 1982 and adjusting for the relative sensitivities of a GRID subcollimator and the HXRBS detector.

During the Phase A study, we will build on the radio-analog foundation to fully optimize the parameters of the GRID experiment. Software tools will be developed to systematically evaluate the imaging properties of the system as a function of source geometry, statistics, systematic error sources, and subcollimator number, size, and orientation. In addition, several design options will be studied with a view towards improved image quality at low energies where more complex image morphology might be expected. Such options include:

1) Imaging of long-lived x-ray sources to be achieved by slowly rotating or stepping the spacecraft about the earth-Sun axis. This would improve image quality in close analogy to the way that earth-rotation synthesis enhances the imaging ability of radio interferometers.

2) Allocation of part of the instrument frontal area for use by grids separated by a shorter effective boom length. Such grids, divided into smaller, more numerous subcollimators, would provide additional u-v coverage at low energies.

3) The superposition of thin grids onto the existing thick-grid planes. This would exploit the higher resolution and the two-dimensional response of the proportional-counters so that each subcollimator could measure several Fourier components simultaneously at low energies. (The thin grids would not affect the high-energy response.)

Such options more fully exploit the copious photon statistics and proportional counter performance at low energies without compromising the high-energy performance.

In summary, simulations and studies of Fourier transform x-ray imaging show that a GRID experiment on SHAPE can provide spatial information that comfortably satisfies the basic scientific objectives discussed in this proposal. The Phase A study will enable the design of the instrument to be optimized, with full consideration given to the unique aspects of its x-ray response and to the potential impact of low energy enhancements.

Baseline Design. Having discussed the basic imaging design considerations, we now describe the "baseline" design of the GRID instrument. This design, shown in Figure 1 of the proposal, is that previously studied by the MAX'91 Science Study Group. It consists of the following elements:

- 34 pairs of Fourier-transform grids (subcollimators),
- 34 modular x-ray detectors,
- 34 modular NaI(Tl) γ-ray detectors, and
- 2 aspect determination sensors.

The two planes of Fourier-transform grids are separated by 6.7 m. The grids of the upper plane are nominally 15 cm x 15 cm, while those of the lower plane are 10 cm x 10 cm. The slit widths increase logarithmically from 50 μm to 0.6 cm corresponding to angular resolutions of 1.5 arc second to 3 arc minutes respectively with a variety of angular orientations. The nominal thickness of the grids is 1 cm of tungsten to provide attenuation adequate for imaging of γ rays up to 1 MeV. In addition to the grids, lead honey-comb collimators are used above the detectors to reduce the diffuse background by restricting the field of view to approximately $\pm$ 2.5 degrees.

The x-ray detector system consists of 34 modular xenon multiwire proportional counters. Space qualified Xe counters have been developed for use on Spacelab by members of the SHAPE study team (e.g., U. of Birmingham). The GRID proportional counters will cover the energy range from 5 to 30 keV with good sensitivity and have moderate sensitivity up to 60 keV providing overlap and intercalibration with the γ-ray

detector system. An important consideration is saturation of the proportional counters in the very high fluxes of large solar flares. This problem will be alleviated by the use of variable thickness entrance windows which will be designed so that the detectors will have less effective area at low energies where the flux of x-rays is highest.

The γ-ray detector system will consist of 34 modular NaI(Tl) scintillation cameras with one-dimensional position resolution. The technology for NaI scintillation cameras has been developed extensively for γ-ray observations from balloon instruments. The nominal thickness of the NaI detectors is 2.5 cm giving good conversion efficiency, with 1.5 cm FWHM spatial resolution over the entire energy range, and with an energy resolution of 12% FWHM at 100 keV and 7% FWHM at 1 MeV.

The aspect sensors will either be optical pinhole imagers or solar disk sextants. Both of these systems determine the position of the limb of the Sun with respect to the grid planes in order to determine alignment and pointing direction. A further discussion is given in Appendix A.5.

By binning the events according to detector position and energy, considerable compaction of data and reduction of telemetry rate can be realized. Approaches have been developed which allow commandable adjustment of the binning specifications in order to optimize energy and time resolutions for specific scientific objectives.

Detector Plane Design Options. The use of NaI(Tl) scintillation cameras in the baseline design requires approximately 6 photomultiplier tubes (PMT's) per subcollimator and on-board computation of the photon interaction position. By introducing small differences in the orientation as well as the spacing of the top and bottom grids, the direction of the coarse spatial modulation in the detector plane can be adjusted to lie in one of two perpendicular directions for all of the subcollimators. The implications of this development include possible substantial simplification of the detector geometry. For instance, in the baseline design, it has allowed us to use one-dimensional instead of two-dimensional NaI scintillation cameras. We have recently been investigating an alternative design which uses discrete NaI bars and one-dimensional multiwire proportional chambers (MWPC's) to detect photons. In this configuration, the γ-ray detector for each subcollimator would consist of five Na(Tl) bars, nominally 2.5 cm x 2.5 cm x 10.0 cm. An additional bar would separate individual subcollimators. The dependence of the position of the solar shadow on flare position has been addressed by arranging that 1 1/4 periods of the modulation pattern corresponds to 5 NaI bars. This ensures that at least 1 full period of the subcollimator is illuminated regardless of the flare location. The MWPC's would be 10 cm wide, with their length an integral multiple of subcollimators.

By using NaI bars, detector plane position binning is automatic, simplifying the on-board processing electronics. In addition, the implementation of shielding is straightforward since the shield can be placed directly underneath the NaI bars. In the case of the baseline design, shielding must either be placed outside of the NaI camera PMT's, or a phoswich arrangement must be used in the camera itself, adding complexity to the electronics.

Two possibilities exist for the readout of the NaI bars. A single 2.5 cm diameter PMT could view each bar. Alternatively, with proper light guides, one large PMT could be used to view all six bars simultaneously, while in addition, each bar is viewed by one avalanche photodiode (APD). The single PMT provides an energy measurement while the APD's tag which bar contained the actual interaction. This latter scheme would have the advantage of significantly reducing the number of photomultiplier tubes needed in the detector plane array.

We will study the detector plane configuration tradeoffs as part of the proposed Phase A study.

A.2 Subcollimator Grid Fabrication

A new aspect of the GRID instrument is the fabrication of the Fourier-transform subcollimator grids. These grids determine the resolving power of the instrument and consequently their quality is crucial. To obtain 1.5 arc second resolution with a 7 meter boom requires the finest grids to have a slit width of 50 μm at a pitch (center to center distance of the slits) of nominally 100 μm. In order to attain the required attenuation of γ rays, a thickness equivalent to 5-10 mm of tungsten is required. Thus the most stringent requirement is set by the finest grids of the upper grid plane which are nominally 15 cm x 15 cm with slit widths of 50 μm and thickness of 5-10 mm.

Three approaches have been identified for fabrication of the required set of grids.

(1) Electrical discharge (ELOX) machining of tungsten material.

(2) Vertical stacking of tungsten sheets with the slit pattern photoetched into the material.

(3) Horizontal stacking of tungsten or tantalum slats with spacers providing the required slit width.

Schematic illustrations of the three methods are shown in Figure A.2-1.

Method (1) is probably the method of choice for fabrication of the coarser grids. Method (2) is an adaptation of methods used for construction of x-ray and hard x-ray collimators. It is definitely applicable to medium scale grids, and may be adaptable for fabricating even the finest scale grids. Method (3) may be the optimum method for constructing the finest scale grids. We include here description of work in progress at two of the member study institutions on fabrication of grids.

ELOX Machining and Stacked Tantalum Slat Techniques. As an initial attempt at grid fabrication, a group at the Goddard Space Flight Center led by Dr. C. J. Crannell has designed, fabricated, and tested a fine pair and a coarse pair of collimator grids. The coarse collimator was used to verify that standard ELOX machine-shop techniques were applicable and to also provide a unit whose collimator response was easily tested using optical techniques. A pair of coarse (6 mm) collimator grids was machined to specifications from a solid block of tungsten; no outstanding problems were encountered. The ELOX method is now being studied to determine the smallest slit sizes that can be easily fabricated.

The fine collimator size (100 μm) was chosen because it places stringent requirements on design, fabrication, and testing techniques. The particular size is within a factor of 2 of the desired resolution (1.5 arc second with a 6.7 m boom). Fabrication of the initial pair of fine collimator grids has been completed and the units have undergone preliminary performance tests. The fabrication approach was simply to compress alternate 0.5-cm-wide x 10-cm-long pieces of 100 μm thick tantalum and 100 μm thick mylar together inside a rigid steel frame using screw-adjustable pressure plates. A photograph of one of the completed units is shown in Figure A.2-2. The grids have 500 such tantalum/mylar slat pairs contained within the 10-cm collimator length.

The presence of mylar material, rather than voids between the tantalum slats, is not ideal because of the attenuation of photons at low energy ($\leq$ 20 keV). However, this initial fabrication attempt is of interest in testing whether simple stacking techniques can produce a grid in which the precise position and alignment of each tantalum slat in the grid can be held to within the tight design tolerance required by the Fourier-transform technique. Precise measurements of the slat positions, dimensions and alignment have been carried out using a Grant Instruments Series 800 Comparator-Microphotometer system at GSFC. The deviations from the expected positions were found to be less than about 30 μm, consistent with the random walk fluctuations one would expect in a stack consisting of 500 slat-spacer pairs having an RMS deviation in thickness per pair of

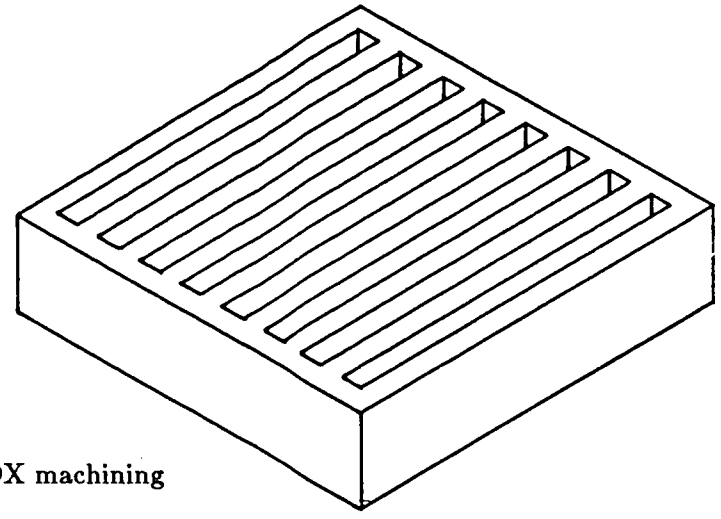

ELOX machining

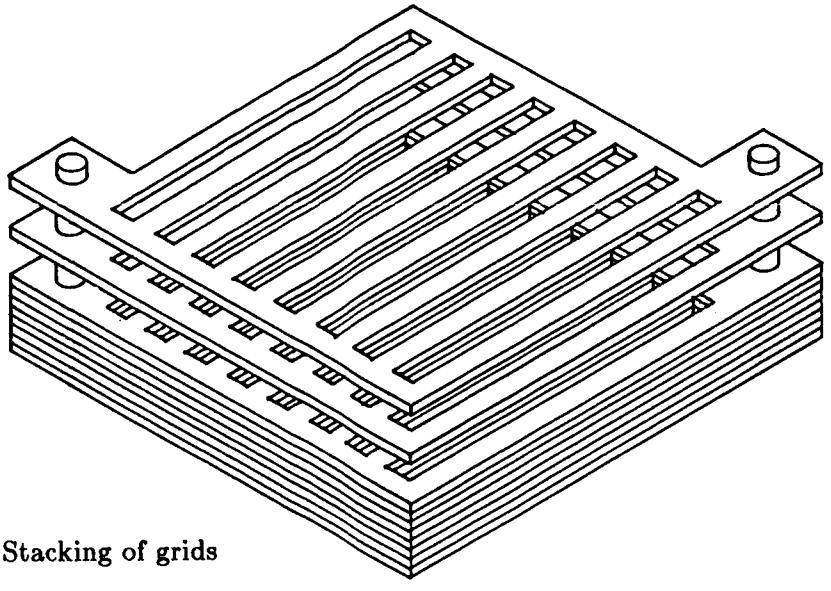

Stacking of grids

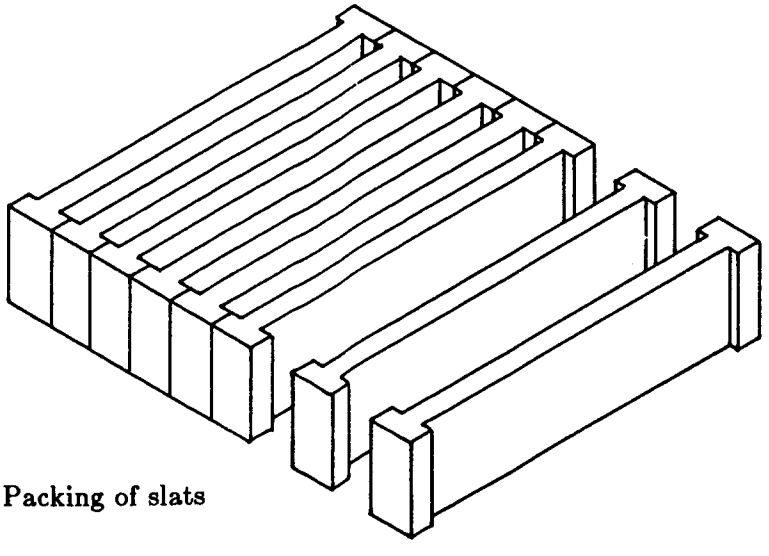

Packing of slats

Figure A.2-1

100-MICRON GRID

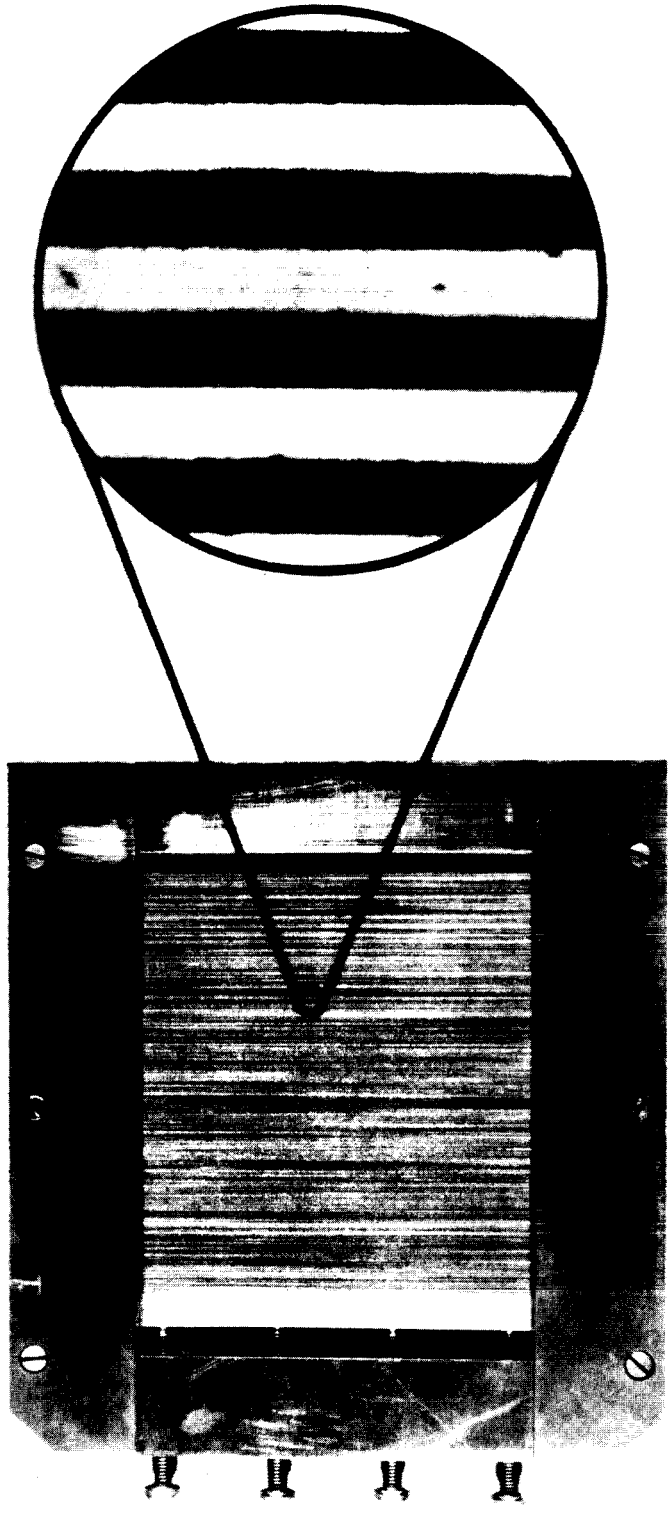

Figure A.2-2

~3 μm. Improved material tolerance and registration of, for instance, every 20th or 50th slat pair should reduce the non-uniformities to acceptable levels.

Horizontally Stacked Photoetched Tungsten Slats. Another approach to the stacking of slats is being developed at the Delft University of Technology. In the Netherlands, tungsten grids were developed and successfully applied for the HXIS instrument on board the NASA Solar Maximum Mission. The HXIS grids were made of basic material with a thickness of 50 μm. Because of this experience, the Laboratory for Micro-Engineering at the Delft University of Technology has started development on the grids required for the GRID instrument. Prof. H. F. van Beek, formerly at Utrecht and now at Delft, leads this development.

The approach for achieving the required slit pattern starts with slats of material, 5 mm wide, 60 mm long, and 100 μm thick. Fabrication of longer slats will be attempted at a later date. By means of chemical etching, the slats can be reduced in thickness to the required 50 μm by removing 25 μm at each side. This etching is done selectively so that spacers will remain that later will keep the slits open and parallel. Figure A.2-3 shows a schematic of one of the etched slats. It is crucial that the pitch of the slits in the upper grid plane deviate very little and in a well defined manner from the pitch of the slits in the lower grid plane.

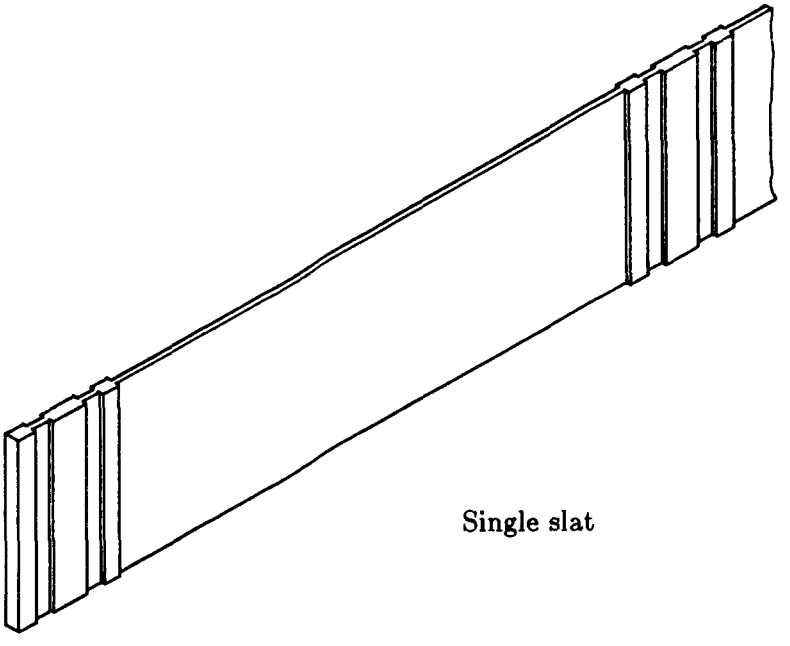

Figure A.2-3

The technique as set up by the Delft group enables the development of the fine grids in a step-by-step mode. The etching technique as well as the pitch adjustment and slat packaging technique can be learned on small samples that cover a few cm^2. Gradually, larger areas of grids can be prepared until full size grids covering hundreds of cm^2 can be manufactured. The development can be split into a purely mechanical part and an etching part. The current status is that a few samples have been manufactured using spring steel instead of tungsten in order to start the mechanical part of the development. As of October, 1986, tungsten etching will be undertaken so that next year the first samples in tungsten can be prepared.

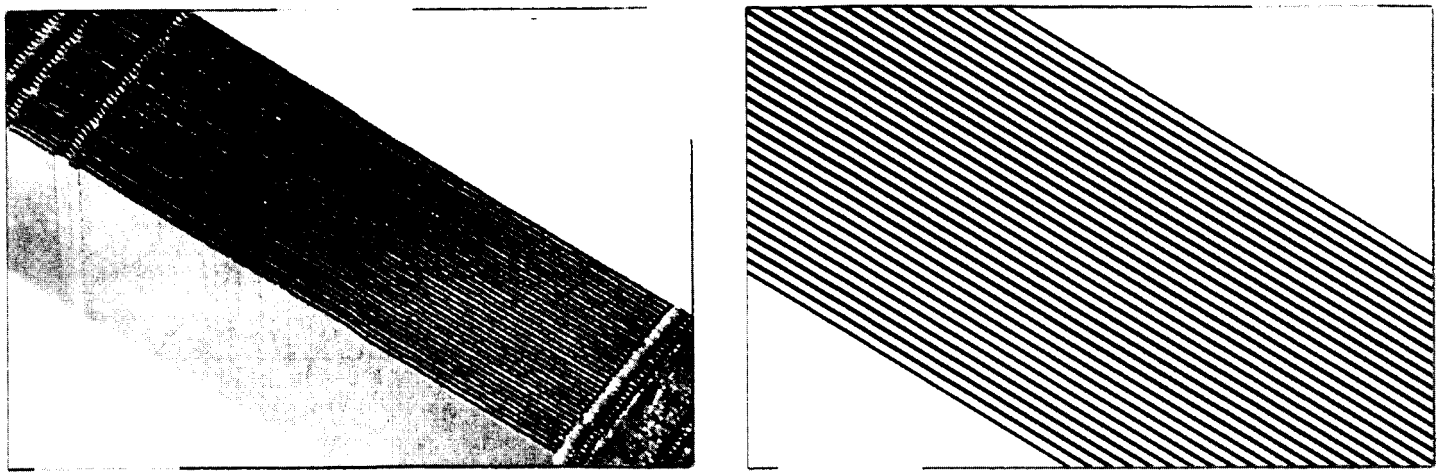

Figure A.2-4a & b

Figure A.2-4a&b shows actual photographs of one of the first samples in spring steel. The package is made out of 35 slats of 100 μm thickness each so that it covers an area of 60 mm x 3.5 mm. The left part of the figure shows how the package is composed out of the individual adjacent slats such as the one shown schematically in Figure A.2-3. The right part shows the slits while white light is scattering through them. Because of this scattering, the open slits seem wider than they are in reality. The accuracy of slit width and slit straightness is close to that acceptable for flight. Given the current results, obtained in such a short time of development, further improvements can be expected. Because of the suitable mechanical characteristics of tungsten and because of the good prospects for etching this material, no special problems are foreseen in switching from spring steel to tungsten.

During the Phase A study, the various approaches and methods discussed here will be evaluated to determine the optimal fabrication technique for the various ranges of grid slit sizes.

A.3 Demonstration of Fourier Transform Imaging

A practical implementation of Fourier-transform imaging techniques for high-energy photons requires a laboratory feasibility demonstration and study of imaging systematics. Such a study was undertaken at Caltech during the past year. The laboratory apparatus consisted of a set of seven subcollimator grid pairs viewed by a standard NaI scintillation camera similar to instrumentation developed for balloon payloads. The subcollimators were oriented in a single direction so that one-dimensional images are readily constructed. Two-dimensional images could also be made by simple rotation of the grid structure through discrete angular orientations. The laboratory arrangement is shown in Figure A.3-1.

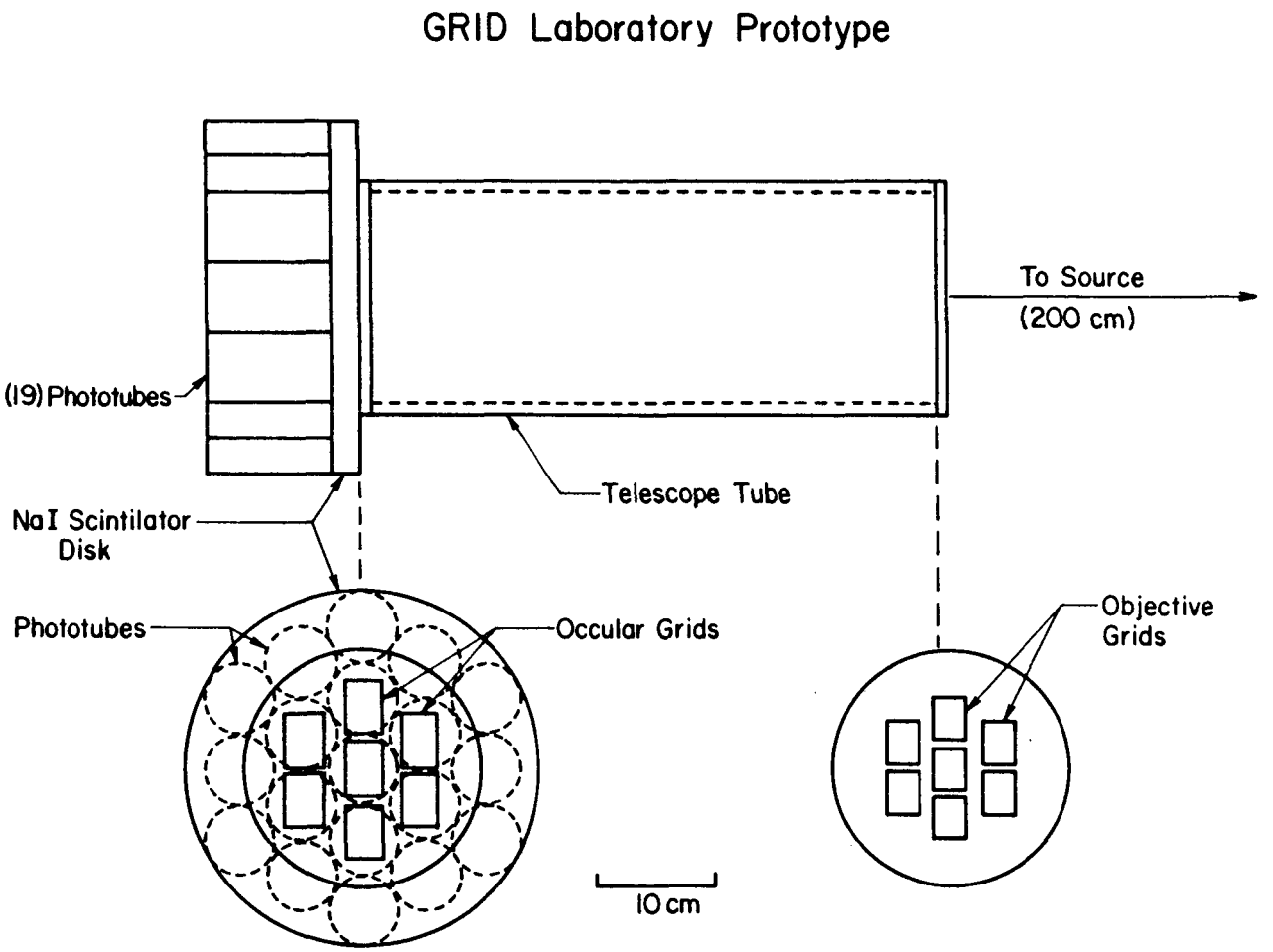

Figure A.3-1

We have recently obtained one-dimensional images at 122 keV. Figure A.3-2a shows distributions of events versus position as measured by the NaI camera from a single subcollimator due to a single source positioned 2 m away. Figure A.3-2b shows data from the same subcollimator but now from a source displaced slightly in position (by 6 mm). The basic response in the two plots consists of a uniform background component together with a triangular response with peak positions corresponding to different source positions. From the event count distribution, the phase and amplitude of one of the Fourier components of the source can be determined. In a similar fashion, Fourier phases and amplitudes can be determined from each of the seven grid pairs.

Figure A.3-3 shows the "uncleaned" image resulting from the superposition of the seven Fourier components. Using standard radio interferometry "cleaning" techniques, the side-lobe distribution present in Figure A.3-3 can be largely eliminated. Figure A.3-4 shows the "clean" distribution resulting from application of one of the standard image processing algorithms. The two sources are clearly visible. Note the distance scale which indicates a very fine source resolution capability. In fact, the position of a single γ-ray source can be determined to better than 100 μm accuracy, and two sources that are ~ 3 mm apart should be easily resolvable.

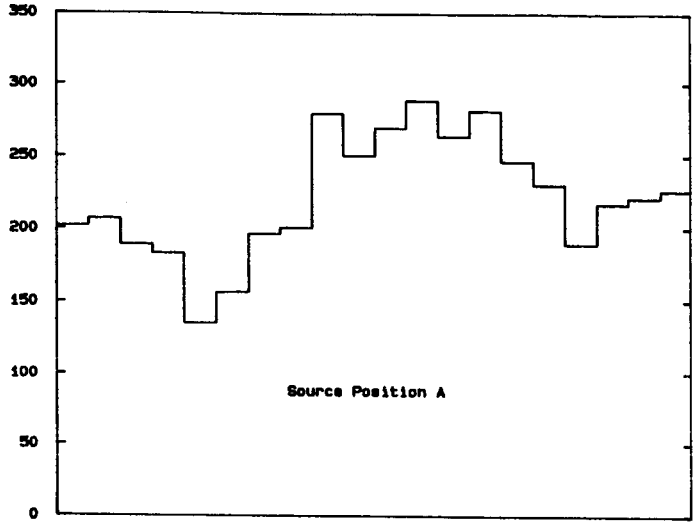

Figure A.3-2a

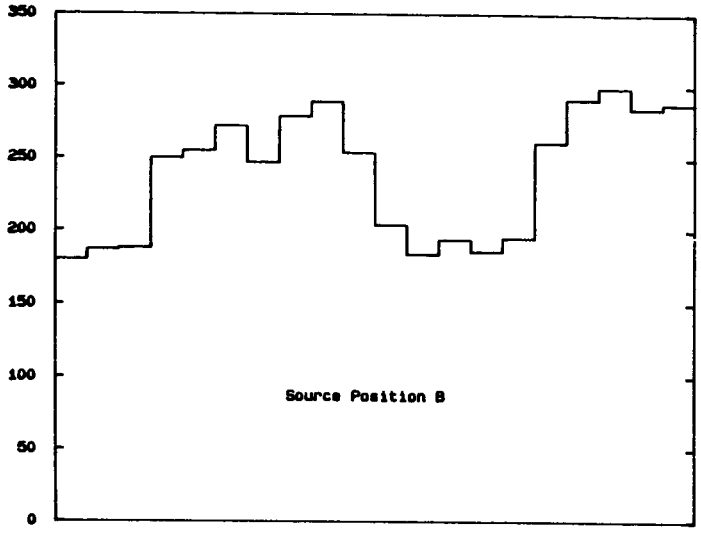

Figure A.3-2b

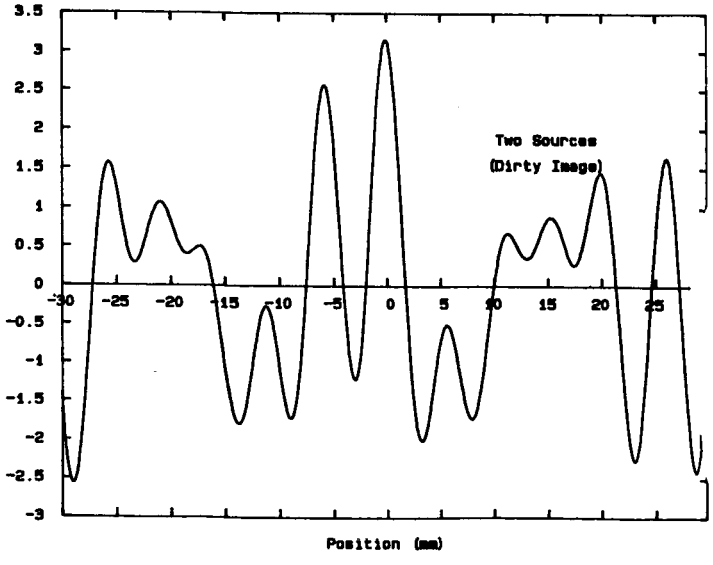

Figure A.3-3

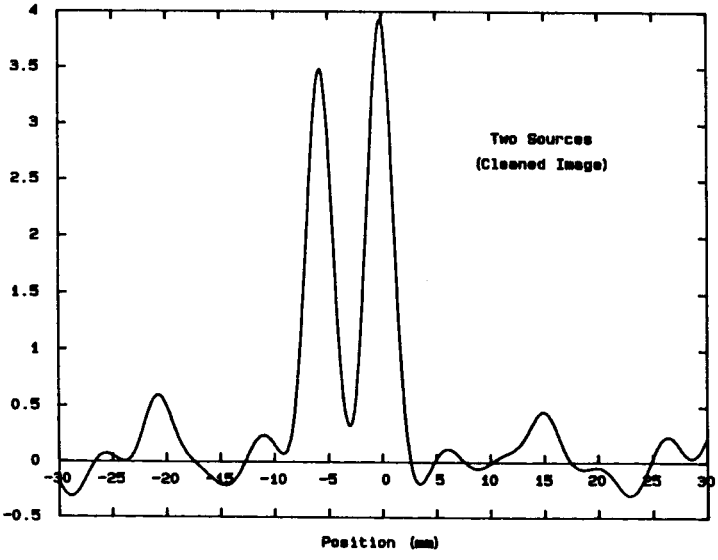

Figure A.3-4

We have begun to make two dimensional images using this apparatus. Figure A.3-5 shows an image of a single 122 keV source produced by the seven collimators rotated to twelve different orientations. The scale of this image is 8 cm on a side, with graph lines every millimeter. Figure A.3-6 shows the same image after "cleaning".

These laboratory studies demonstrate the feasibility of implementing Fourier-transform techniques in the γ-ray regime.

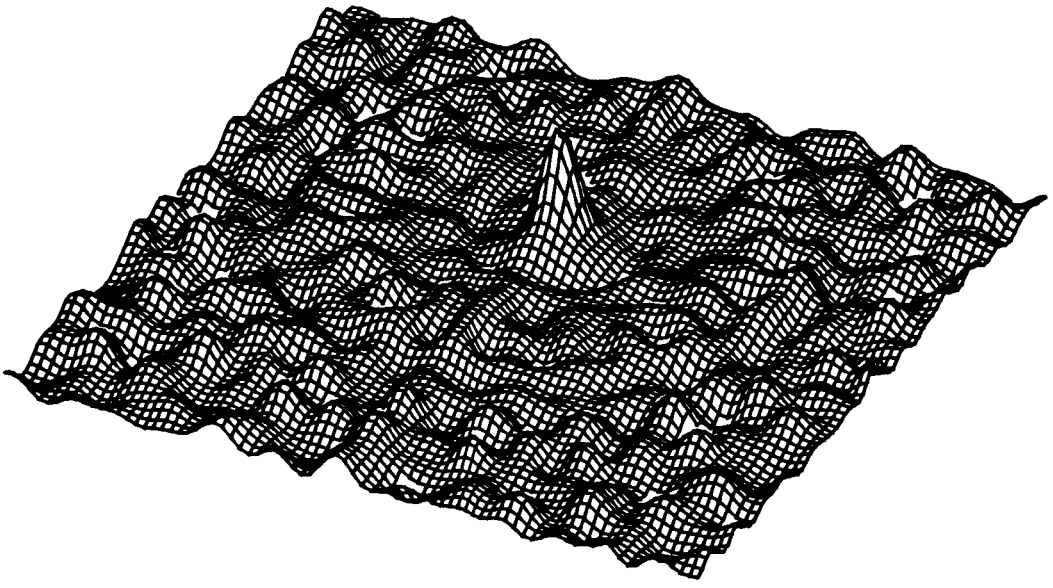

Figure A.3-5

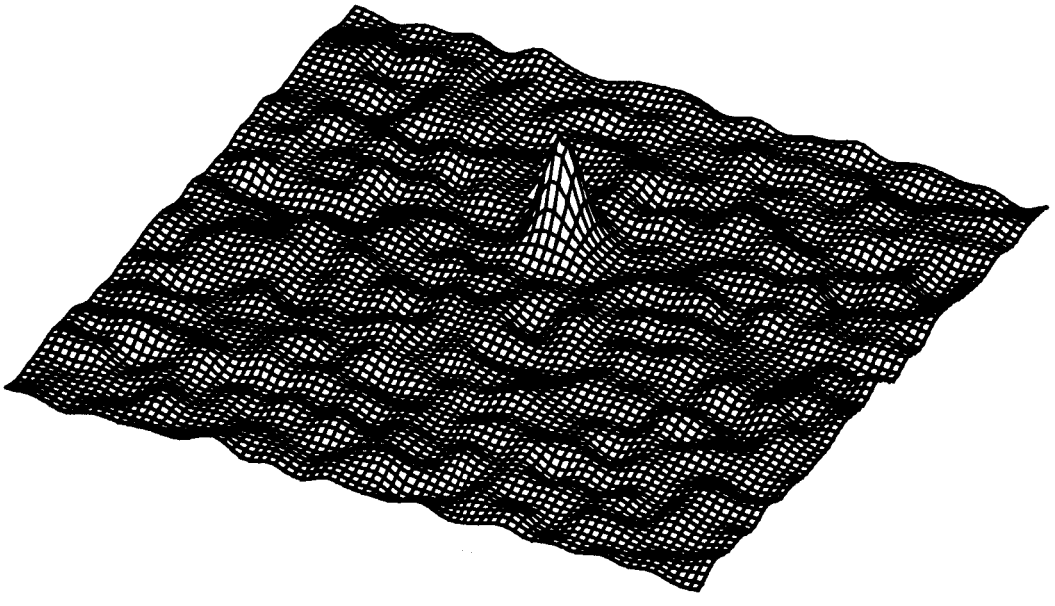

Figure A.3-6

A.4 Structural Design and Alignment/Aspect Determination

The requirements for alignment and aspect of the grid planes in given in Table A.4-1.

Table A.4-1

VECTOR	PLACEMENT (MAXIMUM)	STABILITY (RMS)	POST-FACTO KNOWLEDGE (RMS)
$\hat{p}$	3 arc min	1 arc sec/30 sec	0.2 arc sec
$\hat{d}\cdot\hat{p}$	20 arc min	10 arc min	10 arc min
$\delta\hat{r}$	10 arc sec	10 arc sec	2 arc sec
$\hat{r}_d$	1 degree	3 arc min/30 sec	1.5 arc min
$\hat{d}\cdot\hat{m}$	20 arc min	10 arc min	10 arc min

$\hat{p}$: Pointing direction - through centers of mask and detector planes
$\hat{d}\cdot\hat{p}$: Angle between perpendicular to detector plane and pointing direction (absolute tilt)
$\delta\hat{r}$: Relative azimuthal orientations of detector and mask planes (relative twist)
$\hat{r}_d$: Absolute azimuthal orientation of detector plane (absolute twist)
$\hat{d}\cdot\hat{m}$: angle between perpendiculars to mask and detector planes (relative tilt)

Design of a Boom for GRID. A preliminary concept and design of a boom for the GRID instrument has been studied. The studies have shown that the construction of a lightweight boom suitable for the GRID experiment presents no significant technical problems and in fact can have attractive features such as being deployable/retractable. The boom, proposed by United Technologies, was designed so that it can be retracted into a compact package for transportation in the STS orbiter and so that it provides a stable mounting for the mask assemblies when deployed in orbit. The overall structure as seen in Figure A.4-1 includes a fixed section which mounts the boom and other experiment assemblies to the Payload Support Structure. The deployable section, with graphite-epoxy members, utilizes a Tri-fold square truss design to provide a compaction ratio of 17.5:1 while forming a thermally and dynamically stable structure. A base-mounted deployment structure is not required. The design described herein is based on presently available preliminary requirements and is representative of currently achievable structural technology.

Preliminary Requirements

Overall length deployed	7.1 m
Deployable length retracted	.35 m
Boom cross section	1.3 m
Torsional stability	$<$ 1.0 arc min
Thermal stability, CTE per bay	$\pm$ 5 x 10^{-6} in/in $^{\circ}F^{-1}$
Loading, root accel.	8.59 deg./sec^2
Safety factor	2.0
End mass	68 kg

Figure A.4-1 shows the payload configuration on a spacelab pallet with the GRID boom shown deployed. With the boom retracted, there is no overhang beyond the pallet envelope. The boom is secured in the retracted position with latches. When ready for deployment the latches are released and the three-bay truss is deployed. Deployment is accomplished by the use of torsion springs and control cables, with automatic spring latching. All mechanisms have back-up redundancy. Boom retraction, after a 3 year mission life, is accomplished by retraction cables with redundant reel drives. An alternate deployment/retraction design concept uses motor drives at three of the longeron

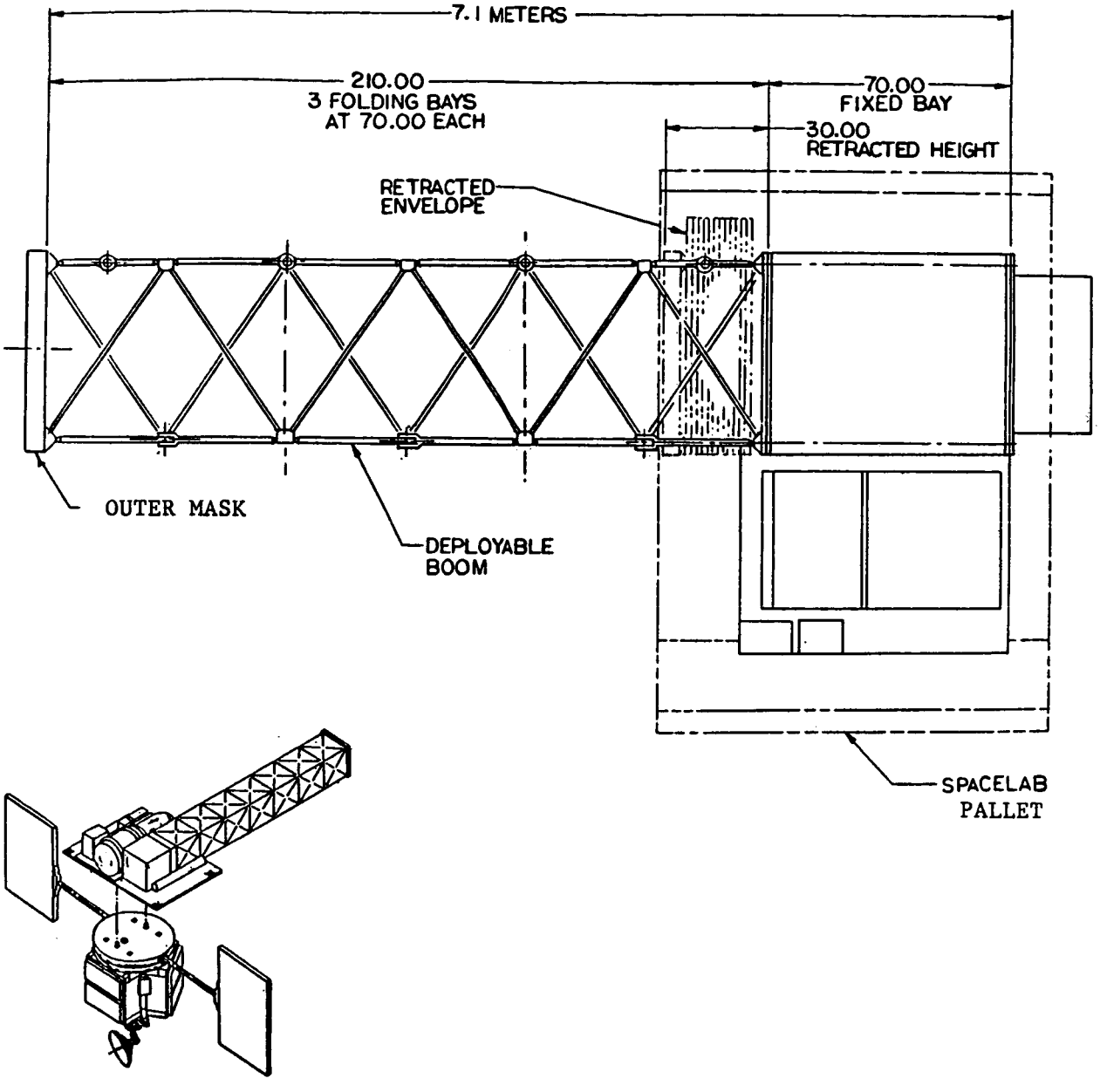
7.1 METERS
210.00
3 FOLDING BAYS
AT 70.00 EACH
70.00
FIXED BAY
30.00
RETRACTED HEIGHT
RETRACTED
ENVELOPE
OUTER MASK
DEPLOYABLE
BOOM
SPACELAB
PALLET

Figure A.4-1

hinge points. The drives would incorporate full redundancy.

The square Tri-Fold truss normally incorporates internal diagonals to provide for localized transverse stiffness. For torsional and cantilever stiffness and strength, these members are not necessary and for this application have been removed. This provides a 100% clear view through the boom and simplifies the joints.

A finite element model of the boom was constructed and used extensively to evaluate static and dynamic characteristics and optimize structural parameters. The model has the following characteristics:

- Cantilever mount with 68 kg end mass
- Mass representation at joint nodes and hinges
- Realistic stiffness coefficients for joints & hinges, based on test data.
- Preloaded joints, no damping
- Materials - 30 x 10^6 modulus graphite epoxy tubes, titanium joints and hinges.

For the selected reference design, the first 10 vibrational modes have vibrational modes with frequencies between 6.36 and 9.15 Hz. The maximum torsional deflections (rotations) of the boom will probably be those due to angular accelerations during attitude control rather than from any dynamic excitation sources. The analyses indicate that the reference design, using the Tri-fold deployment geometry with the required folding joints, will provide a stable boom structure for the GRID experiment. Work is now in progress to determine optimum design parameters for the truss joints and deployment actuators. A thermal analysis of the structure is also planned.

Aspect/Alignment Determination. We are studying several approaches for determination of alignment and aspect. One option is to use a pinhole in the upper grid plane to cast an image of the Sun onto the lower grid plane. The position of the Sun image is then determined by optical sensors, for instance quadrant splitters. Another option, which determines alignment only, uses a system of two lasers and mirrors to determine the alignment of the upper grid plane with respect to the lower grid plane. A third option is to use an instrument currently being developed as a Hitchhiker and balloon payload called the Solar Disk Sextant (SDS). We discuss this third approach in more detail in the following paragraphs.

Both alignment and aspect sensing can be implemented by use of a modified version of the SDS, an instrument designed to obtain precise measurements of the solar diameter (Sofia et al., 1984). The operating principles of SDS are illustrated in Figure A.4-2. The primary optical element used to form multiple images of the Sun is a stable, partially transmitting beam-splitting wedge of precisely known angle. A long-focal-length telescope is used to image the first two of the series of solar images onto a set of linear arrays placed in the focal plane. As implemented for the SHAPE mission, the beam-splitting wedge will be combined with a refractive lens of focal length 6.8m. This combination mounted on the outer end of the boom will produce images at the base of the boom, where the linear array detectors are mounted in precise placement with respect to the inner grids.

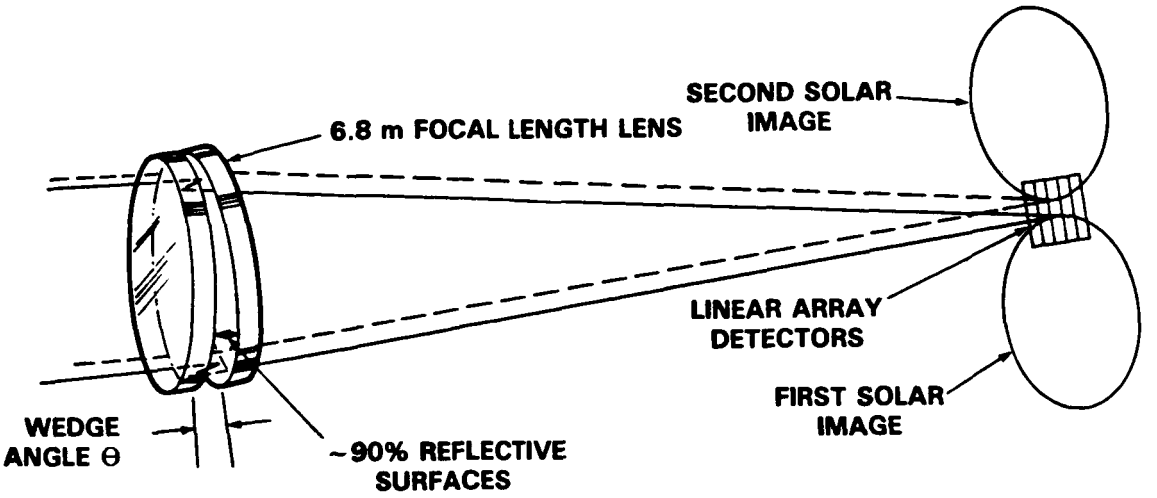

Figure A.4-2. Schematic showing the operating principles of SDS. Note that the wedge angle θ is set to approximately half the solar diameter or ~ 990 arc seconds.

Two SDSs will be required to establish the relative roll alignment of the inner and outer sets of grids to 1 arc second. The real-time system will determine the position of each of the solar edges viewed by the detectors. From the sets of edge positions, the location of the centers of the solar images will then be computed. The position in the image plane of the center of the first solar image can then be algebraically compared with the previously established desired position of the image center to provide the desired spacecraft fine-pointing error function. In addition to providing aspect information for GRID, the two SDSs will measure perpendicular solar diameters simultaneously and with sufficient precision to provide substantial scientific return in their own right. The SDS is thus especially attractive in the context of the SHAPE payload because it can fulfill the dual role of a basic science instrument and an experiment aspect sensing system.

By measuring solar size, shape, and variations, the SDS addresses questions relating to the physics of the solar interior. Variations in the solar size should be directly correlated with variations in the solar energy output. Combined with data from an ACRIM instrument, the SDS measurements would provide important clues to the physical origin of these variations and thus contribute to our basic understanding of solar luminosity. Measurements of the solar shape will provide accurate data on solar oblateness and quadrupole moment. These data bear directly on theories of solar evolution and interior dynamics. Additionally, variations in the solar shape reflect pulsations of the Sun, information of extreme current interest to the field of helioseismology. The SDS should be particularly effective for studying pulsations in the long period regime where standard Doppler techniques are least sensitive.

During the Phase A study, the SDS and alternative aspect and alignment sensing techniques will be evaluated on the basis of cost and performance. A recommendation will then be made on the technique most appropriate for the GRID instrument.

References
Appendix A

Crannell, C. J., Hurford, G. J., Orwig, L. E., and Prince, T. A. "A Fourier Transform Telescope for Sub-arcsecond Imaging of X-rays and Gamma rays," **Proc. of the SPIE, 571,** 142 (1986).

Hurford, G. J. and Hudson, H. S., "Fourier Transform Imaging for X-ray Astronomy", BBSO preprint 0188 (1980) and UCSD-SP - 79-27 (1979).

Makishima, K., Miyamato, S., Murakami, T., Nishimura, J., Oda, M., Ogawara, Y., and Tawara, Y., "Modulation Collimator as an Imaging Device," in van der Hucht, K. A. and Vaiana, G. (eds.), **New Instrumentation in Space Astronomy,** New York, Pergammon Press, 277 (1977).

Marsh, K. A. and Hurford, G. J., "Two-dimensional VLA Maps of Solar Bursts at 15 and 23 GHZ with Arcsecond Resolution," **Ap. J., 240,** L111 (1980).

"Report of the Max'91 Science Study Group," NASA (1986).

Sofia, S., Chiu, H., Maier, E., Schatten, K., Minott, P. and Endal, E., "Solar Disk Sextant," **Applied Optics, 23,** 1226 (1984).

Tandberg-Hanssen, E. A., Hudson, H. S., Dabbs, J. R., and Baity, W. A. (eds.), "The Pinhole/Occulter Facility," NASA Technical Paper 2168 (1983).

Tandberg-Hanssen, E., Wilson, R. M., and Hudson, H. S. (eds.), "Solar Flares and Coronal Physics Using P/OF as a Research Tool," NASA Conference Publication 2421 (1986).

APPENDIX B. HIGH RESOLUTION GAMMA RAY AND NEUTRON SPECTROMETER (HIGRANS)

INTRODUCTION

HIGRANS consists of an array of 12 dual segment, high-purity germanium (HPGe) detectors in a BGO scintillator annulus and back shield/detector assembly (see Figure 3 in main text). The detector system is enclosed in a plastic-scintillator charged-particle shield. The HPGe detectors are contained in a cryostat and cooled to an operating temperature of 90°K with a two-stage solid-cryogen (methane/ammonia) refrigerator via a cold finger.

HIGRANS is designed with a wide, 120° FWHM, field of view, and with excellent dynamic range and count rate capabilities, suitable for high spectral resolution (Figure B1) spectroscopy of solar flare and cosmic gamma-ray bursts, which last typically ~ 0.1–10^3 s. The segmentation of the HPGe detectors provides for a clean separation of the $<10^2$ keV hard X-ray region, where the intense solar flare fluxes are observed, from the >0.4 MeV gamma-ray line region. The HPGe detector electronics is designed to operate over a very wide energy range (10 keV–250 MeV) and to accommodate the range of counting rates expected from flare bursts while maintaining the high spectral resolution of the HPGe detectors. Pulse shape analysis techniques are used to provide low background in the 0.4–2 MeV gamma-ray line region. The BGO and plastic scintillator shield systems, together with the HPGe detectors, can separate and measure fluxes of high energy >20 MeV gamma-rays and neutrons.

HIGRANS is very similar to a balloon-borne twelve segmented HPGe instrument presently being developed for gamma-ray spectroscopy of cosmic sources. An engineering test balloon flight is planned for this fall with a single dual-segmented HPGe detector, in a thick CsI shield with a prototype BGO shield piece, and all flight electronics. The full 12 detector instrument with BGO shield is being fabricated for a balloon flight in late 1987-early 1988. Thus much of the development required for HIGRANS will be completed by the end of the Explorer study phase. We are therefore confident that HIGRANS will then be ready for hardware development and fabrication.

Detailed discussions of the performance of HIGRANS and its subsystems are contained in the following sections.

HIGH RESOLUTION HPGe DETECTOR SYSTEM

Segmented HPGe Detectors

The closed-end HPGe detectors are fabricated from n-type material, 6 cm in diameter and 6 cm thick, and are operated in the reverse bias mode, i.e., the holes are collected by the outside electrode (Figure B2), to minimize radiation damage from long term exposure to energetic particles in space. Based on accelerator tests, no detectable degradation is expected for this type of reverse bias detector in a several year space mission in low earth orbit (Pehl, 1978).

Each detector has multiple collecting electrodes which divide it into two distinct volumes, or segments, according to the electric field pattern (Figure B2). In the central 1.0-cm diameter hole which extends to within ~6 mm of the top, two separate contacts are provided by diffusing lithium into the germanium, coating the lithium with gold, then lapping away the gold and lithium in the boundary between the contacts. The detector is then re-etched to provide a clean surface in the boundary—the gold is unaffected by the etch. This segmenting technique was developed at UCB (Luke, 1984). The top contact collects charge from the upper 1-cm segment of the detector, and the long lower contact collects charge from the bottom ~5-cm coaxial segment. The curved outer surface and top surfaces are implanted with boron to make a very thin (~0.3 micron) window for X-rays, and metallized for the high voltage contact. The bottom flat surface of the detector is coated with amorphous germanium to eliminate surface channeling effects. A 4-cm dia.×4-cm thick prototype and three full size (5.5–6 cm dia.) dual segment detectors have already been fabricated at UCB for the

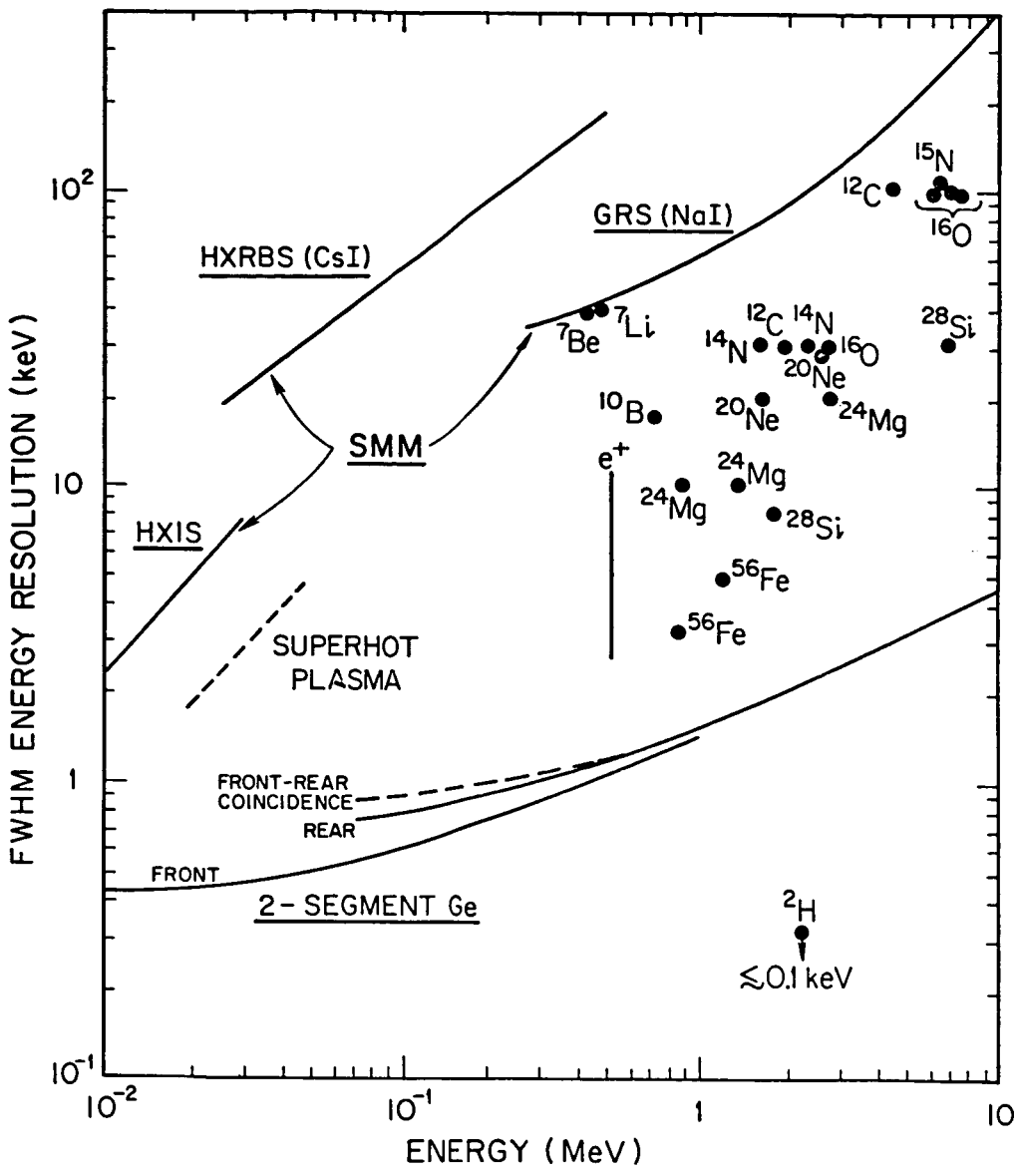

Figure B1. The spectral resolution of the HIGRANS 2-segment HPGe detectors is compared with that of the hard X-ray and gamma-ray instruments on SMM. The typical line widths expected for gamma-rays in solar flares are shown, as well as the resolution required to resolve the steep super-hot thermal component (dashed line).

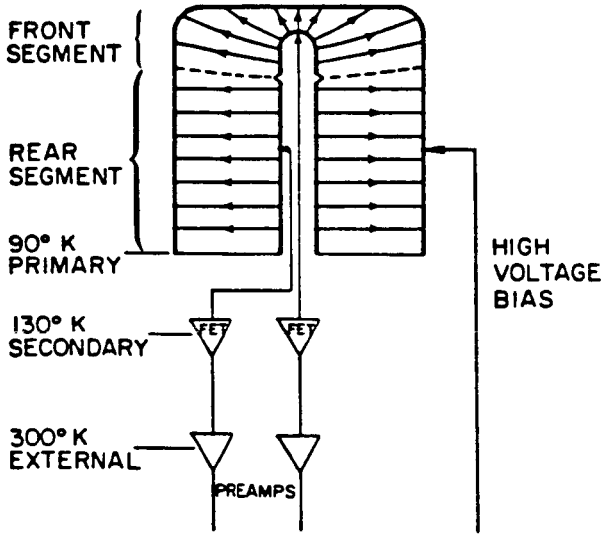

Figure B2. Schematic of a dual-segment HPGe detector.

balloon instrument.

The HPGe detectors operate in three spectroscopy modes. The top segment only is used at low energies ($\leq$150 keV) where photoelectric absorption dominates (Figure B3). Photons are absorbed in the top ~1-cm segment, while Compton scattered photons and detector background is rejected by anticoincidence with the adjacent bottom segment of the detector. Therefore, this mode has the excellent background rejection properties of a phoswich type scintillation counter (Matteson et al., 1977).

Higher energy ($\gtrsim$150 keV) photons are detected primarily in the thick bottom segment alone mode, with a smaller fraction also detected via top-bottom coincidences (Figure B3). The bottom segment is shielded by the top segment from low energy, $\lesssim 10^2$ keV protons. This shielding is crucial for detection of gamma-ray photons in large flares, where an intense hard X-ray burst occurs simultaneous with the gamma-ray emission. Even for the largest flares observed by SMM, the count rates in the bottom segment are easily accommodated by the HPGe electronics without spectral distortion or saturation. The segmentation is also important for background rejection, as discussed in a later section.

The very thin boron implanted outer surface of the HPGe detectors is mechanically fragile. At UCB/UCSD we have developed a special detector holder for the balloon instrument which provides good mechanical support. This holder has been tested successfully to Shuttle (STS) vibration levels. The holder also provides the dual inner contacts for the top and bottom segments, and is designed to plug into the cold plate in the cryostat.

Performance

Dynamic Range. Figure B4 shows the range of continuum fluxes for solar flares and cosmic gamma-ray bursts compared to the diffuse sky flux (computed for the HIGRANS (120° FWHM field of view) which dominates the hard X-ray background. The right hand scale shows the counts/keV for a single (~28 cm^2 area) HPGe detector assuming unit efficiency. The efficiency of the HIGRANS instrument, computed from Monte-Carlo simulations, is plotted in Figure B3 separately for the top and bottom segment of the HPGe detector. Even in the largest flares the peak count rates of the bottom segments is $\lesssim 2\times10^4$ c/s per detector, well within the capabilities of the electronics for distortion-free and low dead time operation.

The largest cosmic gamma-ray burst can be accommodated by both the HPGe top and bottom segments without compromise. The top segments, however, require attenuation to accommodate the fluxes of the largest flares. This attenuation is provided by various absorbers which are placed in front of the plastic shield ~30 cm from the HPGe detectors to block fluxes from the solar direction only (see Figure 3 of main text). These absorbers block less than 20% of the full 120° FWHM field of view, so cosmic gamma-ray bursts will generally be unaffected. Four HPGe detectors have no absorber (except the 1g/cm^2 plastic shield) for detection of microflares and small flares with maximum sensitivity, four are optimized for small to medium flares (with ~0.2g/cm^2 Al absorber), and the last four detectors are optimized for medium to the largest flares (~2g/cm^2 Cu with 0.1 cm^2 hole with 0.2g/cm^2 Al). The effect of these absorbers is shown in Figure B3.

Sensitivity. HIGRANS is designed primarily for spectroscopy of solar flare bursts (and cosmic gamma-ray bursts) which typically last ~10–10^2 s (~0.1–10^2 s). In such short intervals the number of detector background counts in the gamma-ray line region is small (Table B1), and during the flare impulsive phase the bremsstrahlung continuum from the flare will usually dominate the detector background. Table B1 shows that in a flare the size of the 27 April 1981 gamma-ray flare, several hundred to a couple thousand counts would be obtained by HIGRANS in each of a dozen major lines (including four lines of Fe) with line-to-continuum ratios of $l/c \approx 1$ to 10, except for the broad Li-Be combined lines where $l/c \approx 0.2$. These lines will be detected at ~10–60 σ's significance. Thus, line shapes, asymmetries, etc. can be accurately determined. Even for a flare with line fluences more than 30 times smaller, most of these lines could be detected at the 3σ level if the line/continuum ratio remained the same.

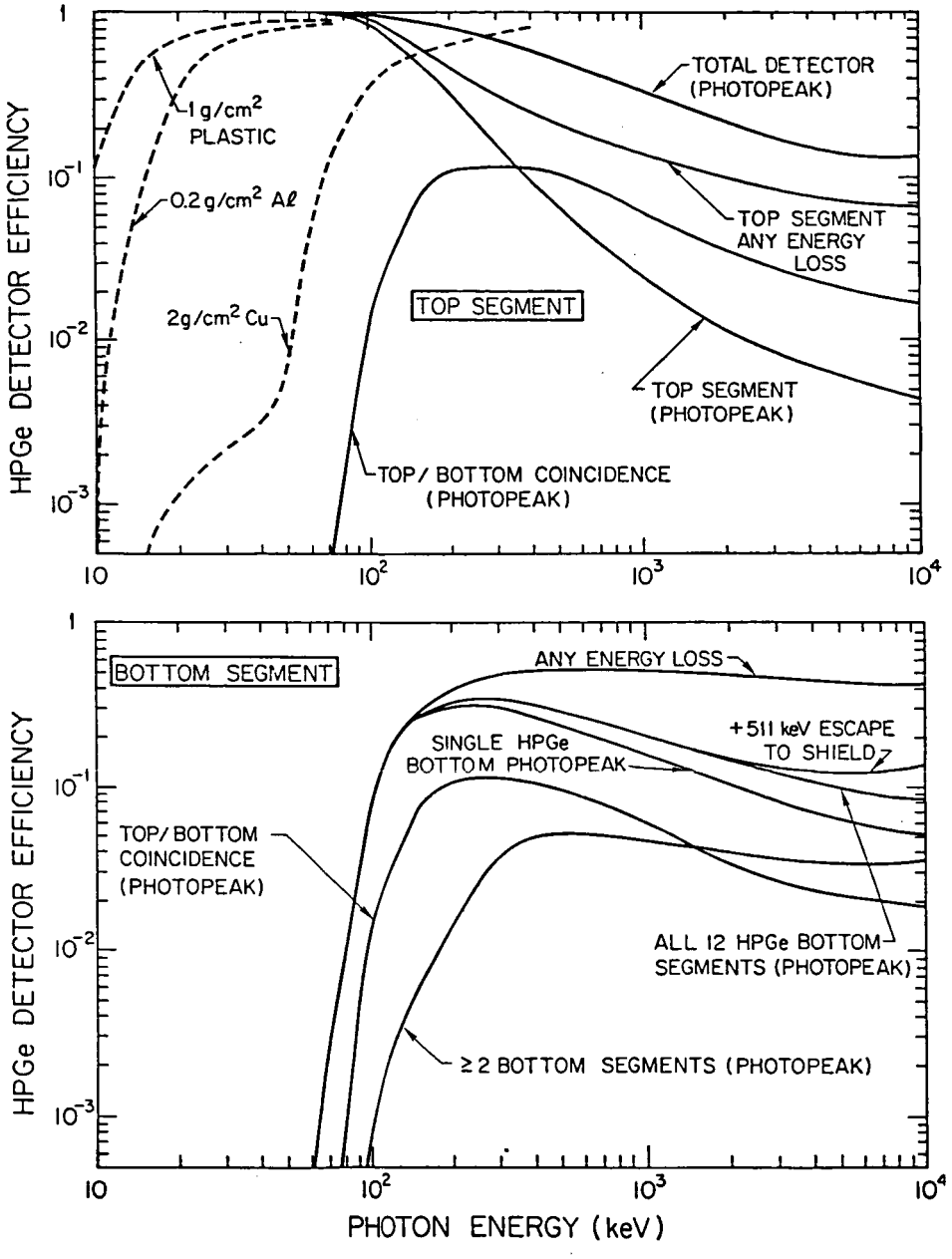

Figure B3. The photopeak efficiency for the top segment (upper plot) and bottom segment (lower plot) of the HPGe detector is shown here for different modes. In the upper plot the total (top and bottom) 12-detector array photopeak efficiency and the effect of various absorbers (dashed lines) is also shown. The bottom plot also shows the increase in efficiency at high energies from the addition of a 511 keV shield window.

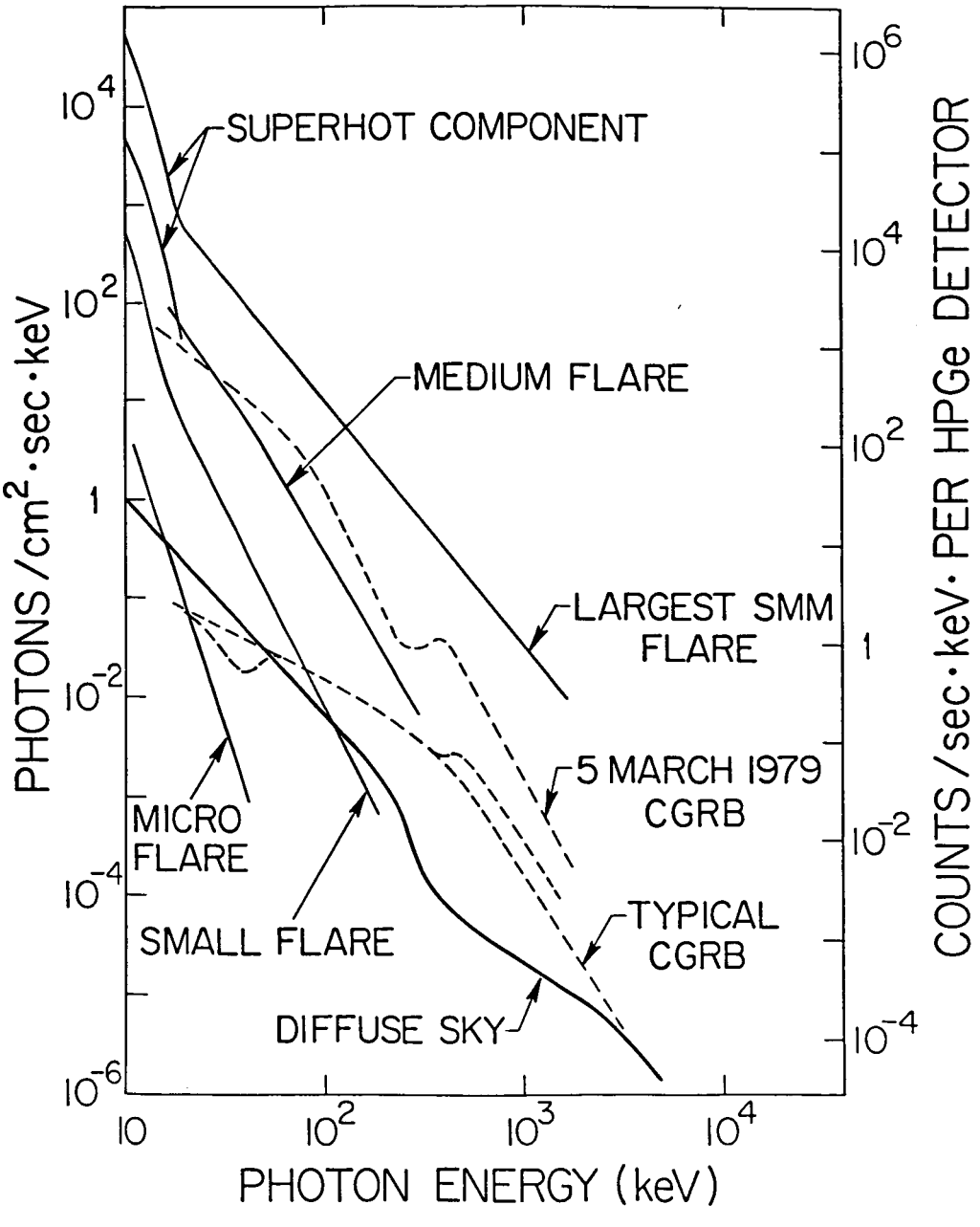

Figure B4. Typical spectra for various size flares and cosmic gamma-ray bursts (CGRB), compared with the background from the diffuse sky emission.

Table B1. Solar Flare Gamma-ray Lines								
Line Energy (MeV)	Excited Nucleus	FWHM (keV)	Fluences at Earth in FWHM (ph/cm^2)		Counts in HIGRANS (1000 s)			HIGRANS 3σ line sensitivity fluence ph/cm^2 (10^3/10^2 s)
			Lines	Flare Continuum	Line	Flare Continuum	Detector Background	
Prompt Lines								
~0.45	^{7}Li,^{7}Be	62	20	105	3.7×10^3	1.1×10^4	1.7×10^3	0.67/0.2
0.847	^{56}Fe	4.5	5	2	630	250	40	0.15/0.05
0.931	^{55}Fe	5	2	2	230	230	35	0.15/0.05
1.238	^{56}Fe	9	2.5	2	250	200	35	0.2/0.06
1.317	^{55}Fe	13	2.5	2	240	190	45	0.2/0.06
1.369	^{24}Mg	18	7.5	3	690	280	55	0.25/0.08
1.634	^{20}Ne	23	13	2.5	1.1×10^3	200	45	0.25/0.08
1.779	^{28}Si	25	8	2	630	180	45	0.25/0.08
2.313	^{14}N	54	6	3	410	205	50	0.3/0.1
4.438	^{12}C	115	10	1.5	510	80	20	0.25/0.08
6.129	^{16}O	120	10	1	440	44	10	0.2/0.06
Delayed Lines								
0.511	e^+	2–10	25	—	4.3×10^3	—	44–220	~0.25/~0.12
2.223	^{2}H	3(0.1)*	60(4.3)*	—	4×10^3	—	3	0.1/0.05

* This line has an intrinsic width of ~0.1 keV, so the HIGRANS instrument FWHM resolution (3 keV) is substituted. The 2.223 MeV fluence observed for the 27 April 1981 flare is highly attenuated because the flare is located near the limb; the value of 60 is for a comparable flare within ~70° of disk center.

The most sensitive indicator of ion acceleration is the narrow nuclear line of neutron capture deuterium at 2.223 MeV, which is delayed from the impulsive phase by the thermalization time for the neutrons. HIGRANS can detect at 3σ significance a 2.223 MeV line fluence $\gtrsim 10^3$ times smaller than the 4 August 72 event. If all flares accelerate ions to tens of MeV energy and the gamma-ray emission scales as the microwave burst intensity, then ~10 flares should be detected per month in the 2.223 MeV line near solar maximum.

Background Rejection. Sensitivity is very important for detection of long-lived gamma-ray lines such as the 511 keV positron annihilation line and the 2.223 MeV neutron capture deuterium line, whose emission lasts well past the impulsive phase. Also SMM observations show that following the impulsive phase there is a delayed phase in some (perhaps many) flares which is dominated by nuclear emissions (Forrest et al., 1986). Thus good background rejection in the range 0.4–2 MeV is important for HIGRANS, even though it is not the primary consideration.

Figure B5 plots the estimated background counting rate for HIGRANS. The background consists of: a) diffuse cosmic (and atmospheric) gamma-ray fluxes in the open aperture of the detector system; b) leakage of ambient γ-rays through the shield, and c) internal background in the detector, now known to be almost entirely due to radioactivity induced by cosmic rays and trapped protons and their secondary neutrons. For modern heavily shielded germanium detectors, this last effect is the dominant background in the range $0.4 \lesssim E \leq 2$ MeV. This energy range also contains most of the gamma-ray lines of interest.

The segmented HPGe detector provides the basic configuration for powerful background rejection techniques in the γ-ray line region from a few hundred keV to several MeV. Most of the induced radioactivity in the germanium detectors not anti-coincidenced by the active shield consists of β-decays; three isotopes, 82 min ^{75}Ge, 21 min ^{70}Ga, and 11.3 hr ^{77}Ge, dominate from 0.4 to 2 MeV. The energy deposition range of a β-particle is small, e.g., 0.08 cm at 1 MeV, and it can be said to deposit its energy at a single site. On the other hand, at energies above ~200 keV, because of Compton scattering (and pair production at >2 MeV), photons typically have multiple site energy loss signatures. Thus, by distinguishing between single and multiple site interactions in the detector volume, it

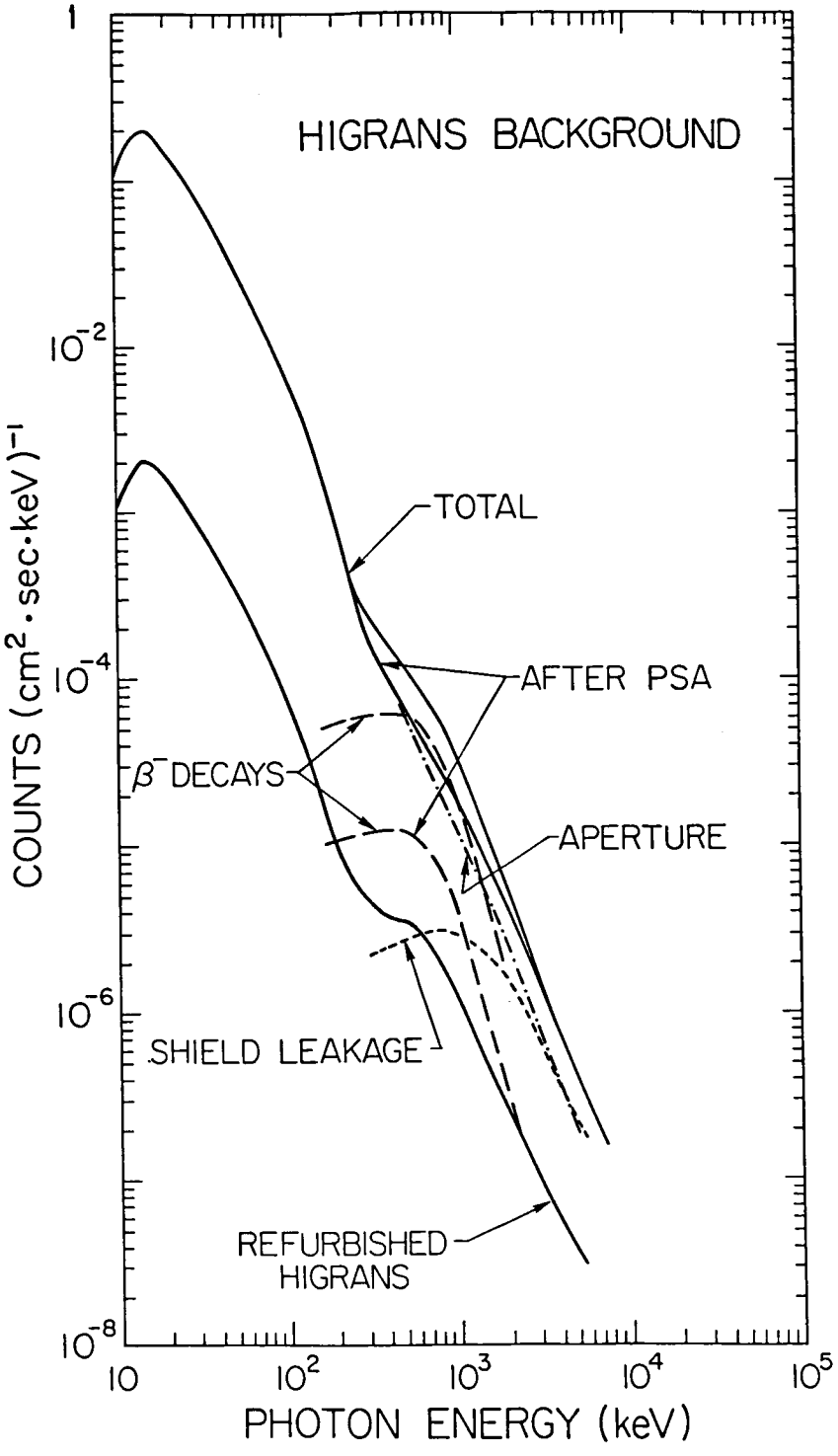

Figure B5. Expected background for HIGRANS. The level of β^- decays, both with and without pulse shape analysis (PSA), is shown. The expected background after refurbishment for collimated observations of weak cosmic sources is shown by the lower line.

is possible to reject most of the induced radioactivity background at energies from a few hundred keV to several MeV.

Techniques have been developed at UCB to separate single-site from multiple-site interactions. First, γ-rays which lose part of their energy in the front segment and the rest in the rear segment would be identified by front-rear coincidence. Second, in the rear segment, pulse shape analysis can be used to identify multiple-site interactions (for pure rear segment events) located at different radial distances. The energy deposited in the Ge detector at a given site produces charge carriers, electrons and holes, which travel radially in the electric field of the detector to the central and outer contacts. The motion of the charge carriers induces a current at the electrodes; the measured signal is proportional to the integrated charge. Thus the current pulse shape at the preamplifier input depends on the radial location of the site of energy deposition. Typically, charge collection takes up to 350 nsec. When the energy deposition of a multiple-site interaction is distributed in radius, the pulse shape becomes a superposition of single-site pulses.

Figure B6 shows examples of single-site and multiple-site current pulses observed from a segmented coaxial Ge detector. At UCB we have calculated the detailed shape of the current pulse waveform for single-site energy losses typical of single photopeak absorption events and β-decay radioactivity, and for normal photons, using the distributions of energy depositions resulting from the Monte Carlo photon propagation program (Roth, Primbsch and Lin, 1984). Our calculations indicate that for a uniform Ge detector with near ideal noise characteristics it may be possible to reject $\gtrsim$95% of the single-site events while retaining $\gtrsim$80% of the multiple-site events at ~800 keV energy. With current balloon flight electronics we have achieved ~80–90% singles rejection with ~60–70% retention of multiple events at ~800 keV, using only two parameters (peak height and time-to-peak) of the HPGe current pulse (Figure B7). Since the sensitivity is proportional to signal/$\sqrt{\text{background}}$, even the current balloon system gives a gain of a factor ~1.4–2 in sensitivity. To place this in perspective, 2–4 times as much Ge detector volume would be required to achieve the same sensitivity without segmentation and pulse shaping techniques.

For HIGRANS, pulse shape analysis would only be used at low count rates, when the background due to induced radioactivity dominates (see Figure B5). Only ~80% rejection of single site events is sufficient to reduce the contribution from induced radioactivity to well below the aperture flux. If HIGRANS is refurbished for narrowly collimated observations of weak cosmic sources, we plan to improve this rejection to ~95%.

Electronics

Each detector has independent signal paths for the front and rear segments as indicated in Figure B2. The analog electronics is essentially the same as used in the UCB balloon system (Figure B8). For each signal path (Landis et al., 1970), this includes a cooled FET, wide bandwidth charge sensitive preamplifier, followed by dual shaping amplifiers. A slow shaper-amplifier (~10 μs time constant) is used for pulse height analysis, and a fast shaper-amplifier-discriminator (~400 ns) supplies fast pulses for coincidence, pileup rejection, timing, and rate accumulations. (The two amps are not shown separately in Figure B8.) The pile-up rejection system, besides allowing operation at rates up to 5×10^4 s^{-1} per detector without resolution degradation, will also remove a large fraction of the 54 keV background line and 54–67 keV background continuum due to $^{73}Ge^m$. This has a 54 keV transition followed by a nearly prompt (4 μs) 13 keV de-excitation.

The shaped pulses go to two separate Analog-Digital Converters (ADC's). At energies below 400 keV a fast 10-bit ADC (1024 channels of ~0.4 keV/ch) is used to accommodate count rates up to ~10^5/s. Above 400 keV the slower 12-bit ADC (4096 channels) used in the balloon instrument covers the narrow gamma-ray line region up to 2.5 MeV with ~0.5 keV/channel width. Finally, in order to achieve a dynamic range greater than that allowed by the 12-bit PHA, the shaping amplifier contains a switchable 8x attenuator controlled by a discriminator on the preamplifier output line. The status of the gain switch is latched by the PHA, when triggered, as a 13th data bit. This attenuator system (also part of the balloon instrument) provides a channel width of ~5 keV from ~2.5 MeV to 20 MeV.

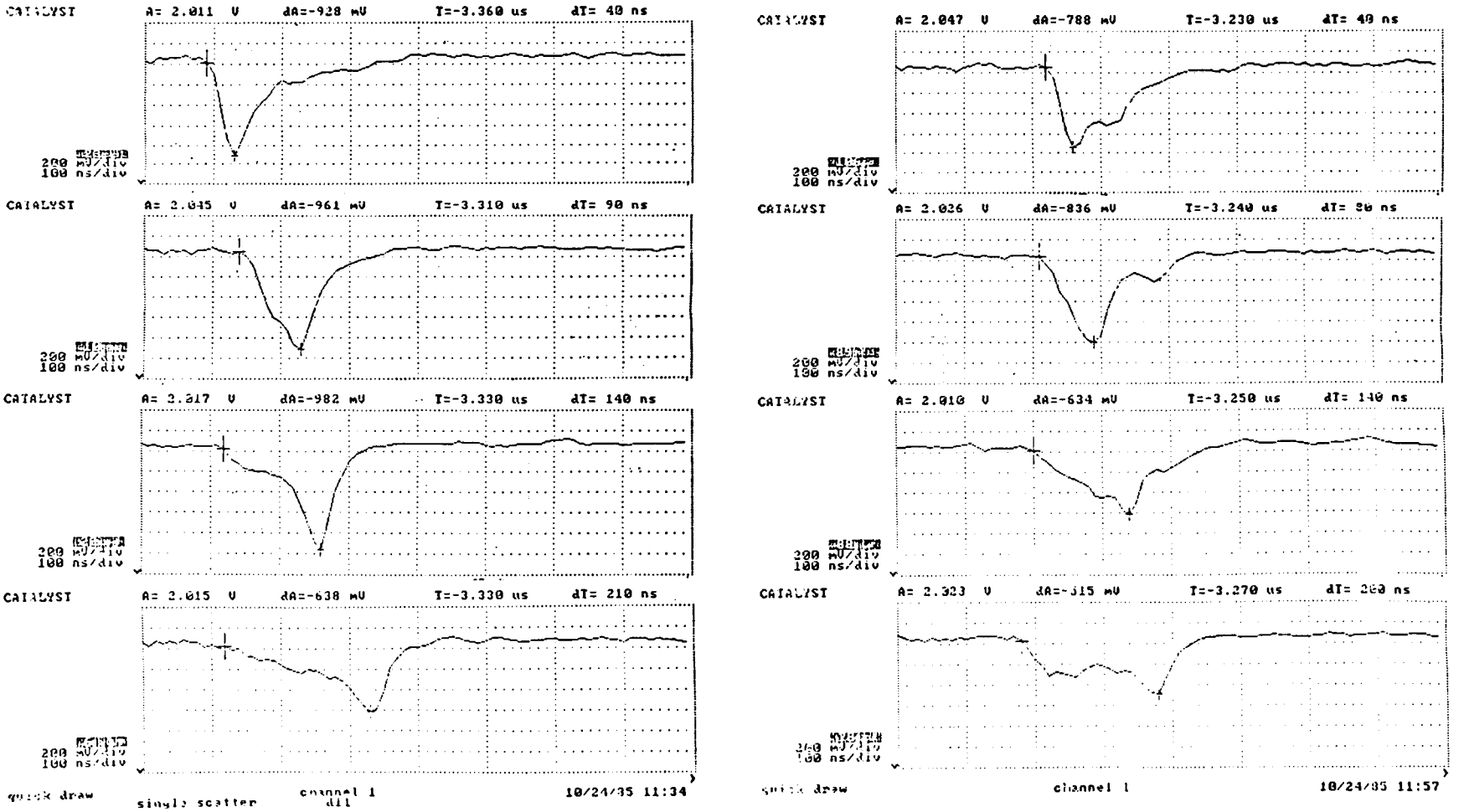

Figure B6. (left) Current pulse shapes obtained for 817 keV single site interactions, ranging from interactions near the central electrode (top) to the outer edge (bottom) of the detector. (right) Current pulse shapes obtained for 835 keV multiple site interactions (^{54}Mn source) for comparison at about the same time to peak. Note the peak height is generally lower.

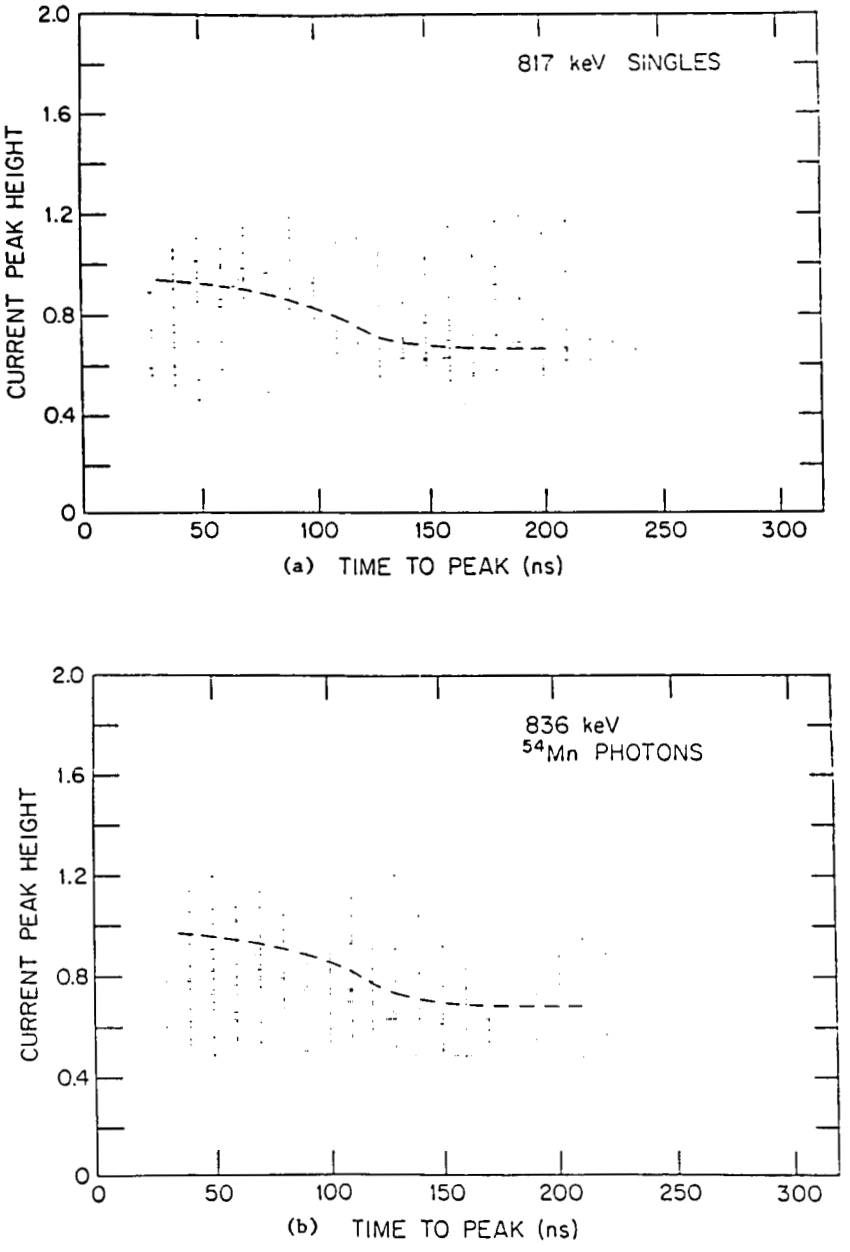

Figure B7. Distribution in peak height versus time to peak: (a) singles; (b) multiples.

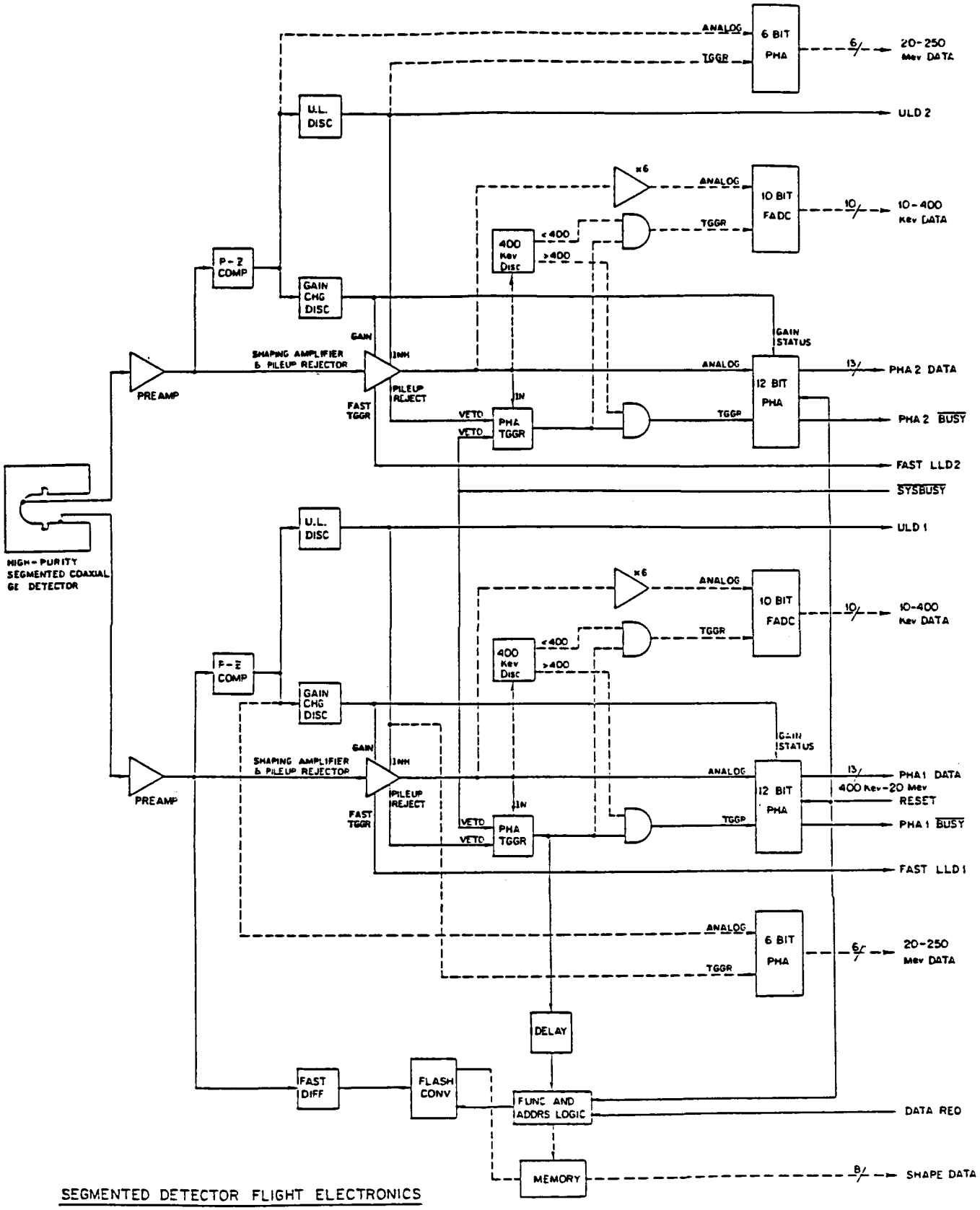

Figure B8. Block diagram of the electronics for the dual-segment HPGe detector. The solid lines show the electronics currently used in the balloon instrument. The dashed lines indicate the additions envisioned for HIGRANS.

The digital output of the ADC's is sent either directly to the telemetry system together with timing to msec, or to incrementing memories where the pulse height spectra are accumulated, depending on the mode of the instrument.

Pulse Shape Analysis. The present pulse shape analysis circuitry, which is connected only to the signal path from the bottom segment, consists of a fast differentiator and a LeCroy model 2261 Channel Analyzer utilized on the balloon instrument as a Pulse Shape Analyzer (PSA). The fast differentiator, with a time constant of 10 ns, extracts the detector current waveform from the preamp output waveform and passes it to the PSA.

The PSA module consists of a Charge Coupled Device (CCD), support, and readout logic circuitry. The CCD is an analog shift register (sometimes referred to as a charge packet bucket brigade) with a length of 640 cells and a clock speed of 100 Mhz. An input signal is sampled, converted into a charge packet, and shifted at the 100 Mhz rate; thus the time length of the device is 6.4 μs with a resolution of 10 ns. Upon receipt of a Stop signal, the 100 Mhz clock signal is replaced with a 100 Khz clock signal, the charge packets are converted to voltage levels as they arrive at the back of the CCD, and these voltage signals are passed to a 12-bit ADC. The 12-bit words are stored in a local memory and become available for readout at the completion of the conversion process.

For HIGRANS the PSA would be simplified by replacing the LeCroy 2261 by a flash ADC and associated storage memory. A dedicated microprocessor would be used to analyze the shape and decide whether a single or multiple event had occurred. From our measurements with the LeCroy we believe that a 8-bit flash ADC with ~20–30 ns time resolution may be adequate for our needs. Further studies of PSA circuitry are going on now at UCB.

The data from the ADC's and PSA's, together with data from the shields, go to the digital electronics (Figure B9). Because of the burst nature of the data, a significant amount of RAM storage is required. Access to the spacecraft tape recorders will also be required by HIGRANS and the other instruments for large flares.

Cryostat and Cooler

The cryostat must maintain the temperature of all twelve germanium detectors at 90°K and provide a secondary thermal control surface at ~150K for mounting of the preamp FET's. The mechanical layout must have sufficiently low mass to avoid background problems. In addition, the design should provide vibration immunity and sufficiently low heat leak. We have chosen an approach utilizing a primary cold plate for detector mounting. Efficient thermal isolation is attained through the use of a unique fiberglass strap cold plate suspension with multi-layer insulation surrounding the secondary shroud. This design presents a simple mechanical interface to the germanium detector modules. At UCB/UCSD we are presently studying whether one large vacuum volume for all 12 detectors or several separate vacuum chambers, each with 3 or 4 detectors, is preferable. The design is directly adaptable to alternative cooling techniques such as mechanical refrigeration.

At present we plan to use a two-stage (methane-ammonia) solid cryogen cooler for HIGRANS. These coolers have been developed and flown on the Einstein and HEAO-3 spacecraft, and no new development is anticipated. The cooler for HIGRANS is sized for a three-year lifetime at 90°K. We plan to monitor progress on a Sterling cycle mechanical cooler, currently being developed at GSFC. This cooler provides ~8 watts of cooling to ~90°K with input power of ~200 watts. The large cooling capacity would permit much more relaxed thermal design for HIGRANS. In the study phase we hope to determine whether the level of microphonics produced by this cooler is acceptable for operation of the ultra-low noise HPGe detectors. The reliability and cost of such a cooler has also to be determined.

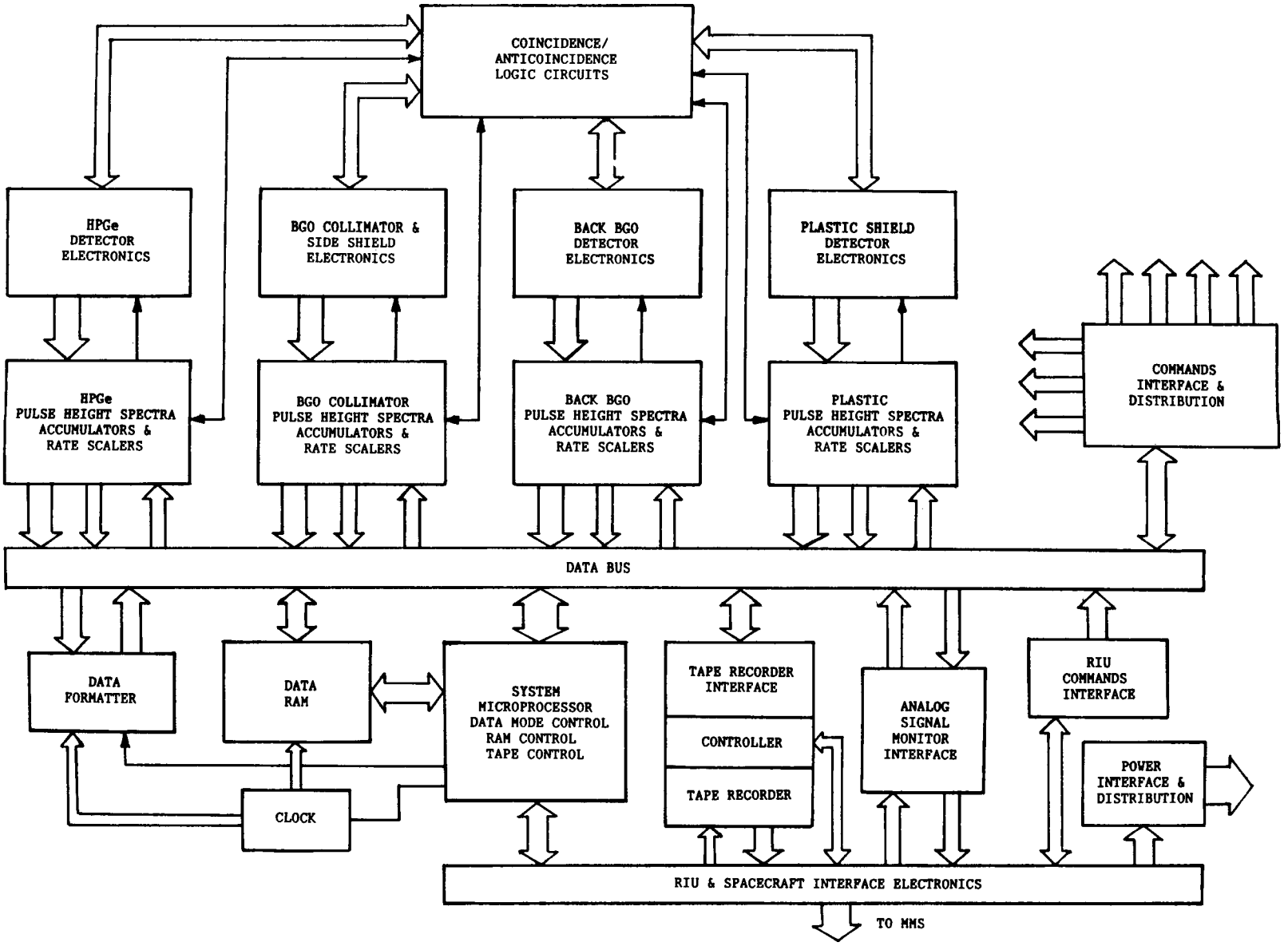

Figure B9. Block diagram of HIGRANS digital electronics.

HIGH ENERGY DETECTOR AND SHIELD

The detection of gamma-rays and neutrons above 10 MeV is a crucial part of an overall solar flare observation program, since these radiations are a signature of the highest energy electrons and ions that are accelerated in the flare process. The high-energy capability of the HIGRANS detector is therefore an important part of the SHAPE instrument complement.

The 5-cm thick BGO shield annulus and the three rear sections are composed of a matrix of BGO units (Figure 3 of main text), each with its own photomultiplier tube, preamplifier, discriminator, high-voltage power supply, LED light pulser, and servo-gain-control electronics. The BGO assembly plays several roles for the HIGRANS instrument. At energies below 20 MeV, the assembly provides shielding for the HPGe array against gamma-ray background. It also provides limited collimation for analysis of radiation from cosmic sources using techniques analogous to those for the SMM GRS. The annulus and first rear section also reject gamma-rays which are Compton scattered in the HPGe and deposit energy in the BGO above the shield threshold level. This makes the instrument response matrix more nearly diagonal, permitting more accurate determination of the incident photon spectrum.

At energies above 20 MeV, the three rear sections together with the HPGe array form a multilayer high-energy gamma-ray and neutron spectrometer. The relative energy loss in these layers will be used to differentiate between events produced by gamma-rays and neutrons. The feasibility of this technique has been proven on a smaller scale in the SMM GRS. The improvement in the neutron sensitivity of HIGRANS, compared with that of GRS, is a factor of 10 or more (Figure B10). The sensitivity to gamma-rays above 20 MeV shows a similar improvement of a factor of 5 or more. This improvement is a result of a much larger area and energy containment of the HIGRANS shield and the added benefits of higher operating energy, better energy resolution, and more sophisticated shield logic to deal with self-gating effects.

The forward layer of the rear shield is also pulse-height analyzed over the energy range from 100 keV to 20 MeV, thus complementing the HPGe data with high photofraction measurements of broad lines and the continuum. The charged-particle 4 pi steradian shield consists of a dome and a rear section, fabricated from low-light-loss plastic scintillator and viewed with photomultiplier tubes.

The UNH group, which will lead the design effort for the high-energy detector and shield for HIGRANS, has had considerable experience in the designing of a similar scheme for the SMM GRS, which made the first measurement of high-energy solar flare neutrals. This group is currently involved in the study of a layered detector technique similar to that planned for HIGRANS. This includes testing of the technique in a neutron beam, which is currently in progress, as well as future testing in electron or gamma-ray beams. During the study phase UNH will lead a design effort to optimize the high energy gamma-ray and neutron response of the HPGe and layered BGO shield configuration.

CESR will develop and build the BGO scintillator with all associated analog electronics. This effort will be a direct continuation of the UCSD/UCB/CEA collaborative balloon project for gamma-ray spectroscopy, in which the CESR is building a similar BGO shield. For that project, 52 BGO bars have been purchased from Crismatec, in Grenoble, a company which is jointly owned by the Rhone-Poulenc chemical corporation and the French Atomic Energy Commission. The material has proven to be of excellent quality. The largest shield pieces have dimensions $5 \times 5 \times 24.4 cm^3$, and are cut from raw ingots about 7.5 cm in diameter and 25 cm long.

At present, the standard size of the Crismatec ingots is 8.5 cm diameter by 24 cm long. If the HIGRANS shield were cut from these ingots, it would consist of about 96 bars. This seems quite feasible, but a reduction in the number of bars would result in reduced complexity. 10-cm diameter material has been grown, but the length is only 16 cm. CESR has requested longer materials, and this is now being studied by Crismatec as an R&D proposal.

The high index of refraction of BGO crystals makes it difficult to collect the light at the PMT photocathode. CESR has discussed the possibility of designing and machining BGO bars with a

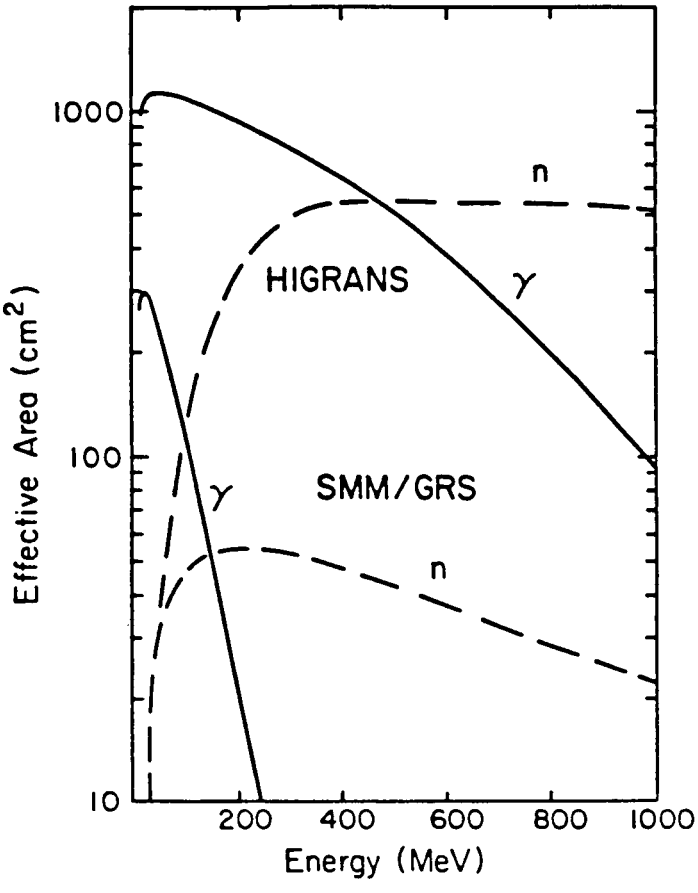

Figure B10. Calculated sensitivity of the HIGRANS BGO gamma-ray and neutron spectrometer compared to the Gamma-ray Spectrometer on SMM (SMM/GRS).

"truncated cone" geometry at one end, i.e., with the rectangular bar cross section sculpted into a small circle whose diameter matches that of the photocathode. This would provide a natural light guide which should improve light collection. It appears quite feasible to accomplish this, give the complex BGO geometries now being machined by Crismatec.

The present balloon system design incorporates one photomultiplier (based on a Hamamatsu R-1847, but with 10 dynodes instead of 9) per bar; the baseline design for HIGRANS would be similar. The performance of this combination is quite adequate for an anticoincidence well: 100 keV resolution at 662 keV, and a lower threshold of 50 keV. This is sufficient, for example, to establish a .511 MeV windows for pair spectrometry. A substantial reduction in mechanical and electronic complexity could come about by using photodiodes to read the BGO bars, instead of photomultiplers. The problem encountered to date with the photodiode/BGO combination to date has been the high noise of the photodiode, which leads to lower thresholds of several hundred keV, clearly not acceptable in this application. However, in the context of an R&D effort for an ESA proposal, the CESR will closely follow PIN diode development work being carried out in England and Germany. By modifying the design of these diodes from that of a parallel plate configuration to a plate plus a point collector, the capacitance, and thus the noise, are much reduced.

To summarize, over the study period, CESR will work on the following questions.

1. Design and fabrication of large BGO bars with a "natural" light guide incorporated.
2. The use of low capacitance photodiodes to read the BGO bars.
3. Breadboard design of an electronic system which incorporates .511 and 1.02 MeV windows.
4. The use of BGO as a neutron and high energy gamma-ray detector.
5. The use of a BGO shield to provide coarse localization of gamma-bursts, by comparing responses in different shield sections. This idea has been successfully implemented on, for example, the HEAO-C gamma-ray spectrometer; the first scientific flight of the balloon shield may allow this concept to be tested.

The group at the Max Planck Institute for Extraterrestrial Physics, which is responsible for the shield and instrument mechanical support structure, and the charged-particle shield, has had related experience in their work on the shields for the GRS on SMM and EGRET on GRO. MPE plans to do a preliminary study of the BGO shield and instrument mechanical design and of the plastic scintillator particle shield.

REFURBISHMENT OF HIGRANS FOR COSMIC OBSERVATIONS

HIGRANS is designed to be a powerful instrument for spectroscopy of solar flare and cosmic gamma-ray burst sources. It could be refurbished into an outstanding instrument for detection of weak steady cosmic hard X-ray and gamma-ray sources. The primary changes would be aimed at reducing the background further by: (a) narrowing the field of view so background from diffuse sky fluxes is reduced, (b) increasing the shielding thickness to reduce leakage, (c) optimizing the pulse shape analysis techniques to further reject background from induced radioactivity, and perhaps (d) adding a coded mask to provide imaging. Furthermore, a careful choice of materials for the cryostat and other structure inside the BGO will be required to reduce internal background at lines of interest. Figure B5 shows the effect of decreasing the FOV to $\sim 10^{\circ}$ FWHM, doubling the BGO annulus thickness to 10 cm, and optimizing the pulse shaping to reject 95% of the single site interactions. The background is reduced by a factor of $\sim 10^2$ below a few hundred keV and ~ 10 at energies of $\gtrsim 1$ MeV. For long observing periods, this background reduction implies a gain in sensitivity of a factor of 3 to 10 over the burst version of HIGRANS. Further study of these options is needed if it is decided to refurbish HIGRANS.

References

Forrest, D. J., W. T. Vestrand, E. Rieger, G. H. Share, *Bulletin American Astr. So., 18,* 697, 1986.

Landis, D. A., F. S. Goulding and R. M. Pehl, IIEEE Trans Nucl. Sci., NS-18, 115, 1970.

Luke, P. N., *IEEE Trans. Nucl. Sci., NS-31,* 1984.

Matteson, J. L., P. L. Nolan, W. D. Paciesas and R. M. Pelling, *Space Sci. Instr., 3,* 491, 1977.

Pehl, R. H., *NASA Tech. Memorandum 79619,* 473, 1978.

Roth, J., J. H. Primbsch and R. P. Lin, *IEEE Trans. Nucl. Sci., NS-31,* 367, 1984.

APPENDIX C: THE LOW-ENERGY IMAGING SPECTROMETER

SCIENTIFIC AIMS

The **Low-Energy Imaging Spectrometer (LEIS)** is designed to address several outstanding problems in solar flare physics. It is the first solar physics instrument with the capability of obtaining high spatial and spectral resolution data, with high time resolution, in both the EUV and UV wavelength ranges simultaneously. The EUV and UV images are monochromatic. It is therefore possible to make detailed simultaneous observations with a single instrument of the high-temperature coronal flare plasma (up to 2×10^7 K) and the underlying low-temperature transition region and chromospheric plasma (as low as 8×10^3 K). These data, when combined with the observations obtained by **GRID**, **HIGRANS**, and **SIPS**, will allow major progress to be made in several areas of solar flare research.

LEIS represents an improvement in several respects over previous instrumentation, when applied to solar flares. The **NRL** monochromatic imaging EUV instrument on Skylab (SO82-A) had lower spatial resolution (2 instead of 1 arcsecond) and had poor time resolution for observations of the impulsive phase of solar flares because it was not designed specifically for flare research. Very little information on the preflare or the impulsive phases of flares was obtained with this instrument. Although an excellent UV spectrograph was also flown by **NRL** on Skylab, the instrument had very poor spatial resolution (2×60 arcsecond), and it was therefore not possible to link observations made with this instrument to specific high-temperature flare features observed with the EUV spectroheliograph. Finally, no high-energy flare instruments were flown on Skylab because the mission was not designed primarily as a flare mission, and the X-ray telescope on Skylab did not obtain monochromatic images. The more recent **SMM**, **P78-1**, and **Hinotori** spacecraft were designed specifically for solar flare research. However, none of the instruments on these spacecraft had sufficient spatial resolution (< 8 arcsecond) to resolve adequately the high-energy nonthermal, high-temperature thermal, and transition region flare components. Such simultaneous observations have not been obtained on any previous solar physics mission. The specific questions that **LEIS** can address are discussed below.

(a) What is the Pre-flare Magnetic Configuration?

All theories that attempt to explain the origin of solar flares depend on specific configurations of the magnetic field. Most, if not all, flare theories assume that the energy released in solar flares is magnetic energy stored prior to flare onset. In some theories, energy release can occur in a single magnetic flux tube or loop, while in other theories, the energy is released when two or more loops physically interact. Up to now, there are no concrete data on the preflare magnetic configuration. The field configuration can only be determined by observing the plasma confined to the preflare loop or loops. Existing observations are so sparse that we do not presently know the temperature and density of the plasma confined to such loops, or the initial sizes and orientations of the loops. It is quite possible that the preflare temperature is quite low, considerably less than 10^6 K, because if the temperature were much higher than that, the preflare loops would have been observed with Skylab instruments. **LEIS** obtains monochromatic images in spectral lines that span a continuous range of temperature from about 2×10^4 K (C II) up to 2×10^7 K (Fe XXIV). Therefore, **LEIS** has an excellent chance of making the first detailed and thorough observations of preflare loop structures. The images obtained at different temperatures, when interpreted using plasma diagnostic techniques, should enable the emission measure distribution and density of the plasma in the loops to be determined, as well as the size, number, and orientation of the loops.

When these data are combined with simultaneous ground-based microwave observations, it should also be possible to obtain quantitative measurements of the magnetic field strength and structure within the loops. Such detailed results would unambiguously eliminate certain flare theories from further consideration and should provide strong support for others.

(b) What is the Relationship of the High-Energy Accelerated Particles to the Lower-Energy Thermal Flare?

Bursts of hard X-ray and γ-ray emission, evidence of particles accelerated to very high energies, occur during the impulsive phases of many flares. The energy of these particles, as derived from the photon spectra, is quite high and in some cases is about the same as the total energy released in a flare. Consequently, one current scenario for energy transport in a flare is that the magnetic energy is first converted into accelerated particles, which subsequently become thermalized, producing the thermal soft X-ray flare by chromospheric evaporation and the H-α flare by chromospheric heating. While energy transport in some flares may be explained in such a fashion, severe problems with this interpretation arise for other flares. For example, energy input in some flares is required long after hard X-ray emission has ceased. In certain other events in which soft and hard X-ray emission features are observed simultaneously, the features are not cospatial in the manner expected in the simplest evaporation picture. It has been difficult to address this problem with **SMM** because of the coarse spatial resolution and lack of adequate coalignment of the **HXIS** and **UVSP** instruments.

LEIS will obtain images during the impulsive phase in lines, such as Si IV, which reveal the sites of chromospheric heating due to energy deposited by high-energy electrons. These sites should be the footpoints and sources of evaporation for the thermal coronal flare plasma that produces the soft X-ray flare. These observations can be combined with the **GRID** images to give a complete picture of the geometry of the high-energy flare. The UV images, combined with **LEIS** EUV images in spectral lines such as Fe XXIV (2×10^7 K), which indicate the locations, sizes, and orientations of the soft X-ray flare loops, will directly test the chromospheric evaporation hypothesis. Furthermore, the plasma diagnostics available with high-resolution spectroscopy in the UV and EUV will enable the interaction of the coronal portion of a flare with the chromospheric flare to be studied in detail. For example, theoretical modelling has shown that deposition of energy by high-energy electrons produces a chromospheric response that is different from the response expected from energy deposition by conduction fronts. Moreover, recent calculations indicate that anomalous conductivity can produce a chromospheric response different from the response expected using classical conductivity. The behavior of the chromosphere can be inferred from the intensities, profiles, and Doppler shifts of UV and EUV spectral lines. **LEIS** will provide detailed observations for testing predictions of many of the numerical and analytic models of coronal-chromospheric interactions.

(c) Flare Energetics and Plasma Diagnostics.

Although the total energy budget of a flare has been considered previously using data from Skylab and **SMM**, various difficulties with these data have prevented a definitive treatment of this problem. The total energy released in a flare, and its transport in different flare structures, are clearly important parameters for flare theories. **LEIS**, because of its unique simultaneous UV and EUV capability, which translates into a very broad temperature coverage, will allow the flare energetics problem to be addressed in detail for temperatures in excess of 10^4 K. Another important aspect of **LEIS** is the spectroscopic, as well as imaging, mode of operation. The wavelength ranges of **LEIS** have been chosen to cover spectral lines important from the diagnostics standpoint. For

example, observations of the UV intersystem lines of O V, S IV, and O IV, when combined with allowed lines of Si IV and N V, enable the electron density of the regions heated by electron beams to be determined. The line ratios can be compared directly with theoretical line ratios calculated by numerical simulations. Similarly, the lines of Fe IX in the EUV region are excellent indicators of electron density for plasma near 10^6 K. In addition, the intensities of allowed lines covering a broad temperature range can be used to calculate the differential emission measure, which is a parameter that can be related to energy transport processes and dynamics in the flare plasma. Finally, the spectral resolution is high enough to measure line profiles and wavelength shifts of highly turbulent plasma or plasma ejected as surges and sprays; e.g., the Fe XXI line at 1354 Å is an excellent indicator for chromospheric evaporation. The combination of plasma diagnostics with Doppler information over a very broad temperature range provides the basis for unraveling the physical conditions in the flare plasma and the way these conditions change as a flare evolves.

(d) High-Energy Proton Beams

There is considerable interest in whether high-energy proton beams exist and, if they exist, how deeply they penetrate into the chromosphere. The protons can in principle be detected from the charge-exchange interactions with hydrogen atoms as they are thermalized. Since the beams are moving downward into the atmosphere, the red wing of Lyman-α exhibits a characteristic asymmetry when observed at Sun center. Although interpretation of any Lyman-α asymmetry may be complicated due to the presence of a C I free-bound continuum, **LEIS** can nevertheless make the observations necessary to infer whether proton beams exist.

INSTRUMENTATION

The **LEIS** instrument, shown schematically in Figures 4.3 and C-1, represents a synthesis of several of the instrument concepts considered by the **MAX '91** study committee. **LEIS** consists of an off-axis parabola operating as a prime-focus telescope, a slit assembly, a toroidal grating assembly, and an imaging detector. Functionally, **LEIS** operates as a high-speed spectroheliograph. The telescope section is similar to that of the Ultraviolet Spectrometer instrument prepared by the Harvard College Observatory for Skylab; the spectrograph is a derivative of the spectrograph section of the **SEUTS** instrument designed at GSFC for the Spacelab program; the detector is of the type suggested by L. Golub for the normal incidence Soft X-ray Polychromator; and the control system is patterned after that used in the **SMM–UVSP** instrument.

The primary mirror has a two-meter focal length and is articulated, permitting the optic axis of the telescope to be directed to any position on the solar disk without moving the instrument as a whole. The grating assembly contains two toroidal gratings, one optimized for the 1300 Å region and the other for the 250 Å region. The detector is an intensified television camera based on a Plumbicon tube and using tapered fiber optic lenses to match the pixel size required at the focal plane to those required by the intensifier and Plumbicon sections. EUV sensitivity is provided by a fine-grained P-45 phosphor screen deposited on one half of the input end of the tapered fiber optic lens. UV sensitivity is derived in a similar way with a "to be determined" phosphor (possibly coranene) on the other half of the input fiber optic lens. The Plumbicon readout electronics are designed to permit selective addressing of areas of the focal plane, so that only the desired portions need to be sampled.

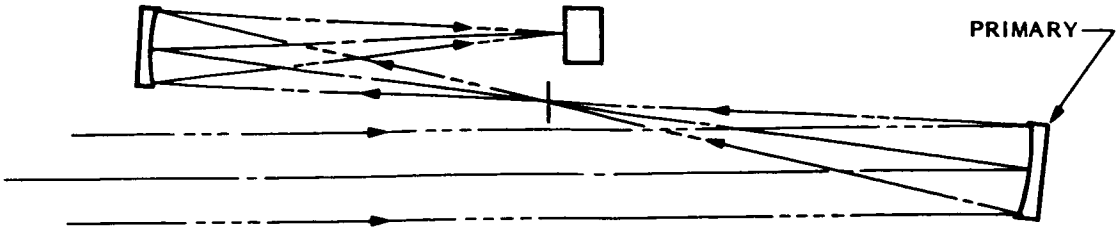

Figure C-1b: Schematic of the **LEIS** optical system - top view.

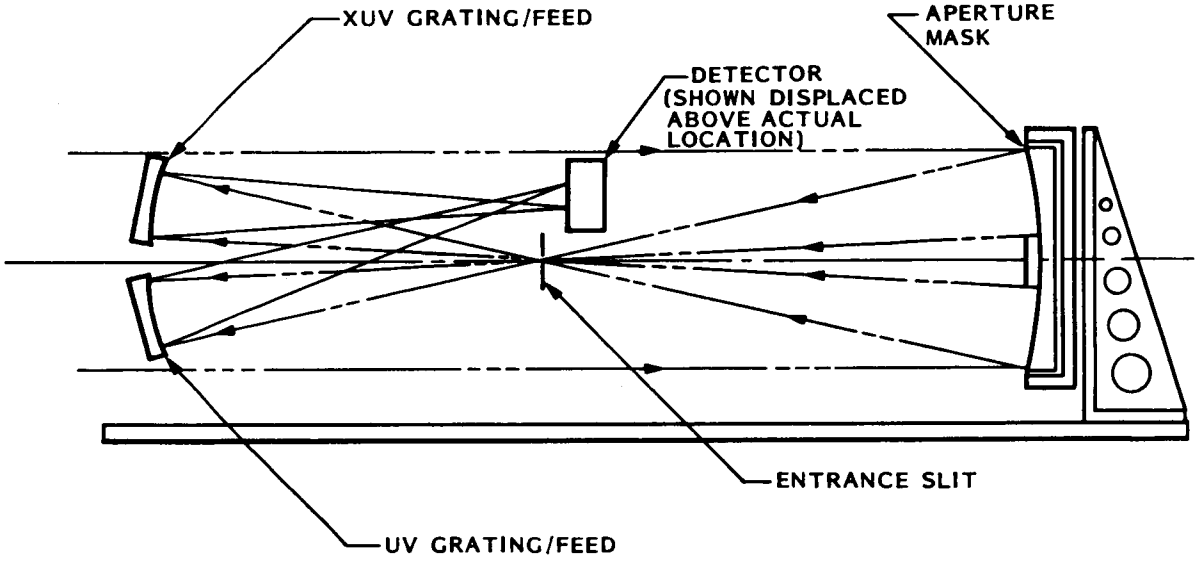

Figure C-1a: Schematic of the **LEIS** optical system - side view.

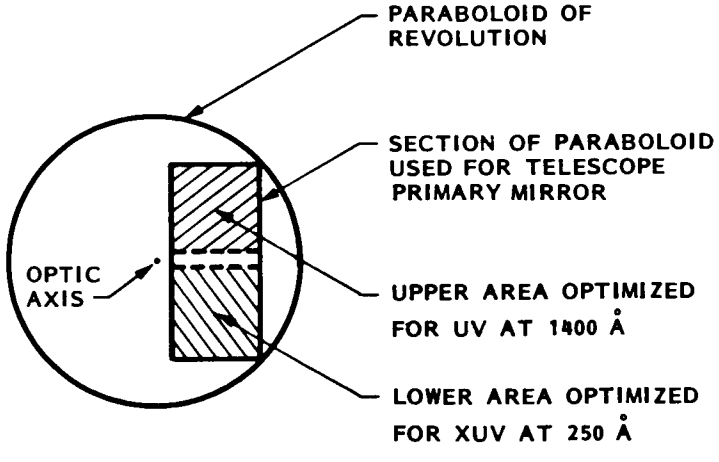

Figure C-2: Schematic showing section of paraboloid used for primary mirror.

A discussion of the instrument may begin with the telescope primary. As shown in Figure C-2, the primary mirror is a rectangular section cut from a paraboloid of revolution. The aspect ratio of the rectangular section is near 2:1, and defines two collecting areas. The lower collecting area is optimized for EUV reflectivity, probably with multilayer mirror technology. The upper area is optimized for UV reflectivity and will probably be coated with aluminum/magnesium-fluoride. Since they are part of the same parabolic surface, the upper and lower sections of the telescope primary have a common focus and the UV and EUV images are rigorously co-aligned on the entrance slit of the spectrograph. Note, however, that the chief rays, defined by lines from the center of each section to the center of the entrance slit, are not coincident, but converge toward the entrance slit, and then separate again inside the spectrograph, as shown in Figures 4.3 and C-1. It is this feature of the telescope that allows the two sections of the spectrograph to operate simultaneously and independently. The projected slit length on the Sun is 8 arcminutes in the baseline version of the instrument.

The upper grating in Figures 4.3 and C-1a is ruled for the EUV and is nominally the same as the grating originally specified for the **SEUTS** spectrograph. It has a ruling frequency of 3600 grooves per millimeter and a nominal working distance of one meter. Use of the toroidal figure permits astigmatism to be substantially eliminated over the working wavelength range. The grating rulings are parallel to the plane of the drawing of Figure C-1a and to the entrance slit, which lies in the plane of Figure C-1a. The normal to the EUV grating is tipped down such that the chief ray strikes the grating at normal incidence. The plane of dispersion is perpendicular to the plane of Figure C-1a and contains the chief ray. The spectrum is focussed to one side of the entrance slit as shown in Figures 4.3 and C-1b, and directly behind the entrance slit as the slit is seen in Figure C-1a. (The detector is shown above its actual location in Figure C-1a to avoid confusion in the ray diagram.) Note that the plane of dispersion is parallel to the baseplate. The operating range and resolution of the EUV spectrograph are yet to be determined, but will probably be centered at about 260 Å. Our first look at the rough design parameters for the EUV spectrograph gave an operating range of about ± 20 Å about the central wavelength. This range would allow us to have 0.04 Å resolution elements, or R = 6250 for a 1000×1000 pixel detector, and would correspond to a sampling interval of 48 km/s in the Doppler velocity domain.

Operation of the UV spectrograph section is analogous to that of the EUV section. The toroidal UV grating is the lower one in Figure C-1a, and its normal is tipped up, such that the chief ray from the upper section of the primary mirror is perpendicular to the grating rulings. The plane of dispersion is, again, perpendicular to the plane of the drawing of Figure C-1a, and contains the chief ray so that it is parallel both to the baseplate and to the EUV dispersion plane. The central wavelength of the UV section is at about 1300 Å in order to observe the hydrogen Lyman-α line at 1216 Å and several strong lines of Si IV, O IV, and S IV near 1400 Å that **UVSP** experience showed to be very useful in deriving densities and emission measures at transition zone temperatures. The rough design parameters for this section gave a spectral range of about 12 Å and the same numerical resolution as the EUV section, assuming the use of a toroidal grating with the same radii of curvature as those of the EUV grating. (This assumption is not a requirement; the UV section may have either a longer or a shorter working distance than the EUV section and could even be a completely different form of spectrograph should we find it to be an advantage during the Phase A study.)

After leaving their respective gratings, the two chief rays cross behind the entrance slit so that the UV and EUV spectra are separated on the focal plane. This geometry also compensates for

most of the focal plane tilt error resulting from the fact that the slit is not perpendicular to the chief ray of either spectrograph section. The EUV and UV dispersion planes form a dihedral angle whose vertex is a line perpendicular to the plane of Figure C-1a and passing through the center of the entrance slit. The residual tilt error in the trial designs is only 0.3 degrees and results in a blur error of less than one micron at the focal plane for an f/20 system so that further correction is not necessary. The plane of the detector is perpendicular to that of the baseplate in this design.

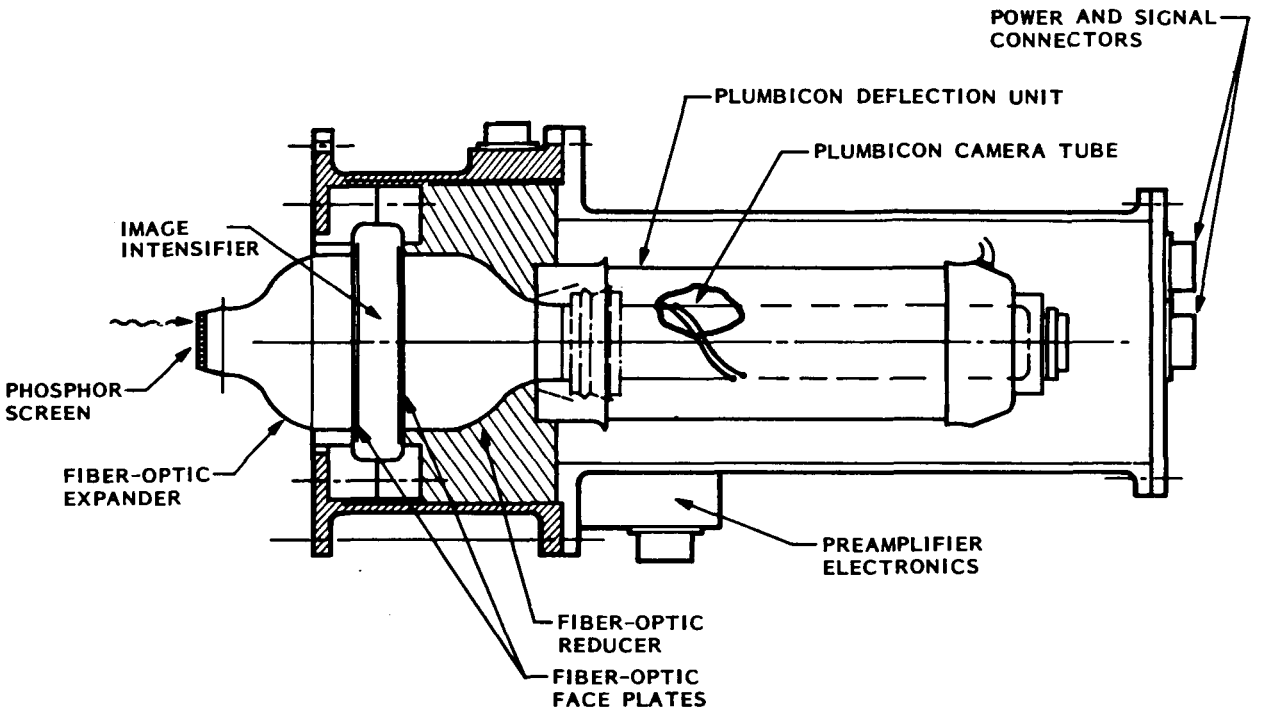

Figure C-3: Schematic of the **LEIS** detector system.

The detector system consists of five major elements: an input fiber optic lens, a proximity-focussed image intensifier, an output fiber optic lens, the Plumbicon television tube, and the Plumbicon control electronics. The arrangement of these elements is illustrated in Figure C-3. Both lenses consist of tapered coherent fiber optic bundles and have aperture ratios of about f/1.0. The small end of the input bundle carries the phosphor screens that convert the UV or EUV photons into visible light photons, which are subsequently conducted by the fibers and coupled to the input of the image intensifier. Scattered and stray visible light within the spectrograph is excluded from the detector by use of appropriate filters. The taper of the input fiber optic bundle provides magnification of the visible image, needed to match the inherently larger pixel size of the image intensifier. The intensified image is coupled and demagnified onto the target of the Plumbicon tube by the second fiber optic bundle. The Plumbicon control electronics define the target scan pattern, and may be set to scan either the whole target, or some predetermined portion of it. In this second or "window" scan mode, it is possible to select one or more spectral lines, reading them out into the data system and ignoring the remainder of the focal plane. Use of the window mode greatly reduces the demands on the data handling system.

The instrument as a whole is controlled by a microprocessor which sequences the operation of the primary mirror, the entrance slit mechanism, the detector control electronics, and the data handling system.

OPERATIONS

As shown in Figures 4.3 and C-1, light entering the instrument strikes the primary mirror, which forms an inverted image of the Sun on the entrance slit. The slit serves as a field stop and defines a segment of a chord on the solar disk that will be sampled by the spectrograph sections. Light passing the slit illuminates the two gratings as previously discussed. The gratings, in turn, disperse the spectrum and form images of the two spectral ranges on the input end of the detector assembly. Since both spectrographs are stigmatic, there is a point by point mapping of spatial elements along the sampled chord of the solar disk onto corresponding positions along the length of each spectral line. Thus, for a given setting of the primary mirror orientation, the instrument simultaneously observes both the UV and the EUV spectra of 480 spatial elements on the solar disk, assuming the use of 1-arcsecond pixels and an 8-arcminute-long slit.

To create a spectroheliogram, one observes a sequence of these stigmatic spectrograms, moving the primary mirror between spectrograms so that the slit sweeps across the desired area of the disk. A spectroheliogram can have any desired width and could, in principle, stretch from limb to limb or even further. It can be centered about any position on the disk. A total of 480 spectrograms would be required to cover a field of 8×8 arcminutes, again assuming 1-arcsecond pixels. The time required to complete an 8×8 arcminute spectroheliogram depends on the pixel sampling rate of the detector and the number of spectral elements sampled in wavelength space. Assuming a sampling rate of 10^7 pixels per second by the Plumbicon electronics, we arrive at a basic sampling rate of 2×10^4 spectral elements per second. (One spectral element corresponds to an intensity measurement at one wavelength for each of the 480 UV or EUV spatial elements. In practice, 500 spatial elements would be scanned in the focal plane for each spectral element, providing a small margin for alignment uncertainties.) These rates would allow us to sample about 40 spectral elements distributed between the UV and EUV image planes while completing a full 8×8 arcminute spectroheliogram in 1 s. It should be pointed out that at these high framing rates, the dwell time on any individual pixel is only about 2 ms, so that only flares and the brightest features of active regions will be observed with high photometric precision, although the ability to observe line profiles and Doppler shifts is retained. Photometric sensitivity may be increased by scanning a narrower field, or by scanning it more slowly. Both options will be possible under direction of the control system's microprocessor.

The system may also be operated in a slitless mode by substituting a rectangular aperture for the entrance slit. In this mode, increased photometric sensitivity is realized at the expense of introducing a convolution of spatial and spectral information, as in the NRL "A" instrument on Skylab. The effective sensitivity gain and the amount of overlap depend on the width chosen for the entrance aperture and the readout strategy. The maximum sensitivity gain obtainable for the 8×8 arcminute field at one frame per second is a factor of 500 to 1000 (depending on the intrinsic line widths) and results in complete overlap of the spectra.

A variety of other operating modes may be conceived by combining the basic ones discussed above. For example, a "super raster" could be generated by combining two adjacent 8×16 arcminute spectroheliograms, requiring 4 s to complete at the maximum scan rate. The entire disk could be searched to establish the locations of the active regions in about 20 s, again at the maximum

scanning rate. Definition of the required operating modes will be one topic of the phase A study. Other study topics include the choice of pixel size, the optimization of the spectrograph designs for wavelength coverage and resolution, and the definition of performance requirements for the primary mirror and slit mechanisms, and for the detector. The Phase A study will include a careful consideration of the choice between a Plumbicon and a charge-coupled device (CCD) as the readout device for the detector.

TRIAL DESIGN

A first iteration of **LEIS** optical system design has been made using software developed by R. J. Thomas for the **SEUTS** system. In this design, we have adopted a nominal focal length of 1.05 m for the spectrometer, and a 3600 groove per mm ruling frequency for the EUV grating. We took the slit-to-grating distance to be 1.0 m, which places the nominal camera distance at 1.1 m and gives the desired separation of the UV and EUV images. We specified the design wavelength range of the EUV portion to be 240 to 285 Å.

These choices of inputs to the optimization code lead to a complete specification of the properties of the EUV spectrometer, including the tangential and sagittal radii of curvature for the grating, the optimum angle of incidence, the angular and linear dispersions, and the location of the focal surface with respect to the entrance slit and the optic axis (as defined by the chief ray passing through the center of the slit). The values of the parameters are:

Spectral range:	240 to 285 Å
Spectral resolution element:	0.045 Å
Sagittal radius of curvature:	100.000 cm
Tangential radius of curvature:	105.497 cm
Angle of incidence:	5.423°
Width of spectrum (230 – 270 Å)	18 mm
RMS focal error (longitudinal astigmatism):	22.4 μm

Once the EUV design has been specified, the properties of the UV section are tightly constrained. If the nominal focal length is chosen to be the same as the EUV grating (which is desirable for reasons of simplicity), then the UV grating radii, the operating angles, and the geometric focal properties are all identical to those of the EUV section. The numerical resolution of the two sections is also the same if the same detector pixel size is used. The only free parameter is the ruling frequency for the UV grating, which is selected to choose the center wavelength of the UV section. For the trial design, we chose a center wavelength of 1312 Å. This choice led to a spectral range of 1200 to 1425 Å. The spectral resolution element for a 1000×1000 detector would be 0.21 Å. All other properties of the UV section are the same as those for the EUV section. The required ruling frequency would be 720 grooves per millimeter, which should be producible if a holographically recorded grating is used. These parameters should be fine-tuned during the Phase A study.

APPENDIX D: THE SOFT X-RAY IMPULSIVE PHASE SPECTROMETER

The Soft X-Ray Impulsive Phase Spectrometer (**SIPS**) includes both flat scanning and bent (fixed) Bragg crystal spectrometers. It will support the science objectives of **SHAPE** by providing information on the behavior (dynamics, energy content, parameters T_e, n_e, element abundances) of the hot plasma that is created during the impulsive phases of solar flares. Absolute coronal abundances of many elements can also be determined with this instrument. Comparison to measurements obtained with **HIGRANS** will make it possible for the first time to determine abundances at different levels in the solar atmosphere during a flare. In the following sections the scientific aims of the investigation and the properties of the spectrometers are described in greater detail than was possible in the main body of the text.

SCIENTIFIC AIMS

The primary science objective of the **SIPS** is to study plasma heating and dynamics during the impulsive phase of solar flares. To carry out this objective, high spectral resolution, high time resolution, and high sensitivity are required. A discussion of science objectives is given below.

a) Plasma Dynamics.

The Bragg spectrometers on **P78-1**, **SMM** and **Hinotori** have shown that early in the impulsive phase of flares spectral lines are much wider than expected at the temperatures obtained from dielectronic satellite lines. The "turbulent" or non-thermal motions are typically about 160 km s^{-1} when first observed, but can be up to 300 km s^{-1}. The motions, when integrated over relatively long time intervals, seem to be random since they appear to be the same for both disk and limb flares. The non-thermal motions decrease monotonically as the X-ray flux in spectral lines increases. By the time peak X-ray flux is reached, and during the decay phases of flares, the non-thermal motions have decreased to between zero and 60 km s^{-1}; it is difficult to measure values < 60 km s^{-1}. According to Antonucci *et al.* (Solar Phys., 78, 107, 1982), there is a correlation between the peak non-thermal motion and the peak flux in the hard X-ray bursts associated with the impulsive phase, but this result needs higher sensitivity observations for confirmation.

Recently, **SMM** observations reported by Doyle and Bentley (Astron. Astrophys., 155, 278, 1986) have cast doubt on the simple picture of completely random motions occurring over a smooth velocity distribution. Doyle and Bentley studied **SMM-BCS** Ca XIX high time resolution (6s) spectra and found many discrete mass flows, varying on time scales of seconds. Their data indicate that what appears as "broadening" at low time resolution (e.g., about 30s) may in fact be a smearing in time and velocity space of the directed motions of plasma perhaps produced by a number of different plasma sources. Interpretation of the data is difficult because of poor statistics, but they note that the determination of just how much structure is present in the line profiles must await a spectrometer with higher sensitivity.

The origin of the non-thermal motions is presently unclear. At present there seem to be two possible explanations. In one scenario, the large line widths are simply convective motions produced as plasma evaporates into coronal flux tubes. Frequently, however (in about 50% of the cases), large line widths appear well before the evaporative phase that is signified by the appearance of blue wings on the line profiles. Therefore, as an alternative scenario, Antonucci, Rosner, and Tsinganos (Astrophys. J., 301, 975, 1986) argue that turbulent motions can appear when magnetic islands produced by lack of MHD topological stability overlap and magnetic reconnection takes

place. These reconnection sites, which would occur throughout the flare volume, signify the flare onset and may also be responsible for particle acceleration. Thus the search for the origin of large turbulent line widths may lead directly to the processes responsible for particle acceleration.

In order to clarify further the nature of the line broadening, it is necessary to obtain observations with a more sensitive crystal spectrometer, while still preserving spectral resolution. The **SIPS** spectrometers have more than 10 times greater sensitivity than the instruments flown on the **SMM, P78-1,** and **Hinotori** missions.

Another major finding based on the results from previous spectrometers is that a blue-shifted component is frequently observed in X-ray lines during the impulsive phase (Doschek *et al.* Astrophys. J., 239, 725, 1980). This blue-shifted component may be the signature of chromospheric evaporation. In this process, energy deposited either by electron beams or by conduction fronts, heats the chromosphere, which responds by ablating hot plasma up into coronal flux tubes thereby producing the soft X-ray flare. The blue wings indicate velocities of about 400 km s^{-1}. In addition, Antonucci *et al.* (Solar Phys., 96, 129, 1986) report that in the earliest observable phase spectra that the entire X-ray line profile is shifted to the blue by about 80 km s^{-1}. This possibly indicates an initial upward motion of the flux tubes that confine all the soft X-ray plasma.

However, there are some problems in the chromospheric evaporation interpretation. These issues are debated in the Doschek *et al.* (1986) **SMM** Workshop chapter on Chromospheric Explosions. One of the problems is that the blue-shifted component is usually much weaker in intensity than the non-Doppler shifted stationary component. In only a few cases (e.g., Tanaka and Zirin (Astrophys. J., 299, 1036, 1985), Karpen *et al.* (Astrophys J., in press, 1986) is the blue-shifted component as strong as the stationary component. However, from numerical simulations (e.g., Doschek *et al.* Astrophys. J., 265, 1103, 1983), it is expected that at least in the very early rise phase the blue-shifted component should dominate. Perhaps the difficulty lies in not having instruments sensitive enough to observe the earliest phase of evaporation, or perhaps the situation is more complicated and an already existing high density loop is present that is rapidly heated to temperatures on the order of 20×10^6 K. Since such loops were not previously observed in Skylab at temperatures in the order of 10^6 K, these loops would presumably be relatively cool before flare onset, perhaps $< 5 \times 10^5$ K, i.e. transition region loops.

In order to obtain further insight into the origin of the blue-shifted component, it is again necessary to observe with a higher sensitivity spectrometer than the **SMM-BCS, P78-1,** and **Hinotori** instruments. A spectrometer with high sensitivity, spectral resolution and with < 5 s time resolution should clarify the origin of blue-shifted emission. Furthermore, high time resolution may reveal structure in the blue wing as has been found for the line broadening, and should make possible much more definitive comparisons of data with chromospheric evaporation models. These comparisons would greatly increase our understanding of energy and mass transport in flares.

b) Plasma Heating During the Impulsive Phase.

One of the deficiencies of the previously flown high spectral resolution spectrometers is that the very early impulsive phase heating of flare plasma could not be observed. Data from these spectrometers show a hot plasma, about 15×10^6 K, but neither the sensitivity nor the time resolution is high enough to study the prior heating up to this temperature. However, data obtained from the low resolution (SOX 1) **Hinotori** spectrometer (Tanaka *et al.* Moriyama *et al.* Annals of the Tokyo Astronomical Observatory, Volume XVIII, No. 4, Volume XIX, No. 2, 1983) show that with greater sensitivity, this heating could be studied. The earliest SOX 1 spectra obtained

at high time resolution during the impulsive phase of some flares are representative of plasma at temperatures of about 12×10^6 K. However, it is difficult to assign a precise temperature because the spectral resolution is insufficient to resolve the key temperature diagnostic line ratios. Furthermore, the statistics are not very good, and it is possible that transient features (e.g., enhancements of lines q and β) could be present in the spectra that cannot be detected because of the low spectral resolution. The prospect of having high spectral resolution observations of the initial heating phase (with a high time resolution **BCS**) is exciting and it is clear that such observations would shed considerable light on the murky subject of pre-flare heating.

Such an instrument could ascertain whether or not transient ionization is present in the plasma. At densities of about 10^{12} cm^{-3} and higher, the detection would probably not be possible if the plasma is rapidly heated to temperatures above 20×10^6 K, i.e., better than 1s time resolution is needed which pushes the instrument capability. However, for the densities of $< 10^{11}$ cm^{-3} transient ionization features could be detected, and, their detection would in fact provide a measure of the density, a parameter that cannot be obtained from line ratios for high temperature plasma near 20×10^6 K. For example, if a plasma with an emission measure of 3×10^{48} cm^{-3} is instantaneously heated to 20×10^6 K at a density of 10^{11} cm^{-3}, then about 270 counts s^{-1} could be detected by the Ge spectrometer of the **HSFCS** in the Fe XXIII line β approximately 1.5 s following the temperature increase to 20×10^6 K. These counts would be obtained in an **HSFCS** observing mode where the Fe XXIII line group between 1.865 and 1.880 Å is scanned in 1 s. For this same example, the **HSBCS** would accumulate about 300 counts in 1 s between the wavelengths 1.840 and 1.894 Å. These count rates would be sufficient to detect transient ionization at a density of 10^{11} cm^{-3} for a modest emission measure. Knowledge of the early impulsive phase flare density is a crucial test of the chromospheric evaporation hypothesis.

c) Plasma Diagnostics.

As was possible with the previously flown spectrometer experiments, the **SIPS** can provide electron temperature and emission measure estimates from spectral lines formed over a wide range of temperatures. For most flares, the temperature deduced from the Fe XXV line is close to the maximum temperature of the bulk of the soft X-ray emitting plasma although for flares with superhot components this may not be the case. It should be possible to determine the differential emission measure (DEM) distribution by combining the **SIPS** and **LEIS** data. This information gives considerable insight into the dynamics of the thermal plasma confined to magnetic loops. The DEM is not well known for the impulsive phase of flares.

Because **SIPS** has high spectral and time resolution as well as high sensitivity, analysis of the n=3 lines such as d13 may reveal the presence of non-Maxwellian velocity distributions. This is an aspect of the present spectra that has not yet been sufficiently investigated, but most likely present spectra do not have the combination of time resolution and sensitivity to exploit this diagnostic.

The **SIPS** will also provide the same information during the decay of flares. For example, **SIPS** and **LEIS** will measure the increase in height of post-flare loop X-ray emission as flares decay. The **SIPS** measurement makes use of the fact that fiducial Bragg angles change with position of the X-ray source (Seely and Feldman, Astrophys. J. Letters, 280, L59, 1984).

d) Superhot Component.

We plan to observe the Fe XXVI Lyman-α lines and associated satellite lines, and the Fe XXV resonance and satellite lines, with high spectral resolution. As Tanaka (Publ. Astr. Soc. Japan, in

press, 1986) has shown, the Fe XXVI and associated satellite lines are excellent indicators for the presence of a superhot component.

e) Element Abundances.

Given the wide range of temperatures and ions covered by both components of the **SIPS**, the absolute abundances of all the principal medium-Z (Mg to Ni) elements can be determined. A section of the X-ray spectrum that will be scanned by **SIPS** is shown in Figure D–1. In particular, the variation in element abundance seen in a number of flares by Sylwester *et al.* (Nature, 310, 665, 1984) can be examined for many more elements than was possible with the **SMM-BCS**. According to these workers, the calcium abundance varies by a factor of 2 to 3 in different flares. If this result is confirmed and extended to other elements, it would provide a further convincing demonstration of the existence of element fractionation or diffusion in the Sun, as recently discussed in detail by Meyer (Astrophys. J. Suppl., 57, 173, 1985). If element abundances can be significantly altered by electrodynamical or diffusive processes, this result will clearly have an important impact on other areas of astrophysics where abundance determinations play a critical role in unraveling the relevant physics.

Why are element abundances determined in the X-ray region superior to those obtained in the XUV or UV? In the X-ray region most of the ions are in H-like or He-like ionization stages, and excitation of these ions is well understood. The He-like ion stages contain about 80% of the element population, making abundance determinations not as sensitive to uncertainties in ion fraction calculations, as is the case in the UV and XUV. It is easier to calibrate an X-ray spectrometer than an XUV instrument, i.e. relevant X-ray lines used for line ratios fall within very narrow wavelength intervals. Plasma diagnostics are more precise in the X-ray region, i.e. we have dielectronic temperatures and the presence of a strong measurable continuum allows absolute abundances to be determined.

Veck and Parkinson (M. Not. R. Astr. Soc., 197, 41, 1981) determined element abundances using X-ray spectra from **OSO–8**. However, the **OSO–8** spectrometers had poor spectral resolution and sensitivity, which lead to large uncertainties in the abundances. An indication of the type of abundance determinations that can be made with a high resolution spectrometer (**P78-1**) can be found in Doschek *et al.* (Mon. Not. R. Astr. Soc., 217, 317, 1985).

INSTRUMENTATION

Two different types of crystal spectrometers are employed in **SIPS**. Based closely on the systems used in the **SMM–XRP** and **P78-1** SOLFLEX instruments, they are illustrated schematically in Figure D–2. The High Sensitivity Bent Crystal Spectrometer (**HSBCS**) provides the capability of very high sensitivity and time resolution observations of the important diagnostic iron-line group between 1.7 and 1.9 Å and the Ca-line group near 3.2 Å. The High Sensitivity Flat Crystal Spectrometer (**HSFCS**) provides the broad wavelength coverage needed for abundance and differential emission measure determinations. It also can perform high time resolution observations over narrow wavelength regions. Figure D–3 shows the two instruments upon which the designs of the **HSBCS** (a) and **HSFCS** (b) are based.

a) HSBCS

The design of the **HSBCS** will be based on the successful **SMM-BCS** instrument. Sensitivity will be greatly increased by removing the 6 arcmin FWHM square collimator. This will enable the

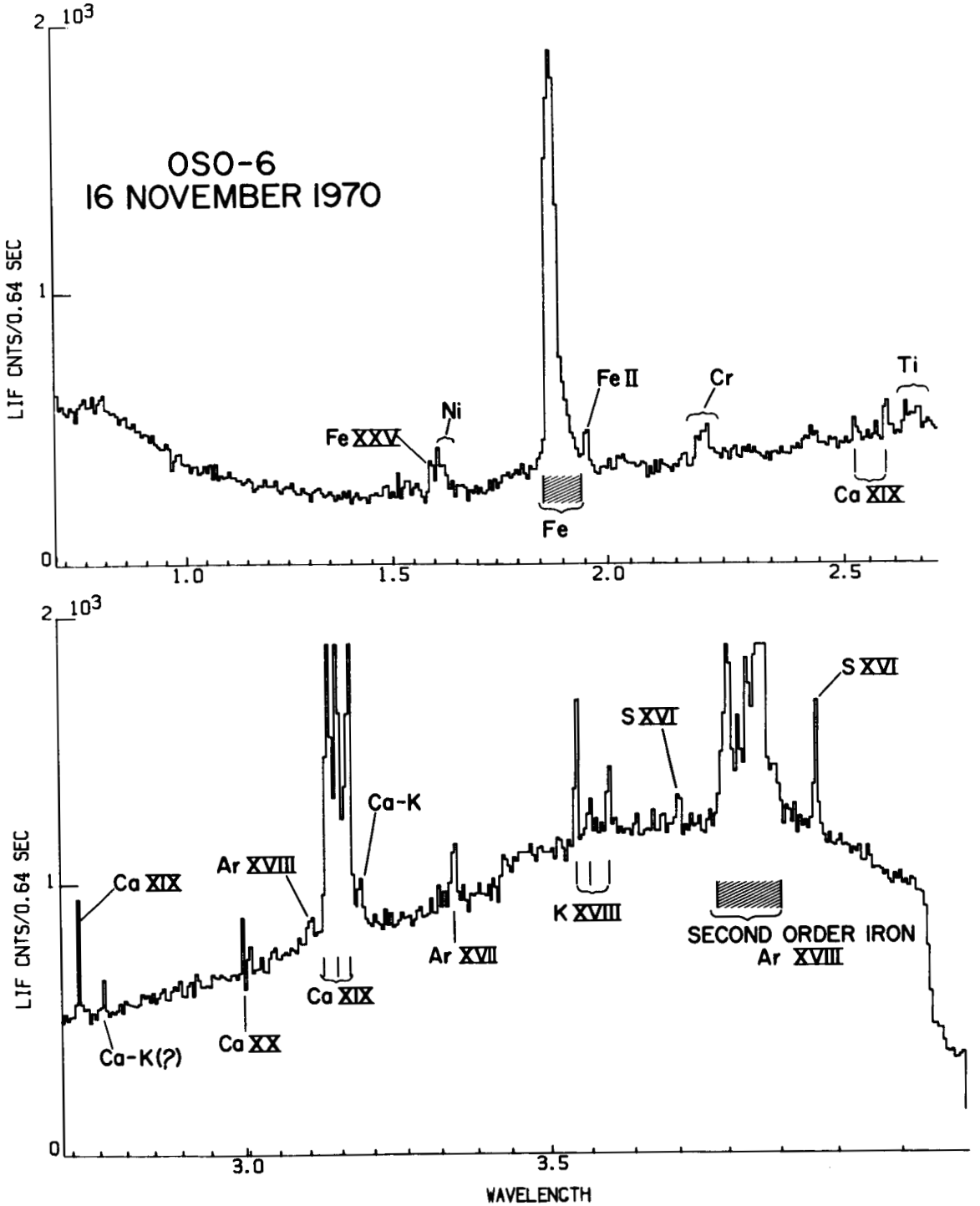

FIGURE D–1: The solar spectrum between approximately 1 and 4 Å as observed with the LiF spectrometer on **OSO–6**. This spectrum illustrates some of the lines of the various elements which **HSFCS** will observe with higher spectral resolution.

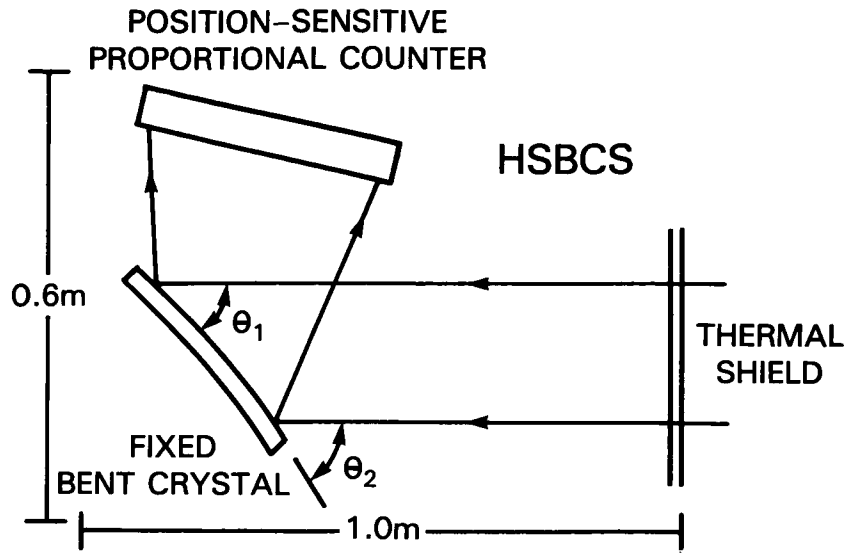

(4) Ge 220 λ=3.17–3.23 A
(4) Ge 422 λ=1.84–1.89 A

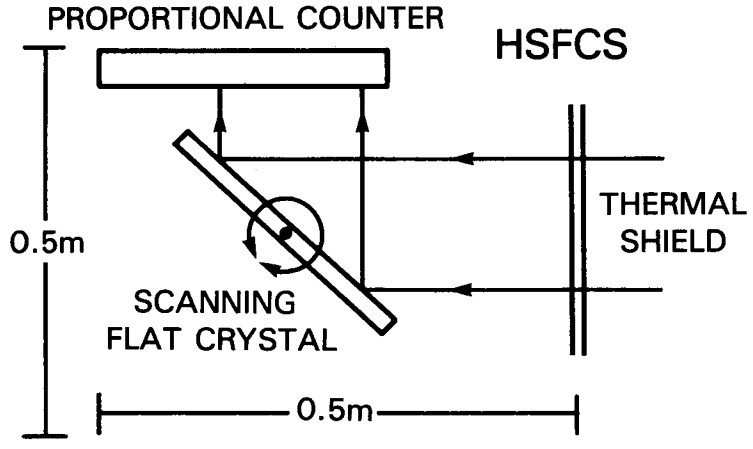

(1) Ge 220 λ=1–4 A
(1) ADP λ=1–10 A

FIGURE D–2: A schematic representation of the **SIPS** spectrometers. The top figure illustrates the concept of a bent crystal spectrometer. The entire wavelength range is obtained simultaneously. The bottom figure shows the concept of a conventional flat crystal spectrometer which obtains spectra by rotating its crystal through a selected range of Bragg angles.

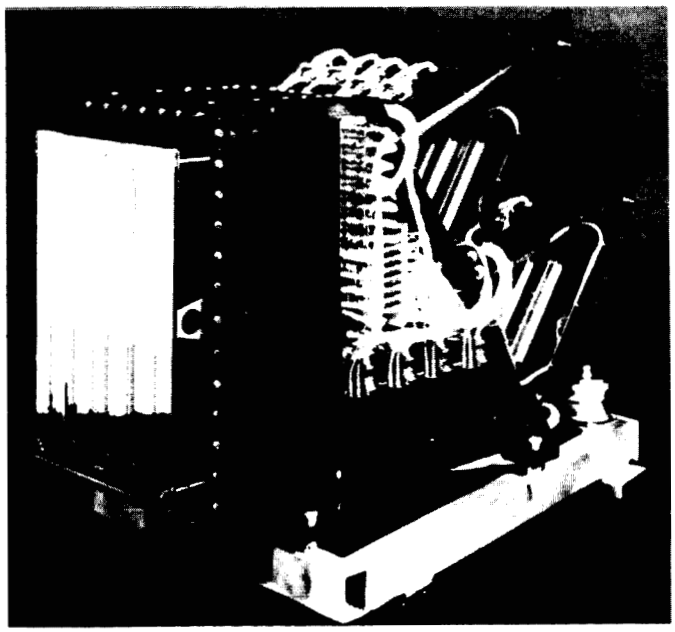

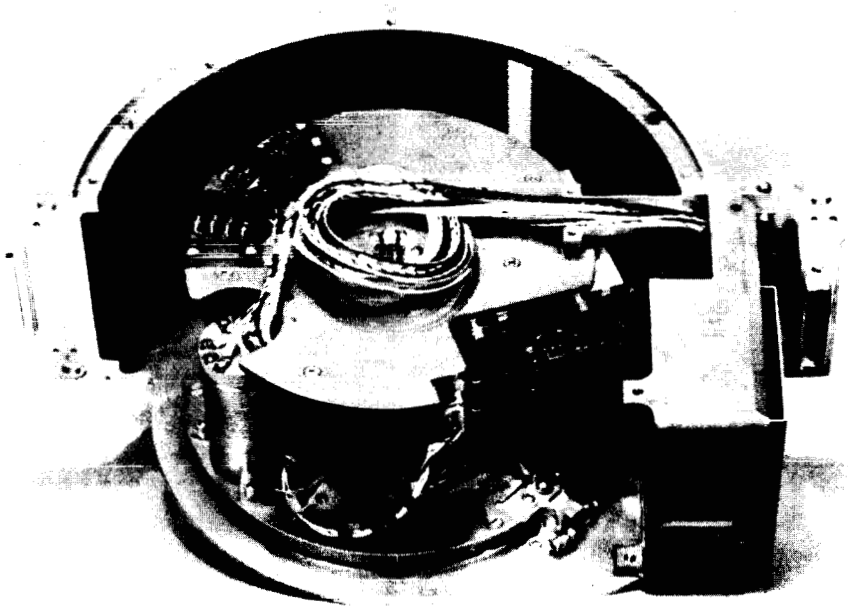

FIGURE D–3: (a) **SMM** bent crystal spectrometer (**BCS**). The **BCS** is approximately 0.8m long, 0.6m high and weighs 35kg. The spectrometer is capable of obtaining simultaneous wavelength coverage in eight energy bands covering the Ca XVIII–XIX lines near 3.2 Å and Fe I–XXVI lines near 1.9 Å. (b) The **OSO–6** flat scanning crystal spectrometer. An example of a spectrum obtained with this spectrometer is given in Figure D–1.

instrument to view the whole Sun and so to support the two high-energy instruments in studying all the flares detected by the **SHAPE** mission. In addition (see Table 5.4 in the main text) the **HSBCS** will study a smaller number of wavelength ranges than did the **SMM** instrument. These two measures will lead to an overall increase in sensitivity of around a factor 10 for the Ca XIX, Fe XXV and Fe XXVI spectral ranges.

The front aperture of the **HSBCS** will be covered by a second surface mirror and a thermal shield as was done successfully for the **SMM** instrument. Both spectrometers (**HSBCS** and **HSFCS**) will be mounted on an intermediate baseplate to ensure co-alignment before integration with the spacecraft. The **HSBCS** thermal and mechanical vibration properties will be very similar to those of the **SMM-BCS** and are therefore well understood.

The same germanium crystal cuts as were used in **SMM** would be employed in the baseline instrument. These crystals can be bent easily and provide high spectral resolution together with good reflectivity. Other crystals (e.g., InSb), which offer the promise of an even better combination of resolution and reflectivity, are being studied by Dr. R. Deslattes and his colleagues at **NBS** and will be carefully considered during Phase A. The crystals will be calibrated in their holders before launch to measure rocking curve width, reflectivity and radius of curvature, as was done for the **SMM** instrument. In addition, since one of the two **HSFCS** spectrometers will employ a germanium (or InSb) crystal, in-flight cross calibration of the **HSBCS** dispersion will be possible.

The **HSBCS** detectors will be sealed one-dimensional position sensitive proportional counters with 75 μm Be windows and filled with a Xe/CO_2 mixture at a pressure of 1.1 atm. The position resolution will be about four times better than was available in the **SMM** instrument through the use of a low noise wedge and strip readout system instead of the resistive anode used in **SMM**.

This modified wedge and strip or double wedge read-outs is illustrated in Figure D–4. The position (X) of the incoming photon is determined from the charges collected on the individual wedges (Q1,Q2), by $X = Q1/(Q1+Q2)$. A position resolution of 150 microns will improve **HSBCS** over the **SMM-BCS** by a factor of three in spectral resolution when the germanium crystal rocking curve width is taken into account. The double wedge read-out provides low thermal noise, low distortion and high linearity. In addition it can be easily manufactured as it consists of a pattern etched into gold on a fused silica substrate in a manner similar to electronic circuit boards. Detectors using wedge and strip read-out have been constructed at **MSSL** and the **HSBCS** detectors will be completely manufactured in-house.

The analogue electronics will be potted and attached to the rear of the detectors and will consist of standard charge sensitive preamplifier and analogue-to-digital circuitry. Although the determination of the photon energy by the detector is unnecessary for a Bragg crystal arrangement, the energy of the incoming photons will be measured by a thirty bin pulse height analyzer which will enable real-time monitoring of detector performance during times of moderate solar flux or when the calibration sources are moved into position in front of the detector windows.

Background rejection in the **HSBCS** will be accomplished by holding the double wedge in coincidence with cathode wires running the length of the detector and located between the double wedge read-out and the detector window. Additional background rejection will be provided by pulse height and shape discrimination.

During flares, hard X-ray photons which strike the crystals cause fluorescence radiation which is detected in the detectors as an additional background. The major contributor for germanium

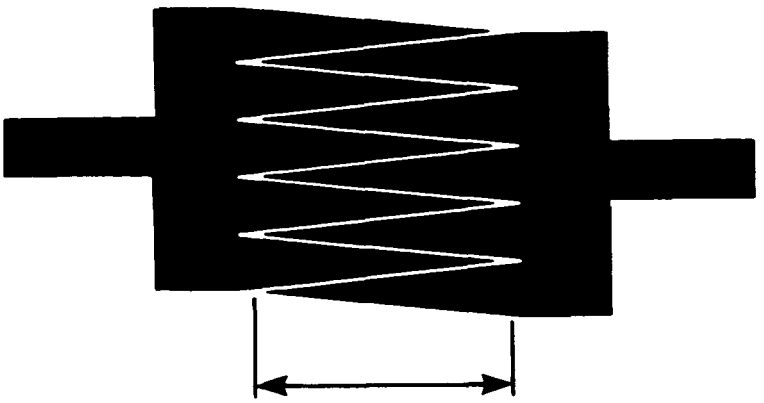

FIGURE D–4: An illustration of the modified wedge and strip or double wedge read-out anode. The position sensitivity is in the direction of the arrows. This anode will be used in the position-sensitive HSBCS detectors.

crystals is K-α emission at 1.25 Å. With even modest energy resolution it is possible to completely discriminate against the fluorescence emission without any loss of the Ca XIX signal. For the iron spectrometers an energy resolution of 13% FWHM at a rejection threshold of 1.54 Å will result in a rejection factor of 3000 for Ge K-α with negligible loss of Fe XXV, XXVI events. In addition, another factor of about two improvement over the **SMM-BCS** design will be achieved by including baffles (exit collimators) between detectors and crystals.

b) HSFCS

The **HSFCS** crystal spectrometers will have an overall sensitivity that is about 10 times greater than the **P78-1** SOLFLEX spectrometers. However, the actual gain in observational capability is substantially greater, because for a flat crystal spectrometer the rate of scan is a crucial factor in determining how well very transient spectra can be recorded. The SOLFLEX instruments recorded a spectrum every 56 s on average. With the HSFCS the time resolution for a measurement of an individual line profile can in some observing modes be as short as 0.5 to 1 s. The sensitivity of the **HSFCS** spectrometer will be sufficiently high to determine abundances of even the non-abundant solar elements, such as Mn and K. The non-abundant elements Mn, Cr, Ti, and K were already observed by **NRL** spectrometers flown on **OSO–6** (see Figure D–1). However, these spectrometers had poor spectral and time resolution, and were not well calibrated. In addition, counting statistics for these elements were poor. The sensitivity of the HSFCS is about 100 times greater than the LiF spectrometer on **OSO–6**, and therefore these and similar elements can be well observed by the **HSFCS**.

The thermal and mechanical design of the **HSFCS** will be similar to that of the highly successful **NRL** spectrometer flown on **P78-1** and successful spectrometers flown on **OSO–4** and **OSO–6**. The crystal drives can be programmed to scan over any desired wavelength interval, within the 1–10 Å range, at pre-selectable rates of 8, 16 or 32 steps per second with each step being about 20 arcsec. The complete 1–10 Å range can be scanned in about 5 minutes.

The **HSFCS** crystals will be germanium and ADP for the baseline instrument although, once again, the use of InSb and other crystals will be considered during Phase A. The instrument will include two rotating shafts: one with a germanium (Ge) crystal and the other with an ADP crystal. However, each main crystal will have its counterpart mounted back-to-back on the same shaft. Thus the primary Ge crystal will have an ADP crystal mounted behind it and the primary ADP crystal will have a back-to-back mounted Ge crystal. This arrangement will ensure redundant coverage of the entire **HSFCS** wavelength range with each of the two rotating shafts. The shaft drive mechanisms will employ stepper motors and perhaps harmonic drives. The drive mechanisms will be similar to the designs used for **P78-1** and **OSO** instruments. A thermal shield will prevent heating of the crystals by direct sunlight, as for the **HSBCS**.

For the **HSFCS**, each primary crystal will feed a single sealed proportional counter detector of conventional construction. The detector for the Ge crystal will be filled with a 1.1 atm. Xe/CO_2 mixture and fitted with a 75 μm Be window. For the ADP crystal, the detector will have a 60 μm thick Be window and a 1.1 atm. Argon/CO_2 gas filling. The **HSFCS** detectors are required only to register the X-ray counting rates as a function of shaft rotation angle. This can be done with amplifier, window analyzer and simple pulse counting circuitry. In particular, no position sensitivity is required for these detectors. The expected background counting rates in these detectors will be assessed during Phase A. It will then be decided whether the additional complexity and expense of an active anti-coincidence system is justified.

c) Digital Electronics.

The digital electronics design will be based on that of the **SMM-BCS** instrument. The baseline proposal is to use the same microprocessor (an RCS 1802) and merely adapt the present software for the increased capabilities of the **HSBCS** and the addition of the **HSFCS**. However, it could prove cheaper and easier to use more modern micros such as those Lockheed has been utilizing on the Spacelab II and Solar Optical Telescope projects. This will be investigated during Phase A.

The digital electronics accumulates the spectra for each of the detector systems (both **HSFCS** and **HSBCS**) in Read Increment Write memories for some preset integration time, after which they are read out and the memories cleared. The microprocessor adds flexibility to the instrument, making it possible to increase the time resolution in any given channel by degrading the time resolution in other channels or degrading the spectral resolution in that or other channels. Alternatively, the data can be processed at a higher rate and put in a queued store for later transmission. This can double the time resolution in all channels for a limited period (depending on the size of the queued memory store and the playback time available). The microprocessor also makes it possible to change the software in-orbit if different observing modes are required. It will also be possible to do some real time processing of the data and issue flare alerts in order to change the observing mode of **SIPS** or of any other instrument. The Command and Data Handling subsytem (CDH) would again be designed in the same way as on the present **SMM** spacecraft. The microcomputer would receive control and programme loads through a Serial Magnitude Command from the spacecraft. Its primary function is to process the spectral data from the **HSBCS** and **HSFCS**. There will be a small amount of engineering data in a subcom word for monitoring the health and safety of the experiment. There will also be an independent PHA monitor scalar that can be accumulated and cleared without affecting the spectral data.

d) Power supplies.

The power supply system would be similar to that of the SMM-BCS but with the additional

requirements from the **HSFCS**. Also, to run the RCA 1802 microprocessor at a higher rate than before, it would be required to run at a higher power level (if we use a different micro the power consumption requirements may be less). The **SIPS** power requirements are listed below.

	HSBCS	**HSFCS**	**TOTAL**
Dormant	< 7 Watts	< 4 Watts	< 11 Watts
Average Running	16 Watts	12 Watts	28 Watts
Peak Running (< 1%)	25 Watts	20 Watts	45 Watts

e) Telemetry.

The telemetry requirements are as follows:

HSBCS Maximum (no RT processing)	30 Kb/s
HSFCS Maximum	10 Kb/s
Total	40 Kb/s

This figure of 40 Kb s^{-1} represents the maximum data rate when all systems are running. Some savings could be made if we reduce the frequency of the readout in quiet times or do some on-board processing such as adding channels together, although this would make the software development more expensive. Not all data needs to be sent directly to the ground but could instead be recorded on one of the tape recorders of the other instruments where it would represent a minimal overhead compared to the imager signals.